Modelling breast cancer metastatic bone niche: a novel in vitro 3D microfluidic platform

MSc Thesis Project

Integrated Masters in Bioengineering, Major Molecular Biotechnology

Ana Rita Oliveira Alves Pereira

Project Supervisor: Dr. Daniela Sousa
Project Co-supervisor: Dr. Meriem Lamghari

September 2016

Abstract

Skeleton is among the most common site for breast cancer metastases, leading to the development of metastatic bone disease correlated with a significantly low prognosis of the disease over time. The development of breast cancer-induced bone lesions is based on a cooperative interaction between metastatic and bone cells, named "metastatic vicious cycle". Due to the lack of available *in vitro* tools to explore this intricate vicious interplay, the underlying molecular/cellular mechanisms are still poorly understood.

Here, it is originally developed a novel *in vitro* tri-culture system based on microfluidic technology to tailor the human *in vivo* metastatic bone niche.

The final tri-culture system was achieved through transferring both cancer and bone co-culture systems to the respective compartment of an optimized microfluidic chamber. The cross-effect between cells were assessed either by morphological studies, resorption functional assays or gene expression.

To perform this work, it was selected and tested two breast cancer cell lines, MCF-7 and MDA-MB-231, representing distinct subtypes (luminal A and Claudin-low, respectively) associated with different patterns of metastization and bone aggressiveness. Both MCF-7 and MDA-MB-231 spheroids were obtained through a feasible 4 days liquid-overlay culture in agarose non-adhesive coated surfaces in presence of 2.5% rBM. The high-throughput morphometric analysis revealed that MCF-7 spheroids, at an initial density of 10 000 cells, resulted in the formation of spheroids with 432 ± 11.27 µm diameter (n=50 spheroids) and an aspect ratio of 1. Additionally, F-actin staining and apoptosis FACS analysis confirmed the presence of a necrotic core (about 30% of apoptotic cells) resembling the tumour *in vivo* status. MDA-MB-231 spheroids at an initial density of 5 000 cells, exhibit a larger structural variability, due to their spread morphology and reduced capacity to form aggregate structures. Although it is possible to distinguish a major population with 369 ± 38.97 µm diameter (n=50 spheroids) and an aspect ratio of 1.3 from where were picked out the spheroid samples to the further characterization studies.

To establish the bone co-culture, human Mesenchymal Stem Cells ($2x10^4$ cells) were differentiated in osteogenic medium supplemented with 10^{-7} M dexamethasone, 10^{-7} M Vitamin D3, 10^{-2} M ascorbic acid and $5x10^{-5}$ M β-glycerophosphate for 14 days on top of bone-like structures, such as dentine discs, to resemble the *in vivo* bone microenvironment. Primary human blood-derived CD14+ cells with osteoclastic potential were expanded in presence of 25 ng/mL M-CSF and RANKL for 7/9 days and seeded ($1.2x10^5$ cells) on top of differentiated osteoblasts. The co-culture system was characterized progressively for both individual cell types. After 14 days of osteoblastic differentiation, MSCs were positive for ALP and Alizarin-red assays and highly expressed collagen, osteocalcin and RANKL genes. Obtained osteoclasts were TRAP+, capable of reabsorbing calcified matrix and exhibit a differentiated marker gene profile with high expression of TRAP, Ctsk and RANK genes.

The microfluidic tri-culture system was maintained for 4 days. The preliminary results show that MCF-7 spheroids exhibit a tendency to lose their original 3D structure in presence of bone cells, probably influenced by the secretion of factors from bone compartment, which is corroborated with the increased expression of VEGF and RANKL. In the other hand, MCF-7 cells appear to induce an over-activation of osteoclast activity, evidenced by a remarkable increase in resorption pit volume, area and depth. The increased expression of both RANK and RANKL in OB/OC co-culture experiments preliminary signposts a successful recapitulation of metastasis vicious cycle reported in the literature.

Overall, the obtained preliminary results demonstrate that it was effectively established an *in vitro* pilot tool to study breast cancer-bone cells interactions that is one step closer to natural conditions. Despite several optimizations and complementary studies are still required, this platform have the potential to provide a novel research-tool for drug screening in the scope of breast cancer bone metastasis in a high-throughput and reliable way.

Acknowledgements

Firstly, I would like to express my deepest sense of gratitude to my supervisor Daniela Sousa for the continuous support, teaching, motivation, enthusiasm, and immense perseverance – more than anything you teach me to never give up.

I am also deeply grateful to Professor Meriem Lamghari for the opportunity to be part of her bright team, and for her valuable guidance upon the project progression.

Furthermore, I am truly thankful for all my colleagues who supported me greatly and were always willing to help me; to all nBTT members and particularly to NOG team for all the inputs to my experiments that helped me to do a better work and for the welcome environment that provided me. I would like to do a special acknowledgement to Luís for being able to constantly combine the cheerfulness and the expertise – you also were always my favourite. Likewise, to Estrela for the incredible knowledge and her permanent smile. And lastly, to my master student fellows, who invade the i3S labs with joy and youth, for sharing with me the worst moments as well as the brightest ones. I couldn't ask for a better group of people – I fell really lucky for have you, guys.

It has been a period of intense learning for me, not only in the scientific area but also on a personal level. I would like to share this moment with my closest friends – to my wp girls who teach me 15 years ago what really means a team; to my c girls who share my craziness and let me be who I am; and to my fac friends who share the wildest and deepest memories along these incredible 5 years.

Last but not the least, I would like to deeply thank my beloved parents. I thank you just because you were always there – from the beginning. You both have all the reasons to feel proud. This accomplishment would not have been possible without you.

Sincerely,
Rita

Index

List of Figures

List of Tables

Acronyms

2D	Two-dimensional
3D	Three-dimensional
ALP	Alkaline Phosphatase
AP1	Activator Protein 1
APC	Allophycocyanin
ATP	Adenosine Triphosphate
B2M	Beta-2-microglobulin
BMP	Bone Morphogenetic Protein
BSA	Bovine Serum Albumin
BSE	Backscattered electrons
Ca^{2+}	Calcium ions
CD14	Cluster of differentiation 14
cDNA	Complementary DNA
COL1A1	Type I collagen
C_T	Threshold cycle
CTR	Calcitonin Receptor
CtsK	Cathepsin K
DMEM	Dulbecco's Modified Eagle Medium
DNA	Deoxyribonucleic acid
dsDNA	Double stranded DNA
ECM	Extracellular Matrix
EDS	Energy Dispersive X-ray Spectroscopy
EHS	Engelbreth-Holm-Swarm
EMT	Epithelial to Mesenchymal Transition
ER	Estrogen Receptor
FACS	Fluorescence-activated cell sorting
FBS	Fetal Bovine Serum
GFP	Green Fluorescent Protein
HER2	Human Epidermal growth factor Receptor 2
HIST	Histone cluster H2A
HTP	High-throughput

IBSP	Bone Sialoprotein
IGF-1	Insulin Growth Factor 1
IL	Interleukin
MCF-7	Michigan Cancer Foundation-7 breast cancer cell line
M-CSF	Macrophage Colony-Stimulating Factor
MDA-MB-231	M.D. Anderson - Metastatic Breast-231 breast cancer cell line
MET	Mesenchymal to Epithelial Transition
mm	Millimetre
MMP	Matrix Metalloproteinases
MOB	Osteoblastic medium
MOC	Osteoclastic medium
mRNA	messenger RNA
MSC	Mesenchymal Stem Cell
NF-κB	Nuclear Factor kappa-light-chain-enhancer of activated B cells
NFATc1	Nuclear Factor Of Activated T-Cells 1
OB/OC	Osteoblast-Osteoclast
OCN	Osteocalcin
OPG	Osteoprotegerin
OSX	Osterix
PA	Polyacrylamide
PBMCs	Peripheral blood mononuclear cells
PBS	Phosphate-buffered saline
PDL	Poly-D-lysine
PDMS	Polydimethylsiloxane
PEG	Poly(Ethylene Glycol)
PFA	Paraformaldehyde
PGE2	Prostaglandin E2
pHEMA	Poly(2-hydroxyethyl methacrylate)
PI	Propidium Iodide
PLGA	Poly(Lactic-co-Glycolic Acid)
PO_4	Phosphate
PR	Progesterone Receptor
PTH	Parathyroid Hormone

PTHrP	Parathyroid Hormone-related Protein
RANK	Receptor Activator of Nuclear factor(NF)-κβ
RANKL	Receptor Activator of Nuclear factor(NF)-κβ Ligand
rBM	reconstituted Basal Membrane
RG	Reference Gene
RNA	Ribonucleic acid
RT-PCR	Reverse transcription polymerase chain reaction
Runx2	Runt-related transcription factor 2
SE	Secondary electrons
SEM	Scanning electron microscopy
TCPS	Tissue Culture polystyrene
TGF-β	Transforming Growth Factor-beta
TNF-α	Tumour Necrosis Factor-alfa
TRAP	Tartrate-Resistant Acid Phosphatase
VEGF	Vaso-endothelial Growth Factor
YWHAZ	Tyrosine 3-monooxygenase
α-MEM	Alpha Modified Eagle Medium
μm	Micrometre

Chapter I

General Introduction

---

1. Disease fundamentals: the dimension of the problem

1.1. The biology of cancer: the tumorigenesis process

1.2. Relevance of breast cancer cell lines as models for breast tumour

2. Bone microenvironment: tissue structure and functions

2.1. Bone Remodelling

2.1.1. Bone-forming cells: Osteoblasts

2.1.2. Bone-resorbing cells: Osteoclasts

2.2. Coupling of bone metastatic niche: the metastatic vicious cycle

3. Cancer models: paradigm shift on novel research tools

3.1. Microfluidic laws: miniaturized engineering flows in biology

3.1.1. Microfluidic 3D models of cancer: cells interaction over fluidics

Aims of work

Chapter I

General Introduction

1. Disease fundamentals: the dimension of the problem

Despite all efforts, cancer still remains the leading cause of morbidity and mortality worldwide. There were approximately 14 million new cases and 8.2 million cancer-related deaths (~14% of all human deaths) in 2012, and this number is expected to pass 13 million in 2030 [1].

Breast cancer is one of the most common human neoplasms, accounting for approximately 1/4 of all cancers among women aged 20-59 years worldwide [1]. Additional risk factors include early menarche and late childbirth, wherefore incidence rates are highest in industrialized countries, such as western and northern Europe, North America and Australia [2].

Of those women who progress to an advanced stage of disease, over 80% develop metastatic bone disease, which is associated with progressive skeletal complications – i.e. severe bone pain, skeletal fractures, hypercalcemia and nerve compression, all of which with a profoundly impair in patient's quality of life and poor prognosis [3]. Metastatic bone disease treatments are often palliative and does not improve overall survival – actually, the disease is associated with significantly low survival rates, around 2-years after diagnosis [4].

1.1. The biology of cancer: the tumorigenesis process

The behaviour of individual cells and, ultimately, the dynamic state of multicellular tissues is regulated by the balanced activity of hundreds of genes that intricately control the process of cell division [5]. Mutations on those genes caused by a failure on regulatory process lead to uncontrolled cell growth and therefore to a proliferation autonomy that characterizes the earliest hallmark of a tumorigenesis process [6].

According to the most widely accepted model of tumour progression, the somatic clonal evolution [7], the cancerigenous offspring is characterized as a heterogeneous cluster composed by several cancer specialized cell-subpopulations with a divergent accumulation of mutations. This heterogeneity is mostly determined by selective pressures of tumour microenvironment in a bidirectional way, i.e. as the tumour mass increases, the interior of the tumour grows farther away from existing blood supply creating a hypoxic and acidic environment leading to a higher genetic instability, which in turn increases the propensity to accumulate additional mutations [8]. Eventually, cells of primary tumour with an malignant phenotype undergo an epithelial to mesenchymal transition (EMT) that enhance their migratory and invasive capabilities [9], and consequently allow them to enter on blood circulatory system through the leaky new formed blood vessels or via the surroundings lymphatic vessels [10] (see Figure I.1).

Once in circulation, cancer cells disseminate themselves through circulation flow patterns [11] and, according to the "seed and soil" hypothesis proposed by Stephen Paget in 1880s [12], specific malignant clones are able to extravasate to tissues with favourable characteristics [11, 13]. Herein, metastatic cells might remain dormant when there is a lack of proliferation-stimulating adhesion signalling molecules [14], or can create a supporting tumour microenvironment in which stromal cells co-evolve with tumour cells influencing the metastatic tumour self-progression [15].

Breast cancer cells can disseminate from the tumour in very early stages. Cancerigenous cells that leave the breast tumour by blood vessels will be carried by the blood flow where they are transported to distant organs, preferentially, to the lung, liver, brain and particularly to the bone [16].

Women with metastatic breast cancer face distinct challenges compared to those with early-stage breast cancer. Metastatic breast cancer cells frequently differ from the preceding primary breast cancer in properties such as receptor status [17] – the cells have often developed resistance to several lines of previous treatment and have acquired special malignant features. The heterogeneous nature of breast cancer metastasis makes it difficult not only to assess the risk factors for metastasis, but also to define a treatment for the cure of this disease.

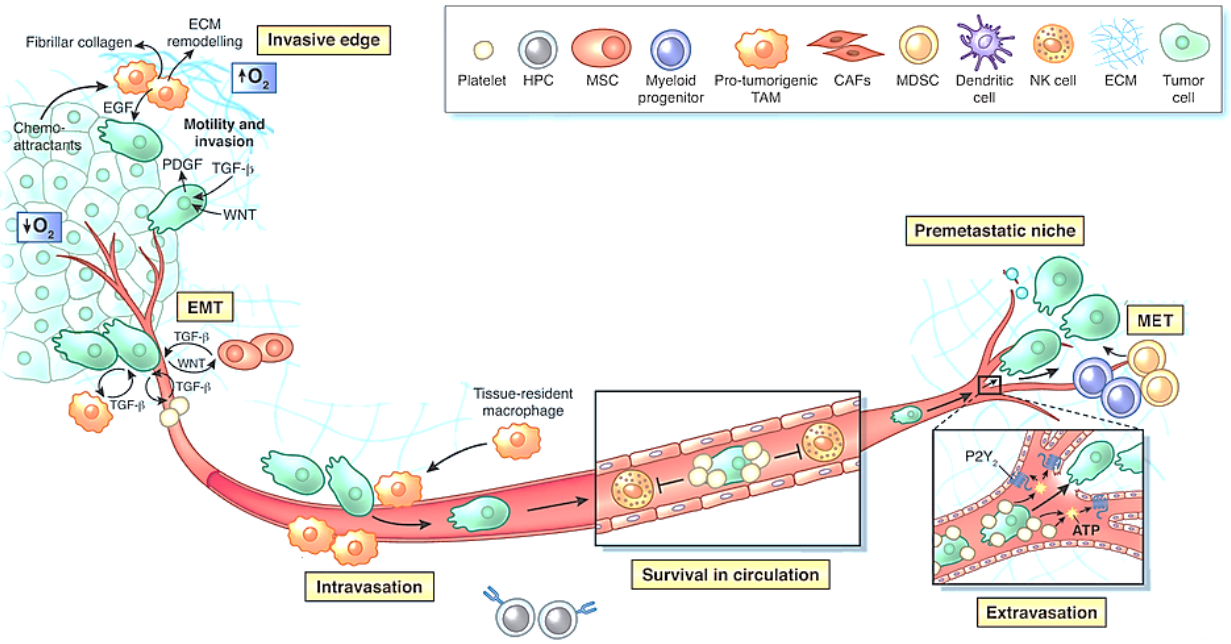

Figure I.1. Cellular transformations over cancer progression and invasion of metastatic cells to distant organs. The process of cancer metastasis consists of sequential, interlinked and selective steps with some stochastic elements. The outcome of each step is influenced by the interaction of metastatic cellular subpopulations with homeostatic factors and cells. Local invasion of the host stroma by some tumour cells occurs by several parallel mechanisms – macrophages, platelets and MSCs contribute to the epithelial-mesenchymal transition at primary sites, allowing tumour cells to detach from neighbourhood epithelial cell-cell contacts and acquire a mobile and invasive phenotype. In the circulation, platelets and components of the coagulation system support tumour cell survival by protecting them from cytotoxic immune cell recognition. Ultimately, the circulating tumour cells become trapped in the capillary beds of distant organs by adhering to capillary endothelial cells and extravasation from the blood vessels occurs trough molecular and enzymatic pathways. At secondary sites, the cells go through a mesenchymal-epithelial transition (MET) that allow them to adhere and proliferate within the organ parenchyma, forming micrometastasis with a permissive niche to tumour colonization that might either remain dormant for years or bump into a new big tumour mass (adapted from [18]).

1.2. Relevance of breast cancer cell lines as models for breast tumour

Breast cancer is a complex and heterogeneous disease. Analysis of adjuvant trials has shown that not all chemotherapeutics have equal effects on breast cancer patient and there are significant differences in chemotherapy sensitivity across disease subtypes [19]. Five subtypes of breast cancer are commonly accepted by the scientific and medical community, which if further validated could be used to guide the best decision-making in patient treatment (see Table I.1) [20].

In the laboratory, mechanistic studies of human breast cancer are largely reliant on *ex vivo* culture using established immortalized cell lines. Their heterogeneity is classified based on the histological type, tumour grade, lymph node status and the presence of predictive markers such as oestrogen receptor (ER), progesterone receptor (PR) and human epidermal growth factor receptor 2 (HER2), which will translate a different behaviour upon the chemotherapeutic approach [17].

Many of the currently available breast cancer cell lines were established in the 1970s and became widespread with MCF-7 cell line [21] and MD Anderson series [22] – both cell lines were obtained from invasive ductal carcinoma derived of metastatic site by pleural effusion and are now widely available through commercial cell banks.

In fact, MCF-7 and MDA-MB-231 cell lines account for the overwhelming majority of all abstracts reporting studies on human breast cancer [23]. The popularity of MCF-7 is largely due to its exquisite hormone sensitivity through expression of ER, making it an ideal model to study hormone response [24]. By other hand, MDA-MB-231 is a further advanced metastatic cell line from which the mesenchymal markers overrule the epithelial and is not affected by endocrine factors [22]. More recently, elegant experiments by Massague's group have developed highly metastatic derivatives of MDA-MB-231 cells that home to particular metastatic sites through rounds of *in vivo* selection in immune-deficient mice, exhibiting unique metastatic capacities compared to the parental MDA-MB-231 line, including bone-selective homing, distinct transcriptional profiles and more aggressive phenotype [25].

Table I.1. Molecular classification of some selected metastatic breast carcinoma cell lines (adapted from [20]).

Subtype	Immunoprofile	Other characteristics	Cell lines
Luminal A	ER^+, $PR^{+/-}$, $HER2^-$	$Ki67^{low}$, E-cad^{high}, endocrine responsive	MCF-7, T-47D
Luminal B	ER^+, $PR^{+/-}$, $HER2^+$	$Ki67^{high}$, E-cad^{low}, endocrine & trastusumab responsive	BT-474, ZR-75
Basal-like	ER^-, PR^-, $HER2^-$	$Ki67^{high}$, E-cad^{low}, endocrine nonresponsive	MDA-MB-468
Claudin-low	ER^-, PR^-, $HER2^-$	$Ki67^{low}$, E-cad^{low}, $Claudin^{low}$, endocrine nonresponsive	MDA-MB-231, BT-549
HER2 enriched	ER^-, PR^-, $HER2^+$	$Ki67^{high}$, E-cad^{low}, trastusumab responsive	SKBR3, MDA-MB-453

2. Bone microenvironment: tissue structure and functions

Bone is a highly specialized form of connective tissue capable of adapting is structure to mechanical or biochemical stimuli [26]. It is a complex metabolic active tissue in which the extracellular matrix is mineralized, conferring marked rigidity and strength to the skeleton while still maintaining some degree of elasticity. Type I collagen constitutes approximately 95% of the organic matrix and the remaining 5% is composed of proteoglycans and numerous noncollagenous proteins [27]. In addition to its supportive and protective functions, bone is a major source of inorganic ions, such as calcium, magnesium and phosphate, which form crystals of hydroxyapatite in the collagenous matrix of the bone, controlling their homeostasis in the body through cellular regulation signalling [27].

Morphologically, bone is composed by two components: cortical (compact) and trabecular (cancellous/spongy) bone. Compact bone has a sturdy calcified and mineralized matrix with very few spaces. This type of bone not only forms a dense protective shell around the spongy bone tissue (see Figure I.2), but it also provides skeleton rigidity, strength, and high resistance to bending and torsion [26]. On the other hand, trabecular bone is composed of a porous honeycomb-like network of trabecular plates and rods interspersed in the bone marrow compartment of mature bones [26].

Differences in the structural arrangements of the two bone types are related to their primary functions: cortical bone provides mechanical and protective functions, while cancellous bone provides metabolic functions [28].

The complex structure of bone tissue, the heterogeneity of cell types, as well as the cross-linked extracellular matrix and the mineral phase, all combine to make bone a complex living tissue of which the knowledge of the structural, molecular, and functional biology is essential for the better comprehension of this tissue as a multicellular unit and a dynamic structure in order to manage new therapeutic approaches to bone diseases.

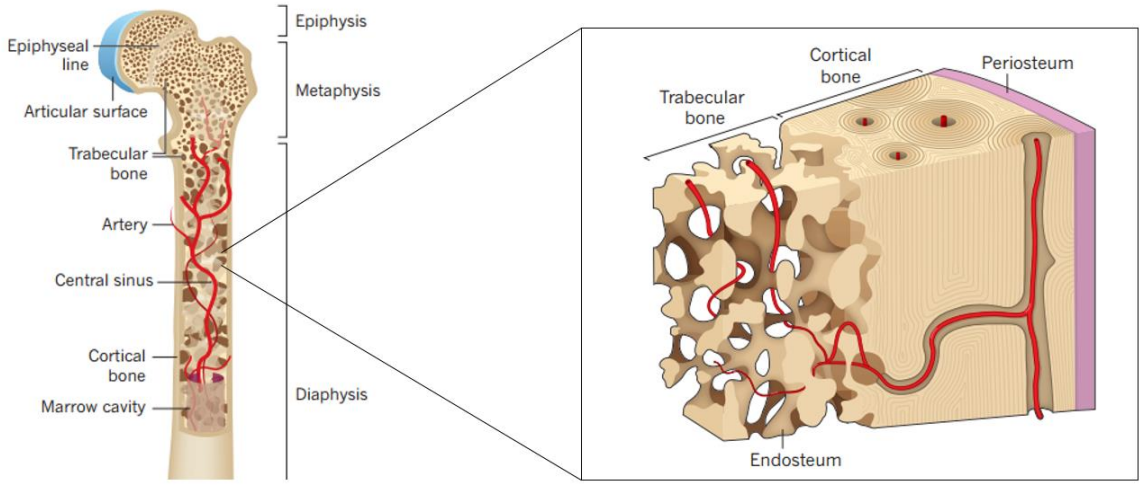

Figure I.2. Long bone anatomy. The hard outer layer of bones is composed by cortical bone, which gives bone its smooth, white and solid appearance, and accounts for 80% of the total bone mass of an adult human skeleton. Cortical bone consists of multiple microscopic columns (each called an osteon) of osteoblasts and osteocytes around a central canal called the Haversian canal. The columns are metabolically active and, as bone is reabsorbed and created, the nature and location of the cells within the osteon will change. Cortical bone is covered by a periosteum on its outer surface and an endosteum on its inner surface, establishing the boundary between the cortical bone and the cancellous bone. The interior of the bone is filled with cancellous bone also known as trabecular or spongy bone tissue – thin formations of osteoblasts forming an irregular porous network. Within these spaces lays bone marrow and hematopoietic stem cell niches that give rise to platelets, red blood cells and white blood cells (adapted from [29]).

2.1. Bone Remodelling

Bone tissue is in continuously remodelling to ensure correct mineral homeostasis and to maintain the structural integrity, and thereby bone strength [30]. This complex process, termed Bone Remodelling, requires the interaction between different cell phenotypes that are regulated by a variety of either local or systemic biochemical and mechanical factors [31].

The major cellular elements of bone include osteoclasts, osteoblasts, osteocytes and bone-lining cells, along with the precursors of these specialized cells. The pivotal bone cells, osteoblasts and osteoclasts, act as supportive cells and simultaneously as bone modulators producing their own matrix. Bone matrix is, therefore, a rich storehouse of growth factors [32] synthesized by osteoblasts and released in the surrounding environment through osteoclastic bone resorption [28]. Disturbances on the balance between these complementary processes might result in metabolic bone diseases, such as osteoblastic or osteolytic lesions [33].

2.1.1. Bone-forming cells: Osteoblasts

The osteoprogenitor cells arise from local MSCs within the bone marrow cavity. MSCs have the ability of self-renewal and equally the capacity of differentiate through highly regulated processes into osteoblasts, (see Figure I.3), adipocytes and chondrocytes [34].

Functionally, fully differentiated osteoblasts are cuboidal cells (15-20 µm thick) located at the bone surface [35], with a large nucleus, cellular processes, gap junctions, abundant endoplasmic reticulum, enlarged Golgi and collagen-containing secretory vesicles. Osteoblasts express receptors to many bone agents, such as parathyroid hormone-related protein (PTHrP), prostaglandins, vitamin D metabolites, gonadal/adrenal steroids and several cytokines, all responsible for maintaining cellular function and responsiveness to metabolic and mechanical stimuli [36].

Osteoblasts are the cells responsible for producing and secreting specific proteins for the extracellular matrix and therefore create newly formed bone tissue. A major product of the bone-forming osteoblast is type I collagen, but osteoblasts also synthesize a number of other proteins that are incorporated into the bone matrix, including osteocalcin and osteonectin which supports bone cells function and survival [35].

In addition, mature osteoblasts express relatively high amounts of alkaline phosphatase (ALP) onto the external surface of their plasma membrane. ALP is a phosphotransferase that allows the bone mineralization by hydrolysing inhibitors of mineral deposition such as pyrophosphates [35], thus regulating the matrix mineralization process. In point of fact, ALP knockout mice developed hypophosphatasia, a condition characterized by defective bone mineralization [37].

The average lifespan of a matrix forming human osteoblast is 3 months [38] – after a long process of bone formation and maturation, eventually some cells start an apoptosis process. The remaining cells are either converted to lining cells that cover quiescent bone surfaces or are buried within the mineralized matrix as osteocytes [35] (Figure I.3).

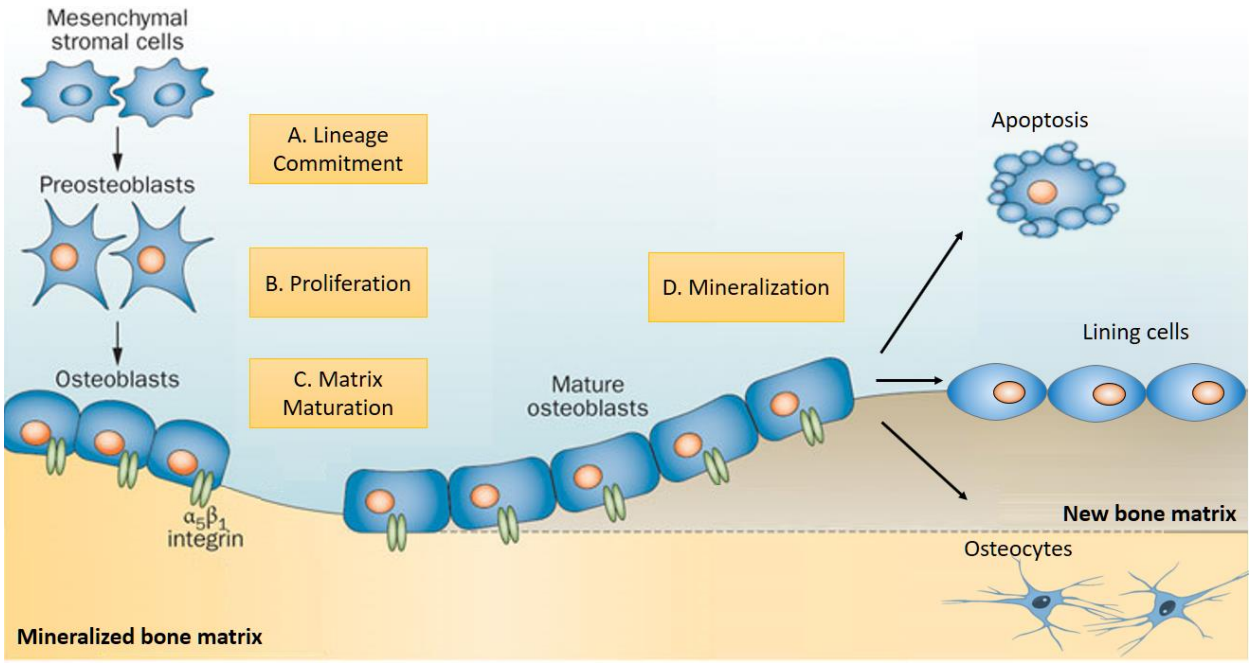

Figure I.3. Stepwise development of metabolic phases of osteoblastic differentiation and maturation. A: Lineage Commitment – the osteoprogenitor cells arise from local MSCs within the bone marrow cavity; MSC commitment to the osteoblastic lineage is initiated with the influence of Bone Morphogenetic Protein (BMP) and Transforming Growth Factor-beta (TGF-β) which induces a transduction cascade in precursors cells [39]. **B:** Proliferation – these progenitor cells have a high rate of proliferation and express Runt-related transcription factor 2 (Runx2), a transcription factor of great importance that suppresses MSC differentiation into chondrocytes and adipocytes. Runx2 regulatory element is present in the promoter of several osteoblastic genes controlling their expression, including type I collagen (COL1A1) and bone sialoprotein (IBSP) [40]. **C:** Matrix Maturation – The precursors cells differentiate further into osteoblasts under the influence of Parathyroid hormone (PTH) inducing the expression of increasing levels of ALP activity. In addition, PTH stimulates the receptor activator of nuclear factor(NF)-κβ ligand (RANKL) mRNA expression, which performs a central role in osteoclast maturation, as well as other matrix components and growth factors [41]. **D:** Mineralization: mature osteoblasts under the combined action of Insulin growth factor 1 (IGF-1) and Prostaglandin E2 (PGE2) express typical secretory characteristics, with a well-developed rough endoplasmic reticulum and a large Golgi apparatus necessary to the production of bone matrix components [42]. Another important transcription factor is Osterix (OSX), a zinc-finger transcription factor that acts downstream of Runx2 and modulates osteoblast differentiation, bone formation and mineralization[43]. In the final stages of osteoblast differentiation only a fraction of mature osteoblasts survives becoming either quiescent bone-lining cells or become sensorial and supportive cells entrapped in the calcified matrix with dendritic extensions, named osteocytes [44] (adapted from [45]).

2.1.2. Bone-resorbing cells: Osteoclasts

The osteoclasts are large (50 to 100 mm diameter) multinucleated cells with abundant mitochondria and numerous lysosomes formed by the fusion of macrophage colony-stimulating factor (M-CSF)-dependent haemopoietic precursors, including mononuclear cells present in the peripheral circulation [46]. After proliferating in bone marrow, mononuclear preosteoclasts are guided to bone surfaces [47] where several cytokines and growth factors are known to affect the differentiation pathway of the osteoclast and induce cell fusion. Studies have confirmed the central role of the RANK-RANKL-OPG pathway in this process [41], as depicted in Figure I.4 and more extensively discussed below.

Osteoclasts most remarkable morphological feature is the ruffled border, a complex system of finger-shaped projections of the membrane formed by tight junction between the bone surface and the basal membrane, creating a sealed compartment from each they mediate the resorption of the calcified bone matrix that results on excavations of authentic resorption pits (Howship's lacunae) demonstrated both *in vivo* and *in vitro* [48]. The mineral component of the matrix is dissolved in the acidic environment of the resorption site, which is created by the action of an ATP-driven proton pump located in the ruffled border membrane. The protein components of the matrix, mainly the collagen type I fibres, are degraded by matrix metalloproteinases (MMP) such as MMP-2 and MMP-9, and acidic hydrolases such as cathepsins K, B, and L which are secreted by the osteoclast into the sealing zone [49] (see Figure I.4b). The degraded bone matrix components are endocytosed along the ruffled border within the resorption lacunae and then transcytosed to the membrane area opposite the bone, where they are released [48]. Another feature of osteoclasts is the high expression of phosphohydrolase enzyme tartrate-resistant acid phosphatase (TRAP). TRAP knockout mice exhibit an impairment in the bone resorption process, however the primary molecular mechanisms are still poorly understood [50].

One resorption cycle of any individual osteoclast thus involves complex multistep processes, which include osteoclast attachment and polarization, formation of a sealing zone and resorption, followed by final detachment and cell death [49] whereby their apoptotic bodies are quickly removed by phagocytes (see Figure I.4a) [51].

In the past, the *in vitro* study of osteoclasts relied on giant cell tumours removed of surgical clinical procedures, and the subsequent isolation of osteoclasts from these tissues [26]. A significant breakthrough in the understanding of osteoclastogenesis process occurred when murine systems using co-cultures of bone marrow and stromal cells yielded osteoclasts [52]. It is now known that this system allowed for production of two haematopoietic factors that are both necessary and sufficient for osteoclastogenesis: the TNF-related cytokine RANKL [53] and the polypeptide growth factor M-CSF [54]. Together, M-CSF and RANKL activates the receptor activator of nuclear factor(NF)-κβ (RANK) on the surface of haematopoietic precursor cells which induces the expression of genes that commit to the osteoclast lineage, including those encoding for TRAP, cathepsin K (CtsK), calcitonin receptor (CTR) and the αvβ3-integrin, promoting further survival and activation of osteoclasts resorptive activity [55].

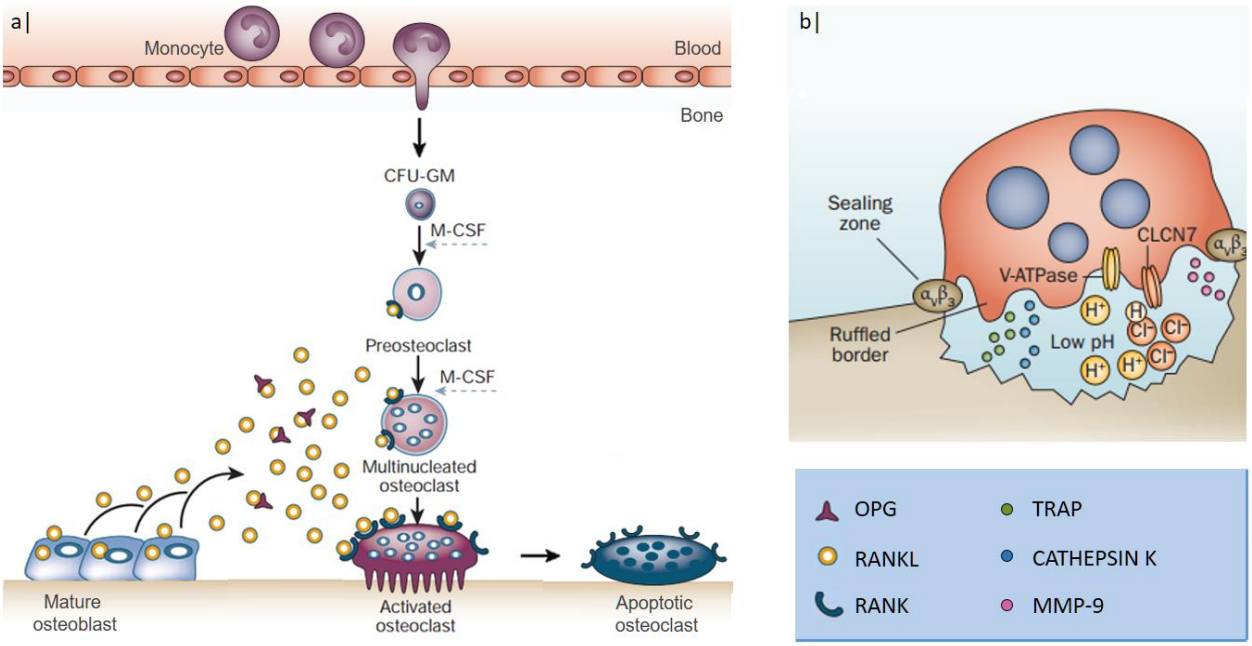

Figure I.4. Osteoclasteogenesis and osteoclast activation process: schematic representation of **a|** physiological regulation of osteoclast differentiation, activation and death, and **b|** the molecular machinery, lytic enzymes and cytoskeletal organization evolved in the bone resorption process by osteoclasts**.** The osteoclast is derived from the pluripotent hematopoietic stem cell, which gives rise to a myeloid stem cell that can further differentiate into megakaryocytes, granulocytes, monocytes/macrophages and osteoclasts. Osteoclast maturation occurs on bone from peripheral blood bone mononuclear cells, being the earliest identifiable hematopoietic precursor able to form osteoclasts the macrophage-colony forming unit [55]. M-CSF and RANKL cytokines, expressed by nearby stromal cells and osteoblasts, are essential for osteoclastogenesis: M-CSF stimulates the proliferation and prevents the apoptosis of early osteoclast precursors, while RANKL interacts with RANK receptor on monocytic osteoclast precursor cells, inducing the commitment to the osteoclast phenotype by triggering the recruitment of co-activators and thus activating the transcription of the macrophage genes cathepsin K and acid phosphatases. Osteoprotegerin (OPG), is a soluble decoy receptor to RANKL, also produced by mature osteoblasts, that binds and neutralize RANKL molecules preventing the osteoclastogenesis or survival of pre-existing osteoclasts [41, 56]. After osteoclasts have eroded to a particular distance, from the surface in cancellous bone to a particular depth, the majority of cells detach and die [51] (adapted from [55],[57]).

2.2. Coupling of bone metastatic niche: the metastatic vicious cycle

According to the “seed and soil” analogy of Paget, the mineral soluble bone-related growth factors enrich the bone microenvironment acting as an attractor and a perfect initial support for specific breast cancer cells [14]. Breast cancer cells extravasate from circulation to wide-channelled sinusoids of the bone-marrow cavity and travel to the endosteal bone surface – e.g. trabecular zones of long bone’s red marrow, sternum, pelvis, ribs and vertebrae [58]. Motility, survival and metastasis invasion is a multi-directional and vicious process that is managed through a molecular crosstalk between tumour cells, bone-resorbing osteoclasts, bone-forming osteoblasts and the organic bone matrix [58, 59].

Bone metastatic lesions are usually classified as osteolytic or osteoblastic [58]. Breast cancer metastases cause predominantly osteolytic lesions with an increase in osteoclast activity and subsequent bone destruction [60], while only approximately 15% exhibit an osteoblastic or mixed phenotype [4].

The entry of breast cancer cells into the bone microenvironment synergistically increases the complexity of cell-cell interactions – most of *in vivo* studies indicate that bone matrix loss associated with metastatic osteolysis is caused by an indirect tumour-induced activation of osteoclast resorption, and not by the direct effect of cancer cells that secrete proteolytic enzymes and acid in abundance to the environment [61].

Within the bone niche, tumour cells produce and secrete onto endosteal bone surface M-CSF as well as PTHrP and tumour necrosis factor-α (TNF- α), which activate RANKL and inhibit osteoprotegerin synthesis, amplifying the efficacy of RANKL and resulting in an intensified osteoclast maturation and thereby in a superior bone resorption [62]. In turn, the over-activation of osteoclast function releases an increased amount of sequestered growth factors of bone matrix, including IGF-1, TGF-β and BMPs that act upon the metastatic cells [4], enhancing their survival and growth while further stimulating PTHrP synthesis with a concomitant increased bone loss [58].

This creates a positive feedback cycle of increased bone loss and increased growth of the metastatic cells [58] (see the "vicious cycle of bone metastasis" in Figure I.5).

The metastatic niche model carries several implications for the clinical management of advanced malignancy. Understanding bone tumour microenvironment and how breast cancer cells influence bone tissue homeostasis, might be the key to discover potential new targets to diagnosis and therapies for bone metastasis-related diseases.

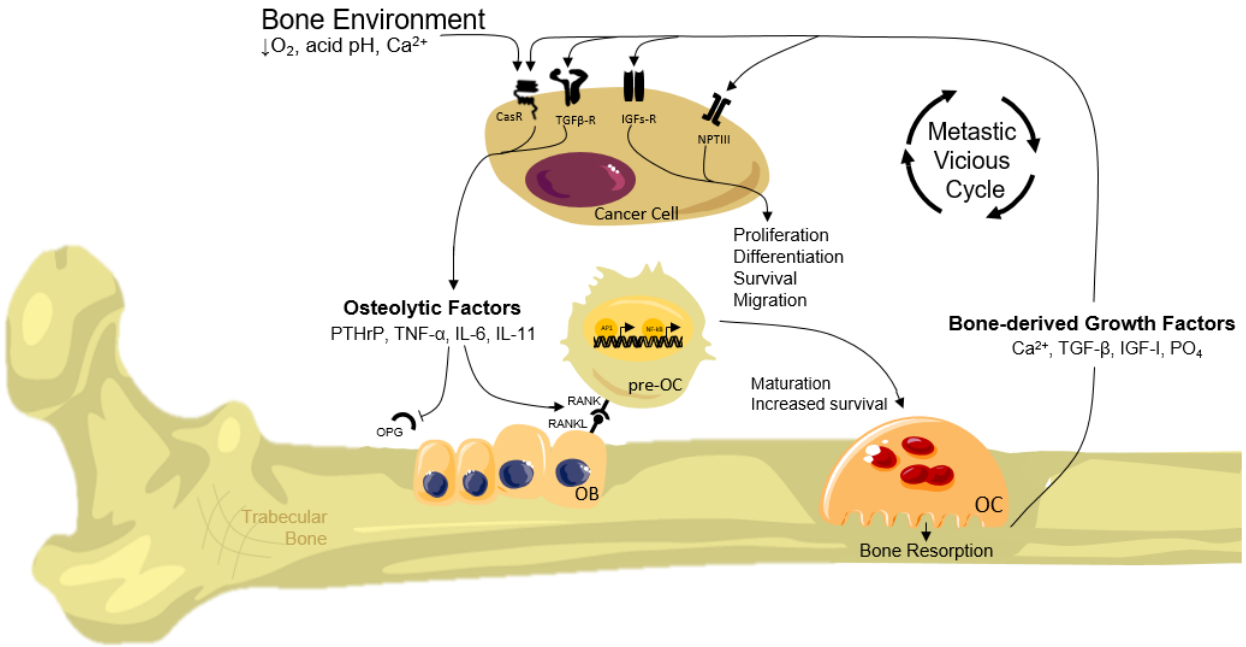

Figure I.5. Molecular and cellular interactions in the metastatic vicious cycle. In the new tissue, tumour cells can then enter in a state of dormancy or, when stimulated, can proliferate giving rise to micro- and macro-metastases. Often is the bone microenvironment itself that induce the tumour production of osteolytic factors such as PTHrP, tumour necrosis factor α (TNF-α), interleukin (IL)-6 and IL-11, which in turn stimulates osteoblasts and stromal cells to produce RANKL and while downregulate OPG. Signalling through RANK-RANKL in osteoclast progenitors activates transcription factors such as AP1 and NF-κB, accelerating their differentiation into mature osteoclasts. Osteoclast activation induces a significant bone resorption that leads to the releasing of bone-derived growth factor such as, TGF-β and IGF-1, and a simultaneous increase of calcium (Ca^{2+}) and phosphate (PO_4) concentrations. These factors are incorporated into cancer cells and while IGF-1 and PO_4 stimulate cancer cell proliferation, differentiation, migration and survival, TGF-β and Ca^{2+} stimulates the PTHrP production establishing a vicious cycle of destruction of bone mineralized tissue and a progressive tumour growth (adapted from [58]).

3. Cancer models: paradigm shift on novel research tools

Given that the majority of cancer-related deaths are due to metastatic disease, the molecular and cellular processes underlying metastasis continue to be a major focus of cancer research [63].

Indeed, the majority of cancer research for preclinical drug testing and mechanistic studies was, in the past decades, carried out through traditional two-dimensional (2D) tissue culture systems and/or animal models. However, only 5% of anticancer agents in preclinical development are licensed after demonstrating sufficient efficacy in phase III clinical trials [64], revealing a critical need to fulfil the research gap and translational priorities for the successful prevention and treatment of breast cancer with optimized preclinical models mimicking in a more accurate way the tumour microenvironment features – e.g. intrinsic cellular interactions, transport barriers and hypoxia conditions [65].

The inherent physical- and chemical-properties of each tissue structure strongly influences molecular pathways and, in consequence, determines cell viability, proliferation and function [66]. For instance, it is now evident that the mechanical and chemical properties provided by the extracellular matrix, the fluid supply conditions and the characteristic cell-to-cell interactions of each research model have a profound influence on the functional properties of tumour cells, strongly affecting their drug sensitivity outcome [14].

Accordingly, much effort is being devoted to improving the structural and cellular complexity of current *in vitro* models to resemble more faithfully the *in vivo* tumour microenvironment. The development of a mimicking cellular model is a very challenging task, due to the richness of issues that should be considered. Each model approach has its own features with particular advantages and limitations that should be taken into account to fill the microenvironment specific constraints (see Table I.2).

Table I.2. Properties of both *in vivo* and *in vitro* tumour models.

Model Type	Advantages	Disadvantages	Ref
In vivo models			
Zebrafish embryos	Large availability offspring Optical transparency	Phylogenetic distance	[67]
Athymic nude mice	Molecular and genetic similarity Suitable to genetic manipulation *In vivo* imaging technology	Time consuming process Expensive maintenance Ethical dilemmas	[68]
In vitro models			
2D platforms			
Cell monolayers	Simple and inexpensive Easily accessible	Lack of cell interactions Absence of gradients	[69]
Trans-wells inserts	Co-culture system Easily accessible	Lack of stromal organization Vertical compartmentalization	[70]
3D systems			
Spheroid aggregates	Cell-cell contact geometry Gradient transport barrier Scaffold-free culture Suitable for HTS Easily accessible	Limited flexibility Short-time experiments	[71]
Matrix- and scaffolds platforms	Cell-cell contact geometry Highly customizable Unique mechanic properties	Inhomogeneous cell distribution Difficult access to further analysis Biocompatible concerns	[72]
Microfluidic devices	Laminar flow conditions Cell compartmentalization Accurate monitoring control	Specialized equipment	[73]

Animal models are, currently, a vital part of research process, enabling investigations at the organism level in a physiological environment, allowing to study the systemic responses to anticancer drugs [74]. Nevertheless, the effects of the microenvironment on drug response can be highly inaccurate and misleading in predicting the therapeutic efficacy of anticancer drug in humans [75, 76], due to intrinsic divergence of molecular mechanisms between species and non-human stromal component of the tumour. These facts, along with enormous ethical concerns about animal experimentation are motivating governments and regulatory organizations to limit their use and support the implementation of alternative methods [77].

By other hand, culture of adherent cells on flat and rigid 2D substrates is a well-established *in vitro* technique playing also a pivotal role in mechanistic investigations. However, 2D monolayer culture does not represent the complexities of the dimensional *in vivo* environment. A major limitation of 2D cell culture is the violation of apical-basal cell polarity [69] and, consequently, their lack of dynamic interactions either between cells or between cells and subtract. Indeed, tissue-specific architecture as well as mechanical and biochemical cues are lost under such simplified conditions, ultimately modifying cellular function and response [78]. Establishing co-cultures into these systems can increase natural intercellular contact and communication, but the 2D surface geometry still inhibits the ability for cells to form a multidimensional structure. Furthermore, 2D cell culture are faced with significant transport limitations – cells grown in monolayers are exposed to a uniform environment with constant supply of oxygen, nutrients or even drug components that is being analysed [79], which can exert either stimulatory or inhibitory effects on tumour progression. Engineered technologies have also been developed to increase the complexity of those systems and improve the culture properties in order to better mimic physiological features – trans-wells technology is particularly suitable for cell migration assays and tumour cell invasion [70].

Three-dimensional (3D) cell cultures bridge the *in vitro* to *in vivo* gap by growing cells within a microenvironment that resembles tissue microenvironment avoiding the concerns related with animal experimentation [72]. Cellular spheroids are simple 3D systems of self-assembled cell colonies, which take advantage of the natural tendency of many cell types to aggregate. The self-organization of cells into spheroid structures re-establish biological mutual contacts and specific microenvironments – e.g. large development of tight junctions and gradients of nutrient concentration – that allow them to express a tissue-like phenotype [80]. This scaffold-free technique, although restrictive of tricky customization, generates homogeneous spheroids with consistent sizes and shapes due to their simplicity, reproducibility and similarity to physiological tissues. Alternatively, in order to physically support the cell growth, matrix and scaffolds platforms for 3D cell culture are available in a broad range of materials, which one with specific chemical and mechanical properties, such as adhesion sites distribution, porosity, permeability, and stiffness. Naturally derived matrix or scaffolds for cell culture are typically formed of proteins and extracellular matrix (ECM) components (e.g. collagen, hyaluronic acid, chitosan or alginate) with an inherent biocompatible and bioactivity. They also promote many cellular functions due to the presence of various endogenous factors, which can be advantageous for supporting viability, proliferation, function, and development of many cell types [72]. Synthetic polymers, such as poly(ethylene glycol) (PEG), polyacrylamide (PA) and poly(lactic-co-glycolic acid) (PLGA), are good choices for 3D cell culture applications when naturally-derived biological matrices are unsuitable. Although the processing of these materials requires extra-labour steps, the composition homogeneity is significantly increased and the range of controllable features is also amplified [81].

Microfluidics devices recently appear as a miniaturized tool imported from the microelectronics industry, from where it is possible to integrate different types of cultures onto compartments connected by microchannels that follows the fluidics laws, allowing a very precise and controlled reactor system ideal for the study of co-cultures communication [82].

3.1. Microfluidic laws: miniaturized engineering flows in biology

During the past decade there has been tremendous development in both science and technology field of miniaturized fluid handling systems to the micrometre range, offering fundamentally new and revolutionary capabilities in the control of molecules gradients into space and time [82].

Microfluidics concept was introduced in biology in the late 1970s through the adoption of fabrication technologies developed in microelectronics industry [82], but it was in 1990s that the miniaturization of cellular systems received the contemplation of scientific community with the work of Manz *et al* [83] with a dramatic growth since then, partly due to increasing popularity of microscale analytical chemistry techniques and the development of microelectronic technologies.

Although a reduction in size to the micrometre scale will usually not change the nature of molecular reactions, laws of scale for surface per volume, molecular diffusion and heat transport enable dramatic increases in throughput. Giving the dependence of reaction parameters on the size of the system, various opportunities can emerge from miniaturization of reaction systems (see Figure I.6).

The most obvious characteristic is the low volume consumption requirement that makes them more suitable for drug testing against rare primary cell populations, such as biopsies and decreases the amount of chemoattractants or therapeutic agents needed, reducing the cost of reagents [84]. Moreover, the small size of the microfluidic devices themselves allows the parallelization of applied methods to a large numbers of conditions that can be observed simultaneously under comparable conditions [85].

Due to the high surface to volume ratio provided by the small distances of microchannels, the diffusion rate of mass and heat is increased and is performed under a laminar flow enabling an accurate control of these systems and, therefore, an access to physical mechanisms that are inaccessible on the 2D cell migration assays [82]. In fact, the generation of concentration gradients based on microfluidic assays was already used for cell-based on-chip toxicological studies [86], gene expression studies [87] and chemotaxis studies [88].

Tightly linked to miniaturization technology is the further enhance of imaging and detection sensitivity, particularly in fluorescence spectroscopy, enabling real-time measurements of small compound out of a flowing bulk sample, due to the inherent reduction of reaction volume [89].

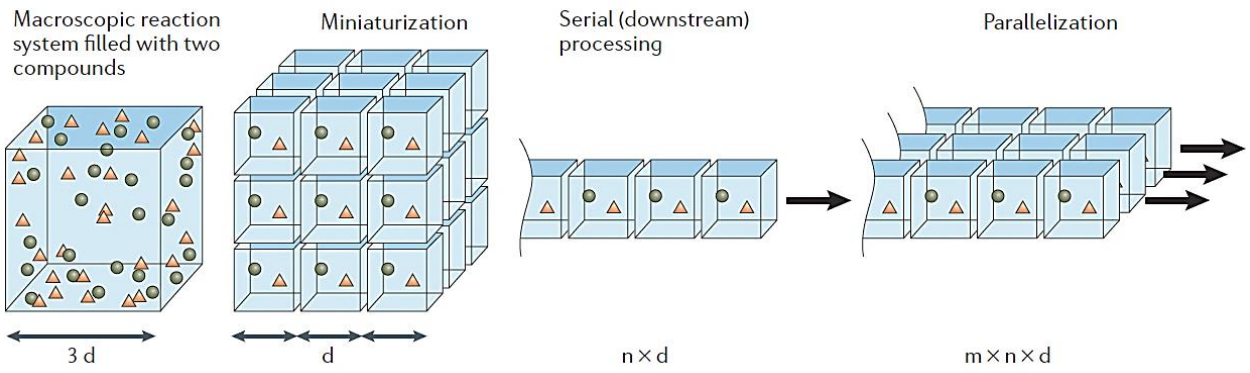

Figure I.6. Miniaturization impact on reaction systems. One key feature of microfluidics is the integration of different functional units for reaction, separation and detection in a channel network. Due to the short distances in microfluidic channels, the transport times of mass and heat are shortened. So that, fast and precisely controlled compound concentration and temperature supply is facilitated due to high surface to volume ratio. Furthermore, because space is used sparingly, massive parallelization can be accomplished (adapted from [85]). Abbreviations: d - length of edge; n and m - numbers of reaction systems serial and parallel, respectively.

As the dimensions of the microfluidic devices are reduced, some physics characteristics are different compared to conventional laboratory-scale assay. For instance, physics laws for fluids are different from laws at macroscopic scale, resulting in laminar fluid flows where the viscosity effects overcome inertia forces – which from a physics point of view is pointed out by a low Reynolds number, leading to a drastic simplification of the complex Navier-Stokes equations describing fluid mechanics (see Figure I.7) [90, 91].

Consequently, the fluid mechanics could be highly tailored by the geometrical and the chemical features of the channels network as well as by the driving force imposed to the system, which can be achieved either through pressure gradients between both compartments or through external electric or magnetic fields [92].

Multiple formats and geometric designs are now available commercially, and there are several options that can be adapted or optimized for each specific application.

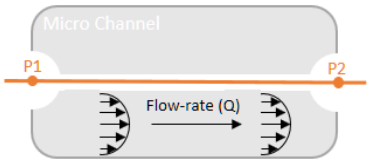

$$P1 - P2 = R \times Q$$

$$\text{Resistance} = \frac{12\,\mu \times L}{h^3 \times w}$$

L : length of the microchannel (L>>w)
h : height of the microchannel
w : width of the microchannel (w>> h)
μ : dynamic viscosity of the fluid

Figure I.7. Physic laws of microfluidics laminar flow dependence. Microfluidic flow-rate can be deduced based on the electrical analogy (Ohm's law): the flow-rate of the fluid is function of the pressure gradient between the two compartments and the resistance of the channel, that is given by its geometric characteristics and by the dynamic viscosity of the fluid (adapted from [93]).

3.1.1. Microfluidic 3D models of cancer: cells interaction over fluidics

The integration of microfluidics and cell biology research has recently reached another significant milestone with the development of "organ-on-a-chip" technologies, where it is possible to engineer living cellular microsystems that behave and function like their counterparts *in vivo* [94].

Cancer research in particular has potential to reap enormous benefits from the application of organ-on-a-chip technologies. A major challenge in cancer research has been the need to develop more accurate, informative and predictive experimental models of human tumour development than those currently available. Importantly, the role of the tumour microenvironment in cancer initiation and progression, and the recognition that a tumour itself should be considered a complex organ, suggests that physiological microenvironments with improved relevance to humans and perhaps even organ-level complexity are integral to our understanding of the disease, and must be taken into consideration in the design of future methodologies of experimental research [95].

The spatiotemporal resolution is, therefore, one of the main breakthrough of microfluidic compartmentalized devices, enabling the analysis of physical and biochemical dependences and interactions on chemotaxis of tissue-specific cells and/or their cytotoxic effect on anticancer therapies. These platforms increase the understanding about the interplay among the biochemical transductional pathways that regulates cancer development and progression, therefore creating a promising tool to identify and validate the efficacy and safety of potential biophysiological clues and therapeutic targets early in the pipeline in order to increase the likelihood of success in clinical trials [84, 89].

Indeed, microfluidics technology is emerging as a novel and valuable *in vitro* platform to the study of cellular interactions within a particular scenario. These platforms offer various advantages over traditional *in vitro* systems, including more complex geometries, better spatiotemporal control of microenvironmental factors and stimuli, added functionality, and increased throughput analysis [96]. Moreover, unique properties of the microenvironment can be designed and controlled through the assemble of a proper design of microchannels geometry and the incorporation of tissue engineering principles into microfluidic 3D *in vitro* cancer models (see Table I.3) – i.e. the evolution of models that recapitulate tissue- or organ-level structures (e.g. mechanical and chemical unique properties) and functions while still allowing efficient and expansive investigation of the dynamics in tumour microenvironments [97].

The purpose of developing improved experimental models through organ-on-a-chip technologies is to accelerate progress in fundamental research, to increase efficiency in drug discovery and to advance the translation of new knowledge into clinical outcomes. Continued development and integration of microtechnology with 3D cancer biology has provided a variety of compartmentalized structures, leading to the creation of more accurate devices that closely mimic the *in vivo* environment and are highly suitable to study cancer cells migration, invasion and molecular interplay with surrounding cells, which conduct to more comprehensive analyses on aspects of cell migration such as migration rate, morphology and different sub-populations of cells on the tumour microenvironment [98].

Table I.3. Summary of microfluidic technology for studying breast cancer biology.

Focus of study	Cell types	Novel features	Ref
Spheroid formation	Human breast cancer (MCF-7)	Continuous perfusion	[99]
ECM remodelling	Human breast carcinoma (MB-MDA-231) Mouse macrophage (RAW 264.1)	Collagen- I or Matrigel matrix 3D co-cultures	[100]
Tumour Invasion	Mouse mammary tumour (4T1) Human dermal microvascular endothelial (HDMEC)	Continuous perfusion Induced hypoxia	[101]
Tumour Invasion	Mammary epithelial cells (MCF-DCIS) Human mammary fibroblasts (HMFs)	Spatial-temporal examination Adaptable channel design Surface-tension pumping	[102]

Aims of the project

The aim of the current work is to develop an *in vitro* breast cancer bone metastasis model using a microfluidic platform.

In order to achieve this prime goal, this project includes 3 complementary tasks:

1. *Optimization of breast cancer cells culture.*

The system will be elevated using two distinct cancer cell lines: MCF-7 and MDA-MB-231. The optimized culture conditions will be studied in order to achieve spheroidal structures reassembling the *in vivo* tumour organization.

2. *Optimization of human Osteoblast/Osteoclast co-cultures.*

The optimization steps to achieved a complete independent co-culture system will mainly rely on the establishment and improvement of cells derivation and differentiation methods – osteoblasts will be differentiated from a human Mesenchymal Stem Cell lineage; whereas human osteoclasts will be retrieved from the differentiation of peripheral blood monocytes of healthy blood donors, in compliance with protocols established by the National Blood Institute.
The bone co-culture system will be assembled in a calcified bone-like substrate in order to reassemble the organic and inorganic bone ECM microenvironment.

3. *Establishment of breast cancer-bone cells microfluidic tri-culture.*

This final step will be mainly focused on optimization of platform design as well as the assessment of co-cultures viability within the microfluidic chambers as well as the crosstalk effect between the pairwise cells.

It is envisaged that this model will be a useful tool to study the signalling pathways intrinsic to the bone metastatic niche and also to be part of a drug-screening platform to assess the efficiency of potential therapeutic drugs in the pre-clinical phase.

Chapter II

Materials and Methods

Experimental Overview

1. Cell Cultures

1.1. Breast cancer cells

1.1.1. Formation of Breast Cancer spheroids

1.1.2. Characterization of Breast Cancer spheroids

1.2. Bone Cells Co-cultures

1.2.1. Human Osteoblast Cultures

1.2.2. Human Osteoclast Cultures

1.2.3. Osteoblast/Osteoclast co-cultures

2. Microfluidic systems

2.1. Preparation of the microfluidic devices

2.2 Microfluidic cultures

3. Statistical analysis

Chapter II

Materials and Methods

Experimental overview In the present study, it was followed a step-by-step process for the development of a microfluidic platform that mimics breast cancer bone metastatic niche. First, specific cell culture protocols were optimized and characterized for both breast cancer cells and osteoblast/osteoclast co-cultures. Finally, the optimized culture conditions were transferred in each compartment of the customized microfluidic chamber and the interactions analysed between them.

1. Cell Cultures

1.1. Breast cancer cells

1.1.1. Formation of Breast Cancer spheroids

Cell culture MCF-7/AZ and MDA-MB-231 breast cancer cell lines were seeded on top of non-adhesive surfaces. Briefly, cells were detached from culture flasks with 0.25% trypsin and resuspended in ice-cold medium supplemented with 10% Fetal Bovine Serum (FBS) (Gibco), 10 U/mL Penicillin and 10 µg/mL Streptomycin. DMEM/F12 medium (without phenol-red, Gibco) and DMEM-high glucose medium (Gibco) were used for MCF-7 and MDA-MB-231 cells, respectively. Using a manual precision dispenser, the cell suspension was seeded into the surfaces at 3 different cell densities: 1.5 x 10^4 cells/mL (3 000 cells per well), 2.5 x 10^4 cells/mL (5 000 cells per well) and 5.0 x 10^4 cells/mL (10 000 cells per well). The cells were kept at 37ºC and 5% CO_2, and cell media changed on day 4. Their ability to form the spheroidal conformation was assessed after 4 and 7 days of culture.

Non-adhesive surface coatings In order to obtain a liquid-overlay culture system the 96-well flat-bottom plate surfaces were coated with non-adhesive polymers: poly-HEMA (Sigma) or agarose (Lonza). Uncoated TCPS surfaces were used as control. Poly-HEMA coating solution was prepared from a stock solution of 120 mg/mL to a final concentration of 5 mg/mL in 96% sterile ethanol. The coating solution was filtered (0.2 µm) and 60 µL was dispensed in each well. The plates were left inside of a sterile hood for 72h at room temperature (RT) to allow a slow evaporation of the solvent. Alternately, the agarose solution was prepared at 1.5% (w/v) in sterile DMEM/F12 without phenol-red (Gibco) and melted to allow the dissolution of the polymer. The solution was kept at 60ºC in a water-bath until use. 50 µL of agarose gel was dispensed in each well and the plates were left to cool down at RT for 20 min to allow agarose gelification.

Medium additives An aliquot of rBM (Corning) was thawed overnight and added to cell suspension at a final concentration of 2.5% (v/v) with ice-cold pipette tips. Complete medium without the rBM was used as control for each condition.

Forced aggregation Based on the agitation-based methods, plates were centrifuged at 1000 rpm for 10 min at 4ºC immediately after the seeding step, in order to mechanically induce the spheroid formation in the central area of the well.

1.1.2. Characterization of Breast Cancer spheroids

Spheroids quantitative analysis The morphology of the aggregates was assessed using a high-throughput scan (InCell Analyzer 2000, GE Healthcare). Shape descriptors were further analysed on the IN Cell Developer Toolbox 1.9.2 (GE Healthcare) software. The frequency of (1) number of aggregates formed per well, (2) the diameter of each structure, their (3) area, (4) perimeter and (5) aspect ratio for each condition, were statistically evaluated. In order to evaluate the precision and feasibility of the spheroids formed by this method, it was performed an extended analysis of 50 spheroids. The ideal conditions for each cell line were further selected.

Morphological analysis Each spheroid was firstly transferred into a multi-well µSlide (Ibidi) and every step was performed under a stereomicroscope to ensure the integrity of the structure. Briefly, after removing the medium, cells were washed twice with phosphate-buffered saline (PBS), followed by cell fixation with paraformaldehyde (PFA) (Sigma-Aldrich) 4% (w/v) for 10 min at RT. Cells were then washed again with PBS and permeabilized with ice-cold Triton X-100 1% (v/v) (Sigma-Aldrich) for 5 min at 4ºC. After washing twice with PBS to remove any remaining excess, cells were incubated with 1% (w/v) Bovine Serum Albumin (BSA) (Sigma-Aldrich) in PBS for 1 h at 37ºC to block antibody unspecific binding. Cells were then incubated with Alexa-Fluor 488 Phalloidin (Thermo Fisher) 1:100 in PBS for 20 min at RT in the dark. At the end of the incubation time, cells were washed again with PBS and stained with a Hoechst 33342 (Thermo Fisher) diluted solution in PBS at a final working concentration of 1 µg/ml. The samples were kept at 4ºC in the dark until further analysis in a Leica TCS SP5 Confocal Microscope (Leica Microsystems, Inc.). Two representative images were acquired for each cell line, with a resolution of 2048x2048 pixels and a z-step of 5 µm. The image projection in z-axis was obtained in Fiji (ImageJ Software).

Cryostat sections A total of 5 spheroids were pooled on a net sheet of about 1cm^2 and embedded in an OCT block (NEG50, Richard Allan Scientific). Samples were frozen and stored at -80ºC until sectioning. Microtone sections of 7 µm thickness were harvested sequentially from each block, using a Micron HM 550 cryostat (Thermo Fisher Scientific) at a cabinet temperature of -20ºC, and placed on SuperFrost glass slides (WWR International). Spheroids were then fixed and stained with Alexa-Fluor 488 Phalloidin and Hoechst 33342 as previously described. The slides were preserved in a Fluoromount™ Aqueous Mounting Medium (Sigma) and analysed under a Leica TCS SP5 Confocal Microscope (Leica Microsystems, Inc.) with a resolution of 2048x2048 pixels and a z-step of 1 µm.

Live-Dead staining Each individual spheroid was transferred into a multi-well µSlide and washed twice with warm PBS to reduce unspecific binding. The spheroids were stained within the wells with 1:5000 diluted Calcein AM (Invitrogen) of a stock solution at 1 mg/ml for 20 min at 37ºC in the dark. Followed by a washing step with PBS, the spheroids were then incubated for 5 min at RT with of propidium iodide (PI, Sigma-Aldrich) at 1mg/ml diluted 1:500. The spheroids were washed again with PBS in order to remove every remaining excess of PI and were then individually scanned under a Leica TCS SP5 Confocal Microscope (Leica Microsystems) with a resolution of 1024x1024 pixels and a z-step of 5 µm. Two representative images were acquired for each cell line, and the image projection in z-axis was obtained in Fiji software.

Quantitative apoptosis analysis 10 spheroids per condition were pooled into a microtube, centrifuged at 400 g for 3 min and the media removed. Samples were washed once with PBS, resuspended in accutase solution (Gibco) and incubated at 37ºC. Every 5 min, spheroids were mechanically dissociated by pipetting and the dissociation was complete within 15 min. Single-cell suspension was centrifuged, resuspended in 1x Binding Buffer (BD Pharmingen) and 1 x 10^5 cells transferred into a 96-well conical-bottom plate. Each condition was then stained with FITC Annexin-V and PI (BD Pharmingen) for 20 min at RT in the dark. Cells were washed with PBS, filtered and analysed by flow cytometry analysis (FACS Calibur, BD Biosciences). Unstained and single-stained cells with FITC Annexin-V or PI were used to set up the compensation and quadrants.

Gene expression analysis The RNA extraction was performed immediately after culture. Each spheroid was lysed with 100 µl of TRIzol reagent (Life Technology) for 1 min and collected into a microtube. From 3 up to 10 homogenate spheroids were pulled together and stored at -80ºC until further usage. RNA was purified using a Direct-zol RNA Miniprep kit (Epigenetics) accordingly to manufacturer's instructions. Briefly, 1 volume of pure sterile ethanol was added to the sample homogenate, mixed and loaded directly into a Zymo-Spin IIC Column in a Collection Tube. A series of washing procedures with Washing Buffers followed by centrifugation at 12000 rpm for 1 min were performed. The RNA was eluted using DNase/RNase-Free water and the total RNA concentration and purity were determined using a Nanodrop ND 1000. RNA quantity was normalized to 250 ng and filled up to 8 µL with DEPC-treated water.

Complementary DNA (cDNA) synthesis was carried out using NZY First Strand Synthesis Kit (NZYtech) through an incubation period of 10 min at 25ºC followed by a 30 min at 50ºC in a Thermocycler (Biometra). The reaction was then inactivated by heating at 85ºC for 5 min, followed by chilling on ice. 1 µL of RNase H was added to each tube and incubated at 37ºC for 20 min to eliminate reminiscent RNA. cDNA was stored at -20ºC. Quantitative realtime-PCR (RT-PCR) was performed using 1 µl of cDNA as a template and adding 19 µl of a master mix containing the specific primer pairs.

Primers of genes involved in bone remodelling process and homeostasis (VEGF, RANK, and RANKL) was designed in NCBI/Primer-BLAST to amplify and detect the expression profile of cancer cells in metastatic niche. Three reference genes were tested: Beta-2-microglobulin (B2M), Histone H2A (HIST) and Tyrosine 3-monooxygenase (YWHAZ). The corresponding primer sequences are summarized in Table A.1, in annexes.

The PCR protocol used is described in Figure II.1. The resulting PCR products were analysed using the iQ5 software (Bio-Rad) and the expression of the markers was normalized using the ΔCT method to a B2M reference gene.

In addition to the melting curve analysis, the specificity of the PCR product was evaluated by the size analysis of the PCR fragment in comparison with a GeneRuler Low Range DNA Ladder (Thermo Scientific) through agarose gel electrophoresis. After completed quantitative RT-PCR run, 20 µl of the reaction mix containing the PCR product was directly applied onto a 3% agarose gel containing Red-safe (iNtRON Biotechnology) and allowed to run for 1h in a gel Power Base (Bio-Rad). The gel was then photographed under UV light, using a GelDoc EZ System (Bio-Rad) in order to validate amplification products sizes.

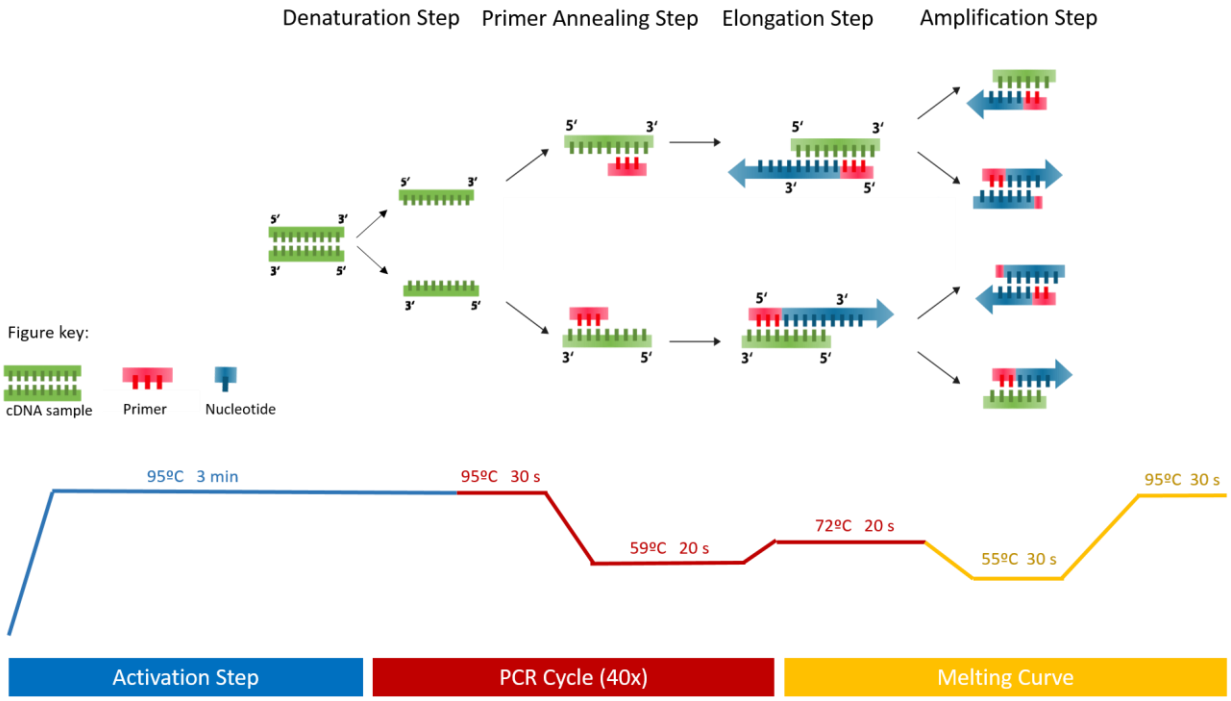

Figure II.1. Polymerase Chain Reaction Protocol An initial activation step at 95ºC for 3 min was followed by 40 PCR amplification cycles, each run with a denaturation step at 95ºC for 30 s, an annealing step at 58ºC for 20 s and an elongation step at 72ºC for 20 s. The procedure was finished with the acquisition of the melting curve with a set point at 55ºC with a 0.5ºC step increment until the end temperature of 95ºC.

1.2. Bone Cells Co-cultures

1.2.1. Human Osteoblast Cultures

Cell culture Human Mesenchymal Steam Cells (hMSCs) (Lonza) were cultured at 37°C under a 5% CO2 humidified atmosphere and expanded in basal medium: DMEM low glucose (Gibco) supplemented with 10% FBS (Gibco), 10 U/mL Penicillin and 10 µg/mL Streptomycin. For differentiation experiments, confluent hMSCs (at a passage not higher than 11) were detached with 0.05% trypsin-EDTA (Gibco) and resuspended in osteogenic medium in a density of 10^5 cells/mL. Four combinations of osteogenic factors were tested in order to assess the condition that induces a better and faster osteogenic differentiation of hMSC. The experiments were performed over 14 days and the medium was changed twice a week. A brief overview of the experiment workflow is summarized in Figure II.2.

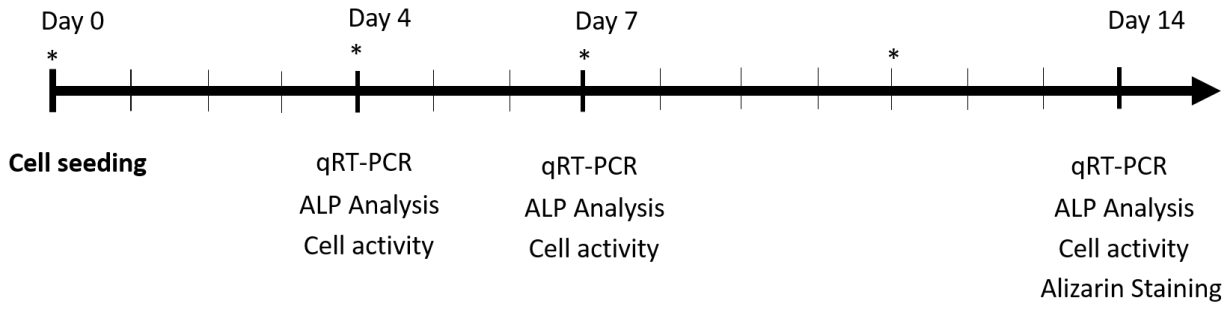

Figure II.2. Planning time-line of osteoblastic differentiation experiment. The differentiation process of hMSCs was evaluated through 14 days of culture. The osteogenic supplemented media were changed twice a week marked with (*) symbol in the figure. Cell activity and gene expression were evaluated on day 4, 7 and 14. Mineralization markers were assessed on specific time-points either by staining procedures and quantification protocols.

Cell viability Cell metabolic activity was evaluated by resazurin (Sigma) assay and compared to the quantity of DNA using Quant-iT PicoGreen dsDNA kit (Molecular Probes). Both examinations were performed simultaneously at 4, 7 and 14 days of differentiation. For each time-point, the resazurin solution was added to the culture media at 10% (v/v) and incubated for 3h at 37ºC in the dark. The viability was quantified by measuring the relative fluorescence units (RFU) with an excitation at 530 nm. Afterward, samples were lysed by 1h incubation in Triton X-100 1% (v/v) (Sigma-Aldrich) in ice and with agitation followed by the incubation with the PicoGreen fluorescence reagent, accordingly to the supplier' indications. DNA standards were prepared using the same procedure. Fluorescence was measured with an excitation at 480 nm and sample values were calculated using DNA standard curve.

ALP staining At different stages of osteoblast differentiation, the medium was removed from the wells and cells were washed with PBS, twice. After fixing the cells with 4% (w/v) PFA for 10 min, cells were washed with pure water and ALP substrate (4% Naphthol AS-MX phosphate alkaline solution (Sigma) in Fast Violet B solution (Sigma)) were added to the wells and left incubating for 45 min. After incubation, cells were washed with pure water twice and left to air dry. Three replicates for each condition were photographed using a Stereomicroscope (SZX10, Olympus) coupled to a digital camera (DP21, Olympus) and the ALP-positive cells were qualitatively evaluated.

ALP quantification In order to quantify the levels of ALP production, samples were lysed with 1% (v/v) Triton X-100 (Sigma) as previously described for DNA quantification. A colorimetric assay was performed, by the incubation of samples with ALP substrate (p-nitrophenyl phosphate in sodium bicarbonate buffer with $MgCl_2$) for 1 h, at 37ºC in the dark. The hydrolysis of p-nitrophenyl phosphate was stopped with 0.02 M of NaOH and absorbance was read at 405 nm. A standard curve was prepared using standard solutions of p-nitrophenol and the ALP activity quantification was determined in mol/min. Enzyme activity was normalized to cell protein content measured using the Bio-Rad DC Protein Assay kit (Bio-Rad) and following the manufacturer's instructions.

Alizarin Red staining and Quantification The medium was removed and the cells were washed twice with cold PBS. Cells were then fixed in ice-cold 70% ethanol for 1 h at -20ºC and allowed to air dry. The wells were washed twice with water and stained with freshly prepared 2% (w/v) alizarin red (Sigma) solution in water (pH 4.2) for 15 min at RT with gentle agitation. After washing the wells twice, the samples were photographed using a Stereomicroscope (SZX10, Olympus) coupled to a digital camera (DP21, Olympus). The stain was eluted with 10% (w/v) cetylpyridinium chloride (CPC)(Sigma) in sodium phosphate solution (pH 7.0) for 20 min at RT on gentle agitation. The absorbance was measured at 570 nm and compared to an alizarin red standard curve.

Gene Expression analysis The gene expression was assessed through the complementary DNA analysis from the RNA extracted from the samples as described before for breast cancer cells. Three replicates of each condition were pooled and qRT-PCR were performed for several genes known to be involved in osteogenic differentiation process, such as collagen type 1-alpha (COL1A1), VEGF, Osterix (OSX), bone sialoprotein (IBSP), runt related transcription factor 2 (RUNX2), osteocalcin (OCN), ALP and RANKL. The housekeeping gene B2M was used as the reference gene. The corresponding primer sequences are summarized in Table A.1, in annexes.

1.2.2. Human Osteoclast Cultures

Cell isolation Human blood monocytes were isolated from buffy coats (5-6 mL each, Figure II.3 -A) obtained from healthy donors gently provided by the Hospital São João, under a protocol approved by i3S ethical committee. The buffy coats were firstly diluted in PBS (Figure II.3 -B) and carefully layered over Ficoll-Paque PLUS (GE Healthcare) solution (Figure II.3 -C). After centrifugation (900 g for 20 min at RT and without brake) a density gradient was created in order to collect the peripheral blood mononuclear cells (PBMCs) layer in the interphase between the plasma and the Ficoll-Paque PLUS solution (Figure II.3 -D). The PBMCs were then washed 2x in PBS, isolated by centrifugation (900 g for 12 min at RT and with brake) and resuspended in incubation buffer (0.5% Biotin-free BSA (Sigma) in PBS with 2 mM EDTA (Invitrogen)). The PBMC initial suspension was then enriched with CD14-positive cells by magnetic separation by incubation with BD IMag™ Magnetic Particles conjugated with anti-Human CD14 antibody (BD Biosciences, Figure II.3 -E). Cell suspension was left to rest for 30 min at RT in order to incorporate de beds and was then put under an EasySep extremely strong magnet (StemCell) for 8-10 min (Figure II.3 -F). The supernatant was discarded, cells were gently washed with incubation buffer and the process repeated again twice.
The enrichment step efficiency was evaluated by the FACS analysis. 10^5 cells were stained with APC-CD14 antibody (ImmunoTools) before and after the separation. Unstained cells and stained cells with APC isotype were used as negative control.
The positive fraction was then resuspended in α-MEM (Gibco) with 10% HyClone FBS (GE Healthcare) and 10U/mL Penicillin and 10µg/mL Streptomycin, supplemented with M-CSF (R&D Systems). The flasks were incubated at 37ºC with 5% CO2 and the supplemented medium with 25ng/ml M-CSF and 25ng/ml RANKL (R&D Systems) was changed twice a week as described in Figure II.3 -G.

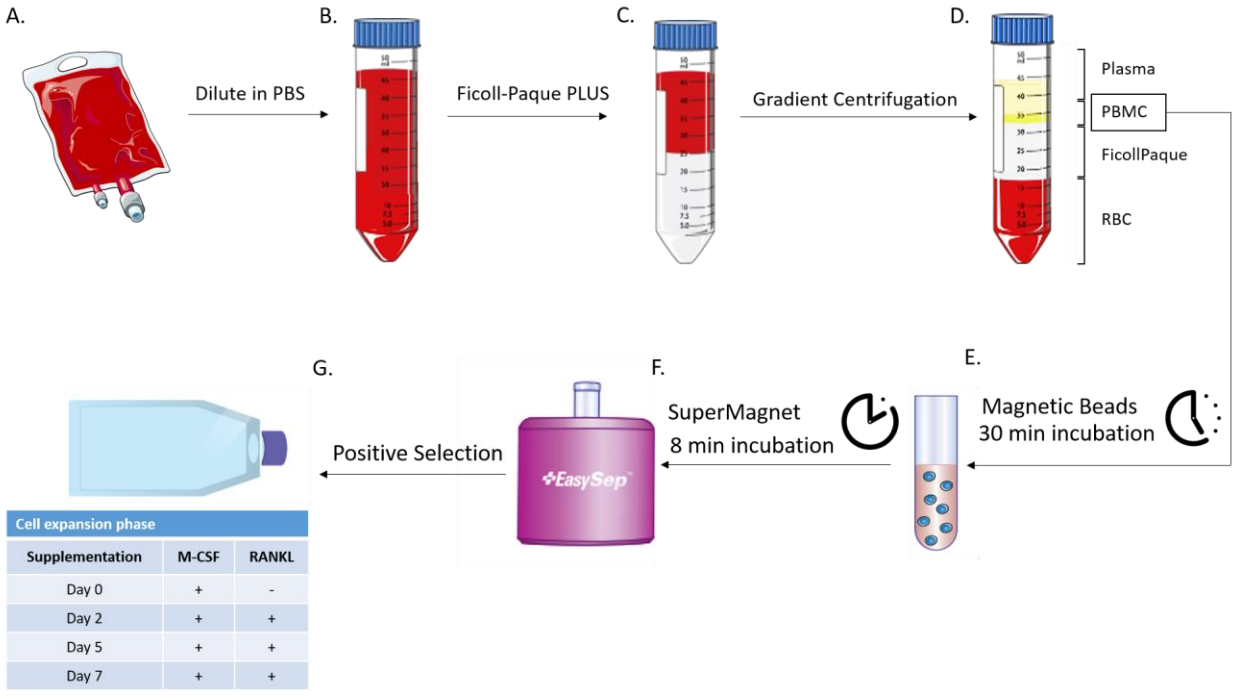

Figure II.3. Workflow of isolation of human CD14 positive monocytes from whole blood. After the isolation process, CD14+ monocytes were incubated at 37ºC with 5% CO_2. On day 2 the culture medium was collected, centrifuged and the reaming cells were resuspended and placed again in the culture flask. The medium was completely removed and replaced with fresh osteoclastogenic medium every 3 days thereafter.

Cell seeding Pre-osteoclasts were detached with accutase solution (Gibco) for 10 min and seeded on top of dentine discs (5 mm of diameter and a nominal thickness of 0.3 mm, IDS) at a cell density of 1.2 x 10^5 cells/well and allowed to generate resorption pits for 72 h. Before seeding, sterile dentine discs were carefully transferred to a 96-well plate and pre-wetted with complete α-MEM medium for at least 1 h at 37ºC. At the end of experiment, conditioned media was collected and stored at -80ºC until further analysis.

TRAP Staining TRAP staining was performed using a Leukocyte Acid Phosphatase Kit (Sigma) according to manufacturer's instructions. Briefly, cells were washed with PBS and fixed with Citrate/Acetone Solution for 30 s at RT. Cells were then rinsed with deionized water, air dried and incubated with warm TRAP Solution (water, acetate, naphtol, tartrate and 1 capsule of fast garnet salt GBC) for 1 h at 37ºC in the dark. After washing with water, cells were incubated with Acid Hematoxylin solution for 5 min at RT. Finally, samples were washed with water and allowed to air dry. The presence of TRAP-positive multinucleated cells was analysed on the Inverted Fluorescence Microscope (Zeiss Axio Vert), and representative images were acquired with AxioCam HRc (Zeiss) and using AxioVision SE64 Rel. 4.8. software. Osteoclast cultured on TCPS surfaces were used as a control.

Morphological analysis The cell morphology arrangement was evaluated through an immunostaining of F-actin and nuclei with Alexa-Fluor 488 Phalloidin (Thermo Fisher) and Hoechst 33342 (Thermo Fisher) as previously described for breast cancer cells. The pictures were acquired with AxioCam HRc (Zeiss) and using AxioVision SE64 Rel. 4.8. software. Osteoclast area measurements were performed using the "measure outline" tool of the AxioVision SE64 Rel. 4.8. software.

Scanning electron microscopy (SEM) analysis Osteoclast cultured on dentine discs were washed with PBS buffer at RT and 2.5% (v/v) glutaraldehyde in 0.1 M sodium cacodylate solution was added to each well. Fixation was performed at RT for 30 min under gentle shaking (50 rpm), in an orbital shaker. Samples were then washed three times with cacodylate buffer. Finally, cells were incubated for 10 min in each of a serial dilution of ethanol solutions 50, 60, 70, 80, 90 and 99% (v/v) to dehydrate samples, and stored in absolute ethanol at 4ºC, until being critical-point dried and mounted onto appropriate supports with araldite glue. Samples were then sputtered-coated with Au/Pd thin film for 80 s, using the SPI Module Sputter Coater equipment and examined using a High-Resolution Scanning Electron Microscope with X-Ray Microanalysis (JEOL JSM 6301F/ Oxford INCA Energy 350 at CEMUP facilities).

3D Reconstruction of resorption pits After washing with PBS, dentine discs were incubated in a 2mM EDTA solution in PBS for 10 min at 37ºC to remove adherent cells. Dentine discs were then washed thoroughly with PBS and stained with 10 µg/mL calcein AM (Invitrogen) in PBS for 30 min in the dark at RT, washed in PBS, allowed to air dry and stored at 4ºC until further analysis. Stacked images were obtained using a Leica TCS SP5 Confocal Microscope (Leica Microsystems, Inc.) at a resolution of 1024x1024 pixels with a 20x oil objective with a voxel size of 0.3662x0.3662x2.849 µm. Resorption pit 3D reconstruction was performed with Matlab 2013a (MathWorks, USA) using the BonePit algorithm [103]. Stacked images of individual pits were loaded into the program and the resorption pit outline was manually inputted in every stack. A mask containing every outline was then generated and used to reconstruct the resorption pit and to calculate the resorption pit volume, depth, top section area and aspect ratio.

Zymography Stacking gels were 5% acrylamide (Bio-Rad) and resolving gels were 10% acrylamide gels containing 0.1% of gelatine (Sigma-Aldrich). Protein content was quantified with the Bio-Rad DC Protein Assay kit (Bio-Rad) for each sample. Samples (18 µg) were mixed with sample buffer (SDS 0.1% plus 0.04% sucrose in Tris buffer 0.25 M, pH 6.8) and loaded to gelatine-SDS polyacrylamide gels. Precision Plus Protein™ Dual Color Standards (Bio-Rad) were used as protein standards. The gels ran at 80 V until the marker for 25 kDa reached the bottom of the resolving gel. Gels were then washed twice with a solution of 2% Triton X-100 (Sigma-Aldrich) for 30 min in agitation and once with distilled water (dH_2O) for 5 min and were left incubating overnight in MMP substrate buffer (50 mM Tris-HCl, pH7.5; 10 mM $CaCl_2$), at 37ºC under gently agitation. After incubation, the gels were washed with dH_2O, stained with a Coomassie Blue solution for 30 min under agitation and washed with dH_2O until the bands were clear. Gels were scanned in a GS800 calibrated densitometer (Bio-Rad) and analysed with Quantity One version 4.6.9 software (Bio-Rad).

Gene Expression analysis The gene expression was assessed through the complementary DNA analysis from the RNA extracted from the samples as described before. Three replicates of each condition were pooled and qRT-PCR were performed for several genes known to be involved in osteoclastogenesis, such as RANK, TRAP, CtsK, CTR, NFATc1, and c-FOS. The housekeeping gene B2M was used as the reference gene. The corresponding primer sequences are summarized in Table A.1, in annexes.

1.2.3. Osteoblast/Osteoclast co-cultures

Cell culture After the optimization of osteoblast differentiation protocol and the blood-derived mononuclear cells isolation method established, the co-culture system between both cells was assembled and the optimized conditions were further investigated. hMSCs were seeded on top of dentine discs at a cell density of 2 x 10^4 cells under osteogenic differentiation for 14 days. At 14 of differentiation, 1.2 x 10^5 pre-osteoclasts (previously isolated) were seeded on top of differentiated hMSCs. The co-culture was supplemented with the osteogenic factors (without M-CSF and RANKL) for further 72h.

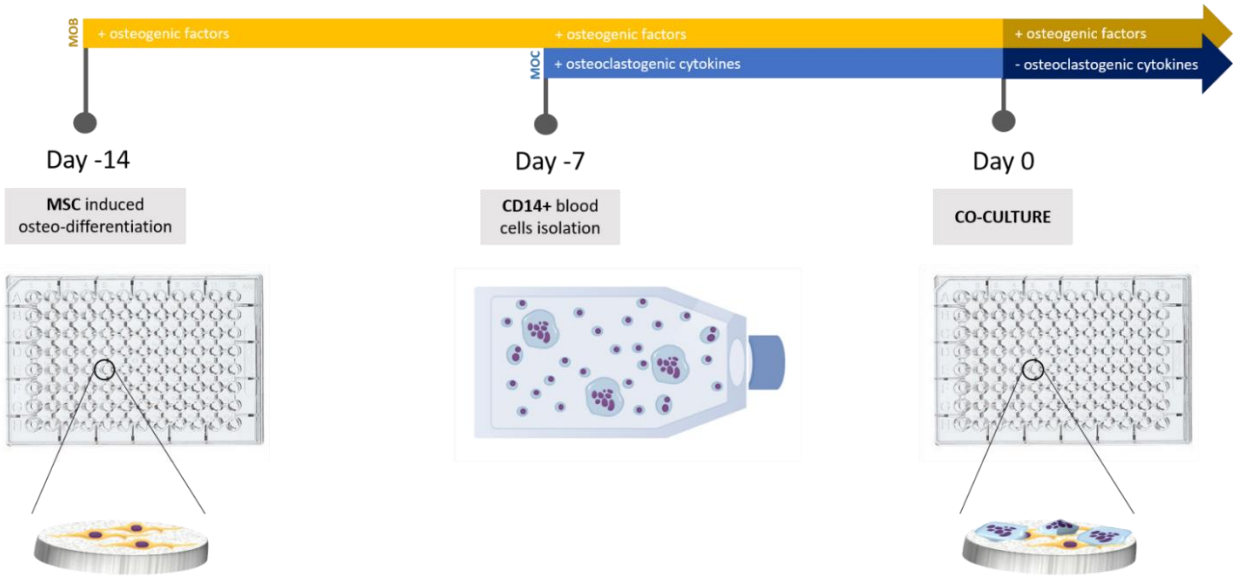

Figure II.4. Bone co-culture experimental scheme. hMSCs were seeded on top of dentine discs with osteoblastic medium in a 96-well plate. The medium was changed twice a week for 14 days. Simultaneously, 7 days before of the initialization of co-culture, the monocytes were isolated from the peripheral blood and stimulated with M-CSF and RANKL over 7 days. On day 0, the pre-osteoclasts were detached with accutase and seeded on top of differentiated hMSC.

Culture characterization The behaviour of both hMSC and osteoclast monoculture were compared with the co-culture. It was performed a phalloidin staining as described before, to assess the morphology and the cell dispersion of both cells. The osteoclast maturation was evaluated through a TRAP staining of dentine discs, as performed before.

2. Microfluidic systems

2.1. Preparation of the microfluidic devices

Microfluidic compartmentalization and design The microfluidic device for cell culture consisted of a poly(dimethlysiloxane) (PDMS) chamber placed against a glass coverslip. The microfluidic chamber was either commercially used (Milipore) or fabricated using soft lithography, as described by Park *et al* [104] (Figure II.2). Briefly, the first step was the fabrication of a master mold, which consists of two layers of photoresist structures on a flat silicon wafer substrate. Then, a PDMS mixture was placed over the master and incubated for 3 h at 50ºC. Afterwards, the cured PDMS cast was mechanically separated from the master mold and the compartments were punched out with a specific diameter using biopsy punch keys (Kai Medical). Three arrangements of compartmentalized microfluidic channels were accomplished and tested. The microfluidic chambers were sealed with super adhesive tape to remove any dust and were sterilized with several wash steps in 70% ethanol.

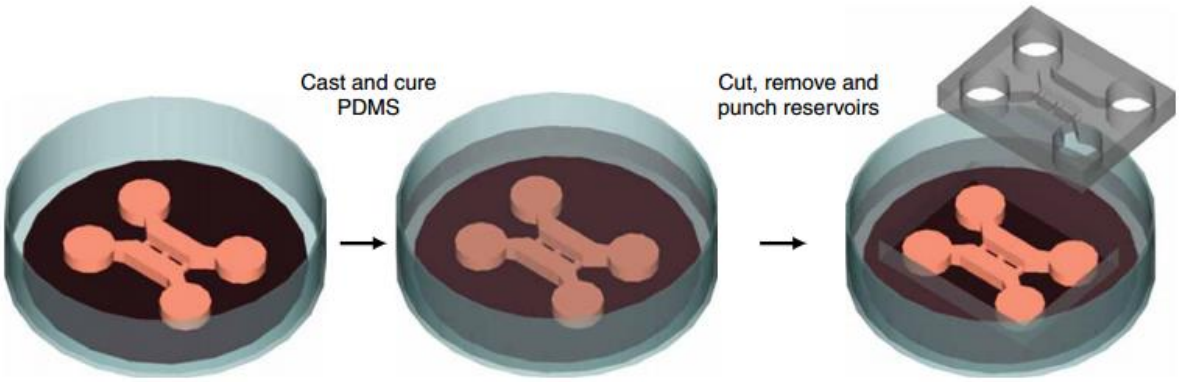

Figure II.5. Schematic process of microfluidic device fabrication by soft lithography. New microfluidic chambers were obtained by replica modelling PDMS against the master mold (adapted from [104]).

2.2 Microfluidic cultures

Microfluidic system assembly Sterile microfluidic chambers were assembled on top of poly-D-lysine (PDL) (Sigma-Aldrich) coated glass slides in 6-well plates. The glass slides were previously cleaned with nitric acid 65% for 24 h and sterilized by the exposition to UV radiation for 10 min. The slides were then incubated with 0.1 mg/ml of PDL solution, overnight at 37ºC and washed with clean water before the assembly. Complete medium was added to the reservoirs to ensure that the microgrooves connecting the compartments were totally filled and the system put into a vacuum system for 15 min.

Microfluidic tri-culture After ensuring a continuous flow over the channels, both cancer spheroids and bone co-culture system were transferred to each corresponding compartment. The microfluidics experiments were performed progressively through the combination of the cancer lines with each bone cell type independently until the final tri-culture system (Figure II.6). Experiments were also done in presence of only medium of each corresponding culture as controls. The morphology and behaviourally differences of the cultures were characterized following the methods above mentioned for each cell type.

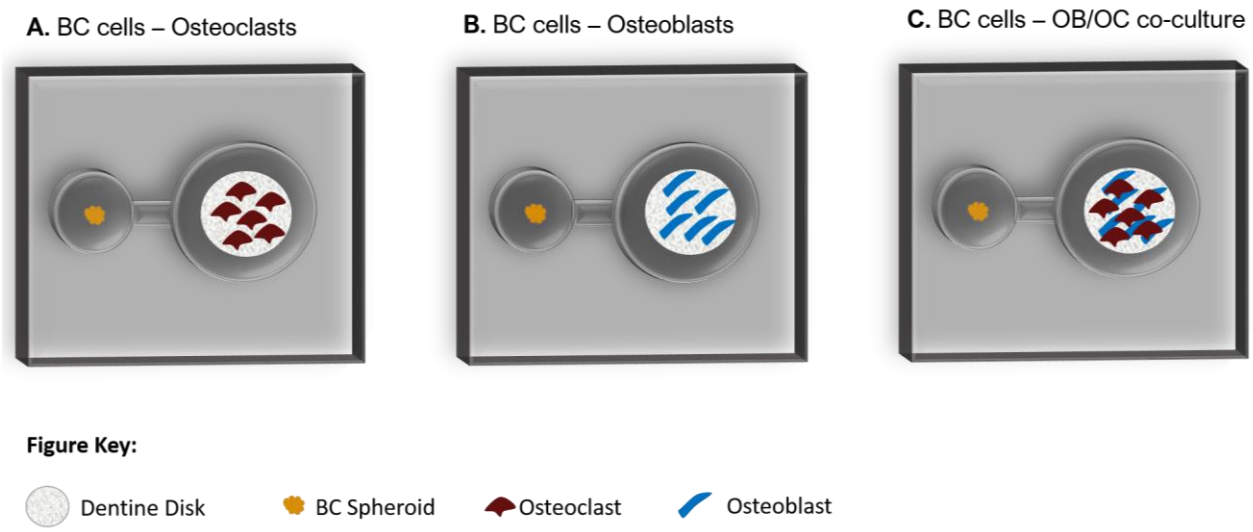

Figure II.6. Schematic overview of the microfluidic experiments with the combination of each cell type. Each experiment was performed individually.

3. Statistical analysis

Statistical significance was calcultated by the software GraphPad Prism version 6.01 (GraphPad Software, Inc.) using two-way analysis of variance (ANOVA) applying multiple comparisons test between all experimental groups. The data were expressed as mean values ± standard error of mean. p-Values less than 0.05 were defined as statistically significant. A significant difference between two experiment groups is denoted as *$p < 0.05$; **$p < 0.01$; ***$p < 0.001$; ****$p < 0.0001$.

Chapter III

Results and Discussion

---

1. Breast cancer spheroids

1.1. Formation of MCF-7 spheroids

1.2. MCF-7 spheroids characterization

1.3. Formation of MDA-MB-231 spheroids

1.4. MDA-MB-231 spheroids characterization

2. Bone Cells

2.1. Human Osteoblast Cultures

2.2. Human Osteoclast Cultures

2.3. Osteoblast/Osteoclast co-cultures

3. Microfluidic cultures

3.1. Preparation of microfluidic devices

3.2. Cell behaviour in microfluidic system

3.2.1. MCF-7 Spheroids

3.2.2. Bone system

Chapter III

Results and Discussion

1. Breast cancer spheroids

Analysis of both adjuvant and neoadjuvant trials has shown that breast cancer is not a single disease, but instead is a spectrum of tumour subtypes with distinct cellular origins, somatic changes and chemotherapy responsiveness [19]. Particularly, factors such as ER/PR hormone receptors and HER2 status are the main features upon which clinical decision-making has traditionally been based on, to guide patient treatment.

Therefore, an additional individualization of pre-clinical research between the breast cancer subtypes is imperative. With this in mind, a full characterization of two distinct breast cancer subtypes, MCF-7 and MDA-MB-231 was performed. While, MCF-7 is a double positive and endocrine responsive breast cancer cell line (classified as luminal A subtype), MDA-MB-231 is a triple negative and endocrine nonresponsive breast cancer cell line (classified as Claudin-low subtype).

1.1. Formation of MCF-7 spheroids

Increasingly, spheroids grown in 3D cell culture are being used in cancer research to more closely mimic the environment associated with tumours. Various spheroid formation techniques have been widely developed.

Herein, breast cancer cells were seeded in non-adherent surfaces and culture conditions were optimized in order to archive an efficient and reliable method to form spheroidal structures.

When cultured in standard TCPS conditions, MCF-7 cells grow as a homogeneous monolayer (Figure III.1A, first row). The presence of rBM in the media induces a natural aggregation of cells particularly notable on day 7 of culture. rBM is a solubilized basement membrane preparation extracted from the Engelbreth-Holm-Swarm (EHS) mouse sarcoma, a tumour rich in extracellular matrix proteins (mainly laminin, collagen IV, and entactin) and several growth factors that occur naturally in EHS tumour [105]. Therefore, the induction of self-aggregation could be likely explained either by the minor increase of medium viscosity, which difficult the cell movement, or due to the chemical interactions between the cell membrane receptors and the proteins of rBM which increase the stability of the structures formed [106]. However, these structures are not mature enough to mimic the complexity of *in vivo* tumours.

Spheroidal structures were obtained through a liquid-overlay culture on top of non-adhesive surfaces. Both poly-HEMA (Figure III.1A, middle row) and Agarose (Figure III.1A, last row) polymers were tested as non-adhesive coatings.

The low cell adhesiveness of poly-HEMA surfaces induce the MCF-7 to grow as aggregates since the beginning of the culture, and later on day 7 it is possible to observe the presence of small floating spheroids of about 200 µm diameter, both in presence and absence of rBM. Whilst, this method did not allow a control over the number and the size of the structures formed. It is important to have a minor size dispersion because different spheroid sizes imply a variation in diffusion gradients established for growth factors, nutrients or metabolites which will influence the response pattern in cell physiological and biochemical analyses [79].

Whereas, agarose coating surfaces induce a complete aggregation of MCF-7 cells in the middle of the well forming a single large spheroid. In particular, it is notable an outstanding circularity of spheroids in the presence of rBM with an aspect ratio reaching the perfect value of a sphere. At day 4 of culture, it is already possible to achieve structures of about 400 µm diameter. At day 7 of culture there are no significant differences between the size or the stability of the structures, although it is possible to see some dark zones in the central area which signpost an excessive condensation of cells within the structure, and consequently an extremely large necrotic core.

Extended studies revealed that tumour spheroids maintain many properties of their tumour counterparts which are lost in monolayer cultures: a higher degree of the structural, morphological and functional differentiation, similar growth kinetics and resembling resistance patterns to chemotherapeutics [79]. In particular, large spheroids are characterized by an external proliferating zone, an internal quiescent zone caused by the limited distribution of oxygen, nutrients and metabolites, and a necrotic core resembling the cellular heterogeneity of solid *in vivo* tumours [107].

Taking this into consideration, it was decided to select the condition of 10 000 cells cultured on top of agarose coating surfaces for 4 days in presence of rBM to go further with the studies of breast cancer MCF-7 spheroids in this project. This method allows a rapid and simple protocol for reproducible, large-scale spheroid production.

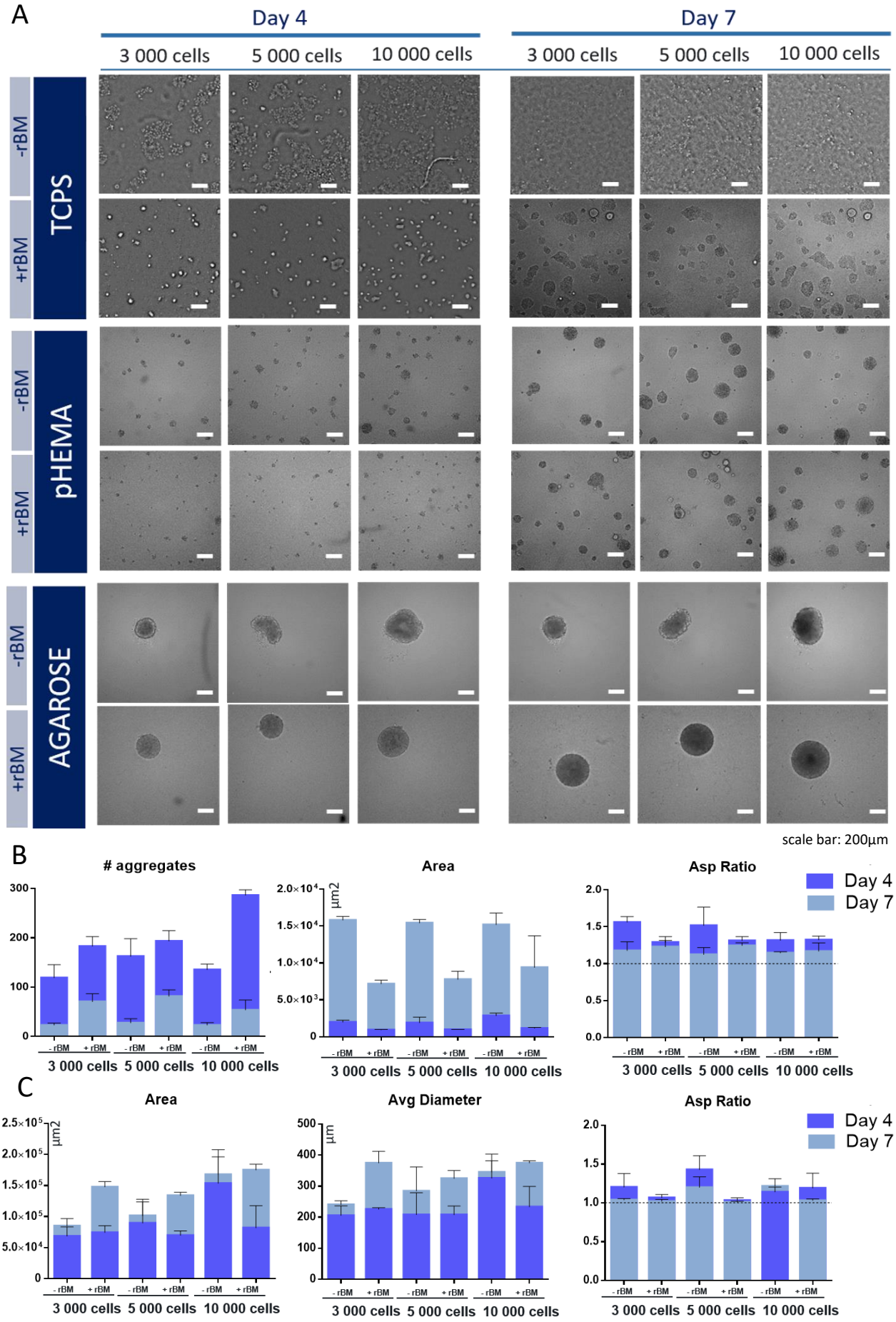

Figure III.1. Screening of optimized conditions for the MCF-7 spheroid formation. A) Representative images of each condition tested. B) pHEMA coating surfaces morphometric analysis. C) Agarose coating surfaces morphometric analysis. (n=4 spheroids per condition)

1.2. MCF-7 spheroids characterization

1.2.1. Morphology analysis

In order to test the feasibility of this technique, it was performed a shape descriptors high-throughput analysis on 50 spheroids using the selected condition: 10 000 cells seeded on agarose-coated surfaces, over 4 days of culture in presence of rBM.

By the frequency distribution graphs (Figure III.2) it is directly observed that all parameters followed a Gaussian distribution with a very slight divergence over the average value. This result is particular significant for the project progress due to the major importance of having replicated structures with the same characteristics which led to reduced variability on the experiment analysis itself.

Through this method were obtained spheroids with an average diameter of (432 ± 11,27) µm and an aspect ratio very close to the perfect sphere approximation (y=1).

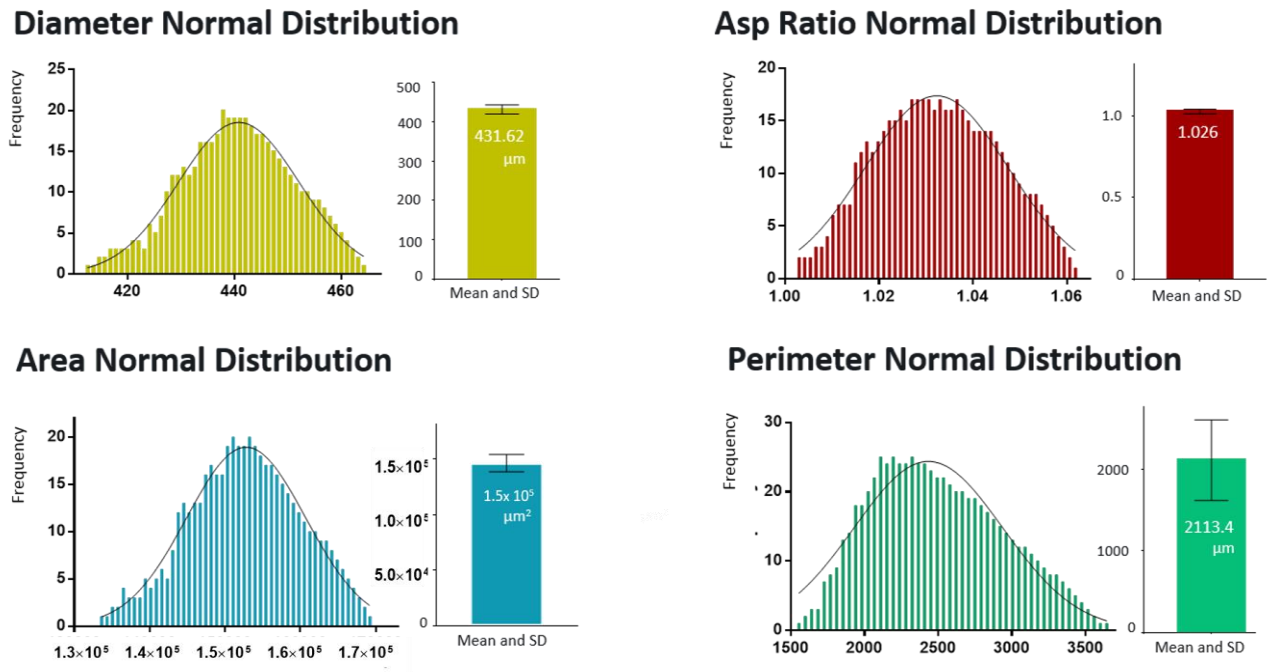

Figure III.2. Shape descriptors HTP analysis of MCF-7 spheroids. Frequency distribution plots of analysed shape descriptors and Gaussian best-fit line. Gaussian average values and SD error bars plotted on right (n=50 spheroids).

The 3D assembly of MCF-7 spheroids was assessed by an F-actin and nuclei staining of structures formed after 4 days in optimized culture conditions (Figure III.3A). The Z-projection of confocal microscopy stacked images corroborates the perfect spherical conformation of spheroid that was preliminarily concluded in the HTP analysis. Although, these images are obtained by the projection of several overstep slides of the outer layer of the spheroid and it is impossible to access the inner part of these structures.

It is postulated that this singularity may be either attributable to the incapacity of the reagent solutions to penetrate spheroid size during the staining protocol, or/and could be an effect of photon losses and spreading caused by refractive index mismatch within the depth samples that induced light distortions and scattering effects during the image acquisition caused by the excessive packing of cells within the structure [108].

To overcome this issue, cryostat sections of these structures were performed (Figure III.3B), where it was possible to validate about the full 3D assembly of these structures. Furthermore, in the middle sections it is possible to note an absence of phalloidin stain while the nuclei are still labelled. This result could indicate the presence of the necrotic core of spheroids reported in literature [107], where the cytoplasm of cells had collapsed but the nuclear fragments are still there. Even though, the presence of necrotic cells will be fully analysed through specific apoptotic studies, in the next section.

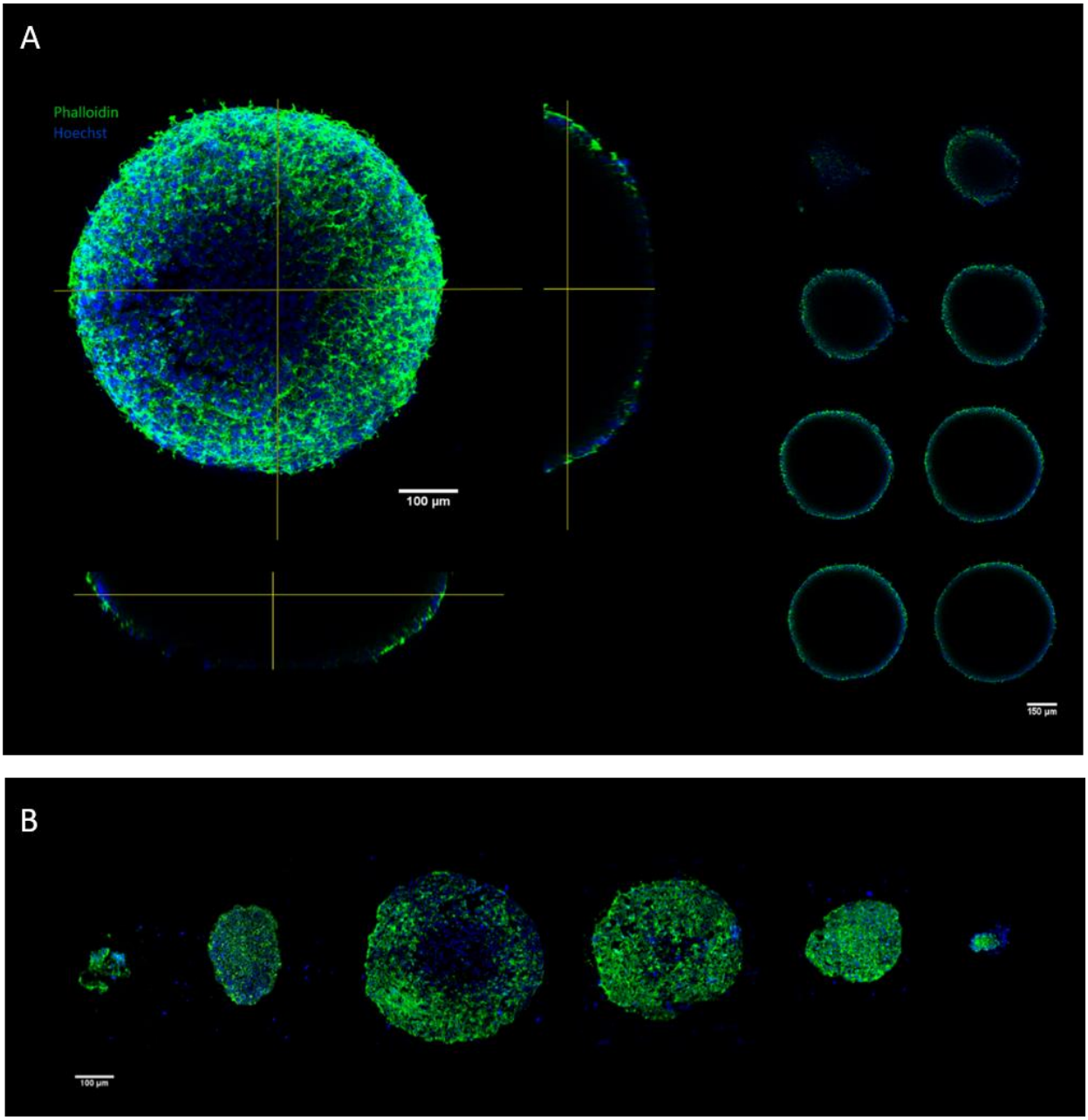

Figure III.3. Structural analysis of MCF-7 spheroids: Phalloidin 488 and Hoechst 33342 staining. A) 3D projection of consecutive confocal slides over the z-axis. The orthogonal views in x- and y-axis as well as the individual images of representative slides over the structure shown, reveal the incapacity to reach the inner layers of the structure. B) Sequential cryostat sections of an entire spheroid.

1.2.2. Apoptosis analysis

PI staining is a commonly used approach for studying apoptotic cells through differences in plasma membrane integrity and permeability. To investigate the accumulation and localization of dead cells in spheroids, it was performed a live/dead fluorescence assay using PI in combination with calcein AM dye (Figure III.4A).

It is possible to note that almost all the structure is viable except for some punctual cells, although not significant. Similarly to what happened before with the morphology staining, through this technique it is only possible to access the outer layers of the structure – consequently, it is not possible to take conclusions about the presence of a necrotic core.

The quantification of cellular viability was measured through the FACS analysis of dissociated spheroids labelled with PI and Annexin V (Figure III.4B). Analysing the cytometer diagrams, it is possible to conclude that about 70% of cells are double negative for both markers, and then are classified as viable cells. Whereas, about 30% of cells are PI positive and/or Annexin V positive, which are apoptotic/necrotic cells.

Despite it was not performed a specific experiment of cell apoptosis localization within the spheroid, putting all the results together, it is acceptable to conclude about the presence of a necrotic core.

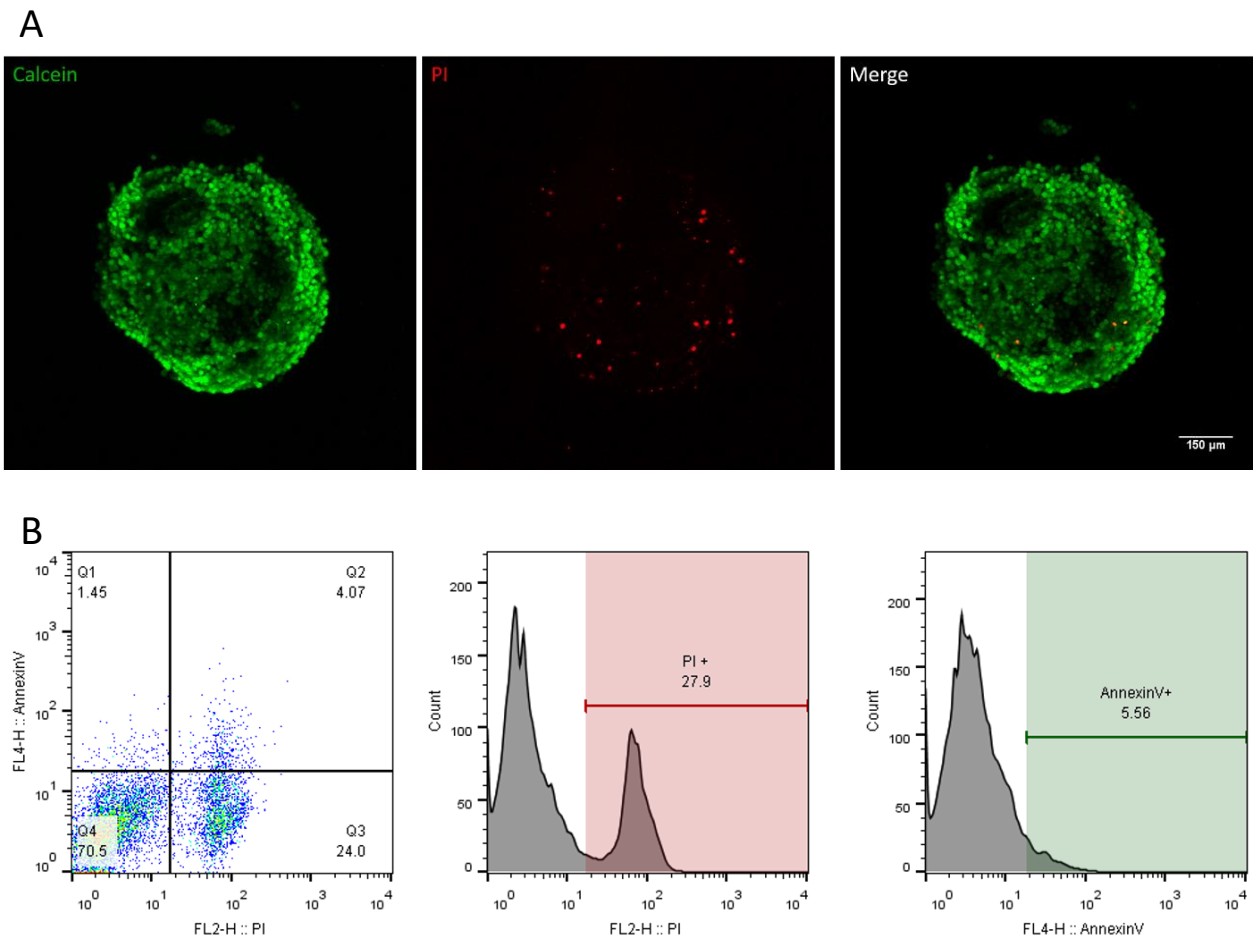

Figure III.4. Apoptosis analysis of MCF-7 spheroids. A) Live/dead staining with PI and Calcein AM dyes. B) FACS analysis of dissociated cells labelled with PI and Annexin V. PI is a late apoptosis marker, while Annexin V is an early apoptosis marker. Therefore, double negative cells are classified as viable; Annexin V positive are classified as early apoptotic cells and PI positive cells are classified as late apoptotic cells. It was expectable that the cells positive to PI expressed also the Annexin V marker, although the major population positive to PI does not express Annexin V. This could be explained by the advanced phase of apoptosis of these cells, where they already have a broken plasma membrane and therefore the Annexin V membrane marker could not able to bind.

1.2.3. Gene expression

Tumorigenesis is associated with gene expression changes on specific markers; therefore, gene expression profiling is a common aspect of breast cancer research and drug treatment practices.

In order to obtain a basal expression pattern of these cells, genes involved in metastatic vicious cycle and bone remodelling (VEGF, RANK and RANKL) were selected and design in NBCI/Primer-BLAST. Additionally, three reference genes, described as suitable housekeeping genes for breast cancer cells [109, 110], were tested: Beta-2-microglobulin (B2M), Histone H2A (HIST) and Tyrosine 3-monooxygenase (YWHAZ).

The primer efficiency was assessed for all genes and the graphs are shown in Table A.2 (Annexes).

Table III.1. Molecular information of genes used for MCF-7 characterization. (RG: Reference Gene)

Gene symbol	Gene name	Molecular function
B2M (RG)	β-2-microglobulin	Major histocompatibility complex
YWHAZ (RG)	Tyrosine 3-monooxygenase	Signal transduction
HIST (RG)	Histone cluster 1 (H2A)	Nucleosome structure
VEGF	Vascular endothelial growth factor	Vasculogenesis signal transduction
RANK	Receptor Activator of Nuclear Factor κB	Osteoclastogenesis transduction
RANKL	Receptor Activator of Nuclear Factor κB-Ligand	Osteoclastogenesis transduction

From the three reference genes tested (Figure III.5A), B2M was selected due to its early detection in quantitative RT-PCR running, i.e. low values of C_T, that allows to achieve a better differential gradient from the target genes values. B2M is also the reference gene with a smaller variance of C_T values between replicas.

VEGF overexpression is reported to be implicated with metastasis capacity in cancer cells [9]. Therefore, the expression profile of VEGF was used as a measure of cancer aggressiveness along the experiments with bone cells. Similarly, the expression pattern of both RANK and RANKL are particularly interesting when in metastasis bone environment. In basal conditions, the expression of these genes is predominantly weak (Figure III.5B), although these levels are expected to increase when in contact with bone cells, accordingly to the postulated metastatic vicious cycle [58].

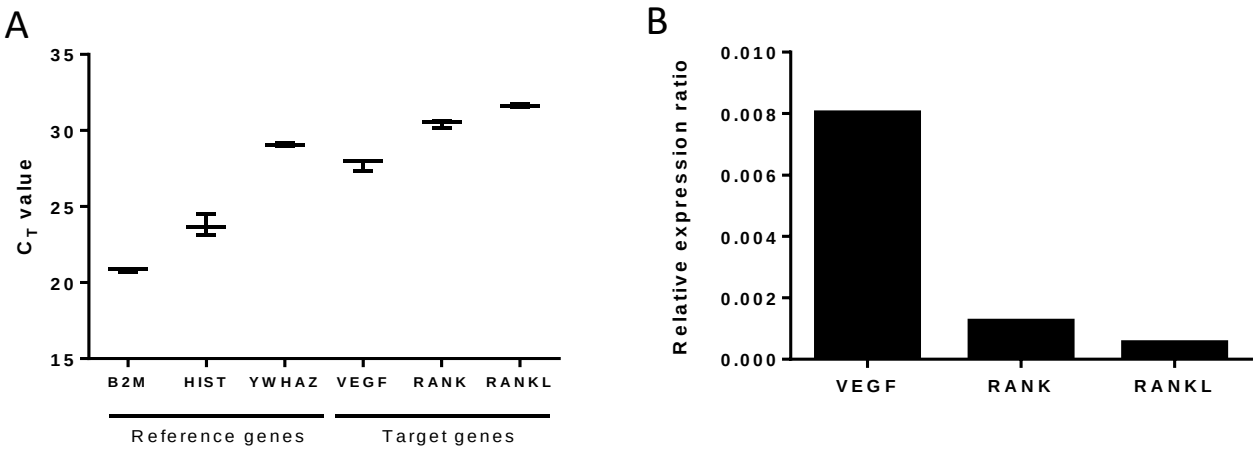

Figure III.5. MCF-7 gene expression analysis. A) C_T values dispersion of each gene analysed. The average values are represented as well as the min and max values obtained for each gene (n=3). B) Normalized gene expression pattern. The expression values of each gene were normalized with expression of B2M reference gene.

1.3. Formation of MDA-MB-231 spheroids

The culture optimization of MDA-MB-231 spheroids were reduced to the agarose non-adhesive surfaces due to the prior results for pHEMA studies in MCF-7 cells.

When cultured in standard TCPS conditions (Figure III.6A, first row), MDA-MB-231 cells exhibit a spread morphology and a vigorous growth speed denoted by the cell density difference between both time-points. The presence of rBM, once again, promote a slight aggregation of cells but not enough to achieve the 3D structure.

Cultured on top of pre-coated agarose surfaces (Figure III.6A, last row), MDA-MB-231 cells assemble themselves in a single aggregate in the middle of the well. Loss of E-cadherin expression was previously reported for MDA-MB-231 cell line [111], which turns this cells with low self-appetence to spontaneously form 3D spheroid structures. Although, it is reported that the presence of rBM mediates the interaction of integrin β1 and ECM proteins which establish the structure and allow the formation of large 3D spheroidal structures [112].

At day 4 of culture, in presence of rBM it is already possible to achieve structures of about 500 µm diameter with an aspect ratio value near the perfect spherical value. At day 7 of culture, small structures were observed in the absence of rBM and, in opposition, an outstanding excessive growth was detected in presence of rBM.

From these results, it was selected the condition of 5 000 cells cultured on top of agarose coating surfaces for 4 days in presence of rBM to go further with the studies of breast cancer MDA-MB-231 spheroids in this project.

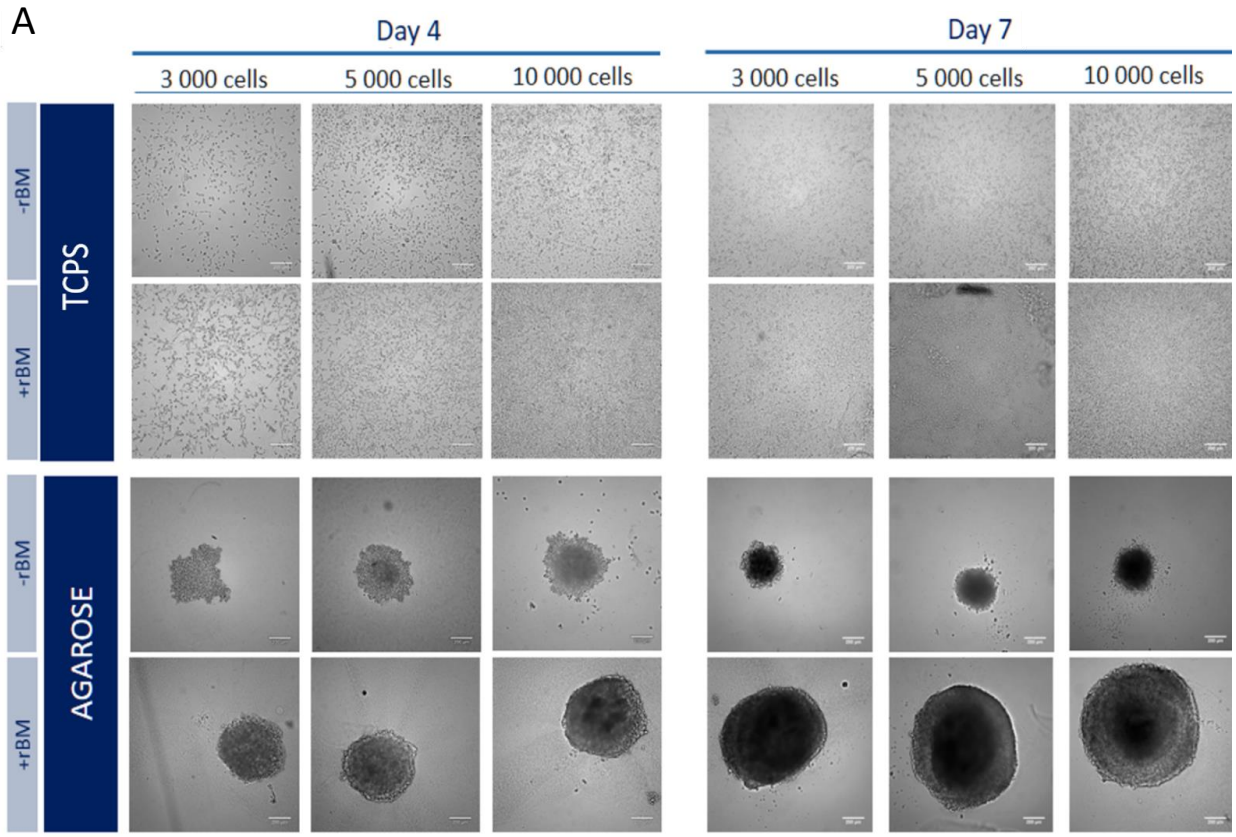

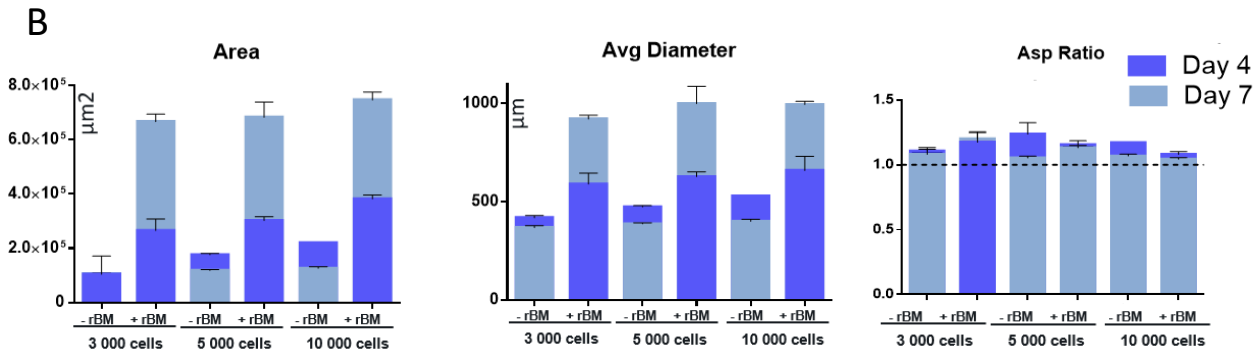

Figure III.6. Screening of optimized conditions for the MDA-MB-231 spheroid formation. A) Representative images of each condition tested B) Agarose coating surfaces results analysis (n=6 spheroids per condition)

1.4. MDA-MB-231 spheroids characterization

1.4.1. Morphology analysis

From the HTP analysis of shape descriptors in 50 MDA-MB-231 spheroids, it is concluded, as expected, a large variability of the results due to the non-innate capacity of these cells to form these aggregate structures. Nonetheless, it is possible, to distinguish a major population of cells with the normal Gaussian distribution around the average value, (369,2 ± 38,97) µm, that were picked out to the further characterization studies.

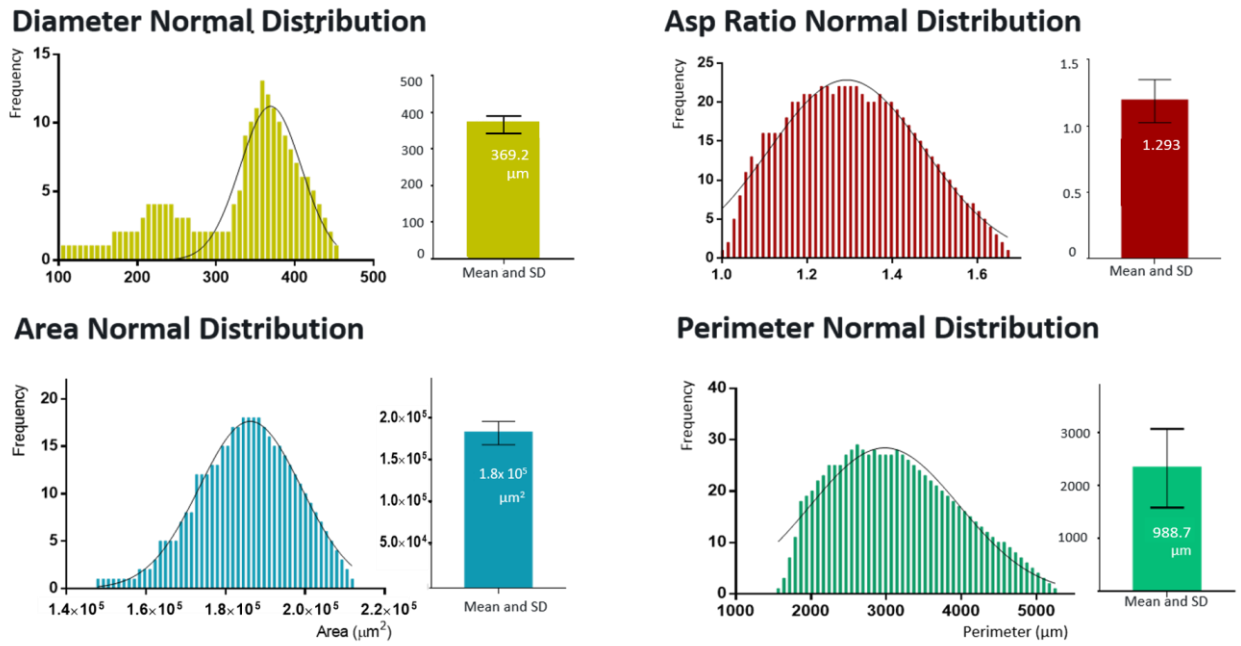

Figure III.7. Shape descriptors HTP analysis of MDA-MD-231 spheroids. Frequency distribution plots of shape descriptors and Gaussian best-fit line. Gaussian average values and SD error bars plotted on right (n=50 spheroids).

The 3D conformation of MDA-MB-231 spheroids was analysed by an F-actin and nuclei staining of structures formed after 4 days in optimized culture conditions (Figure III.8A).

Despite it was not obtained a perfect circular conformation, it is verified the 3D conformation of structure along the z-axis. The dispersion around the circularity could be an effect of post-manipulation during the staining protocol, since that these structures are not so densely compacted and therefore are more susceptible to lose their original conformation.

The cryostat sections of these structures (Figure III.8B) allow to confirm the 3D assembly of the entire structure and evidence the homogeneous spread of cells, i.e. the cells are not so compressed within the structure and there is still more free space to cell growth and compactness.

Interestingly, it is not possible yet to infer about the existence of a necrotic core, since all the structure is equally stained with both phalloidin and Hoechst dyes.

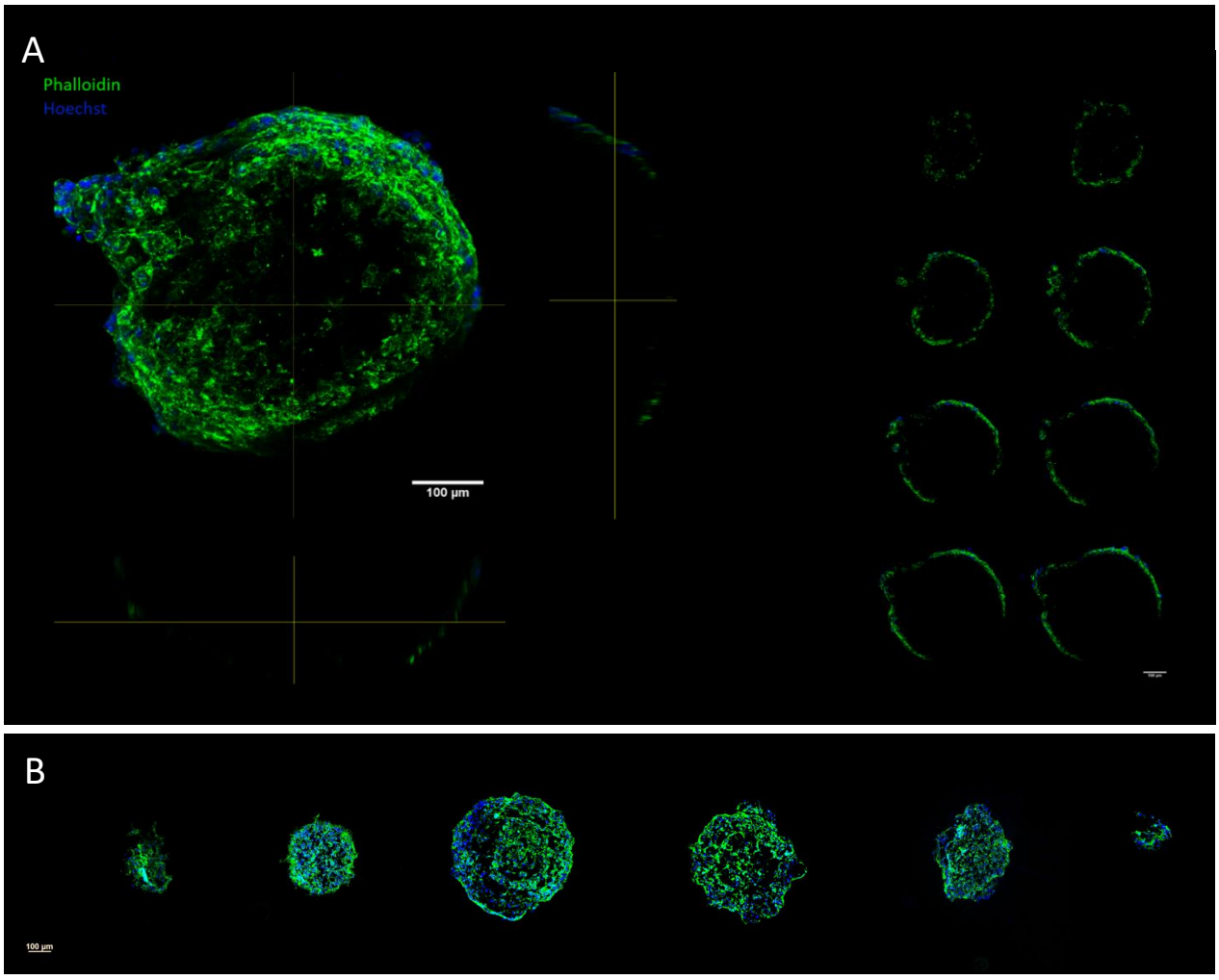

Figure III.8. Structural analysis of MDA-MB-231 spheroids: Phalloidin 488 and Hoechst 33342 staining. A) 3D projection of consecutive confocal slides over the z-axis. The orthogonal views in x- and y-axis as well as the individual images of representative slides over the structure shown, reveal the incapacity to reach the inner layers of the structure. B) Sequential cryostat sections of an entire spheroid.

1.4.2. Apoptosis analysis

The live/dead assay using PI and calcein AM dyes (Figure III.9A) reveal a broad viable spheroid stained with calcein with some unspecific cells labelled with PI. The unspecific label could be a result of a partial 3D conformation loss caused by the manipulation of spheroid during the assay.

FACS analysis of dissociated spheroids labelled with PI and Annexin V (Figure III.9B) show the presence of 75% of cells negative for both markers, i.e. fully viable. While about 20% are positive cells for Annexin V marker, which means that they are in an early apoptosis process. The remarkably reduced presence of PI-positive cells indicates the absence of the expected necrotic core. Despite of the large size of these structures, the small compactness of cells within the structures due to the morphological features of this cell type, allow for a better diffusion of oxygen, nutrients and metabolites through the spheroid depth.

This result could rise some questions about the cell density chosen previously. It should be performed an alternative characterization of MDA-MB-231 spheroids with an initial cell density of 10 000 cells/well and then go further with the studies of these breast cancer spheroids in the scope of this project.

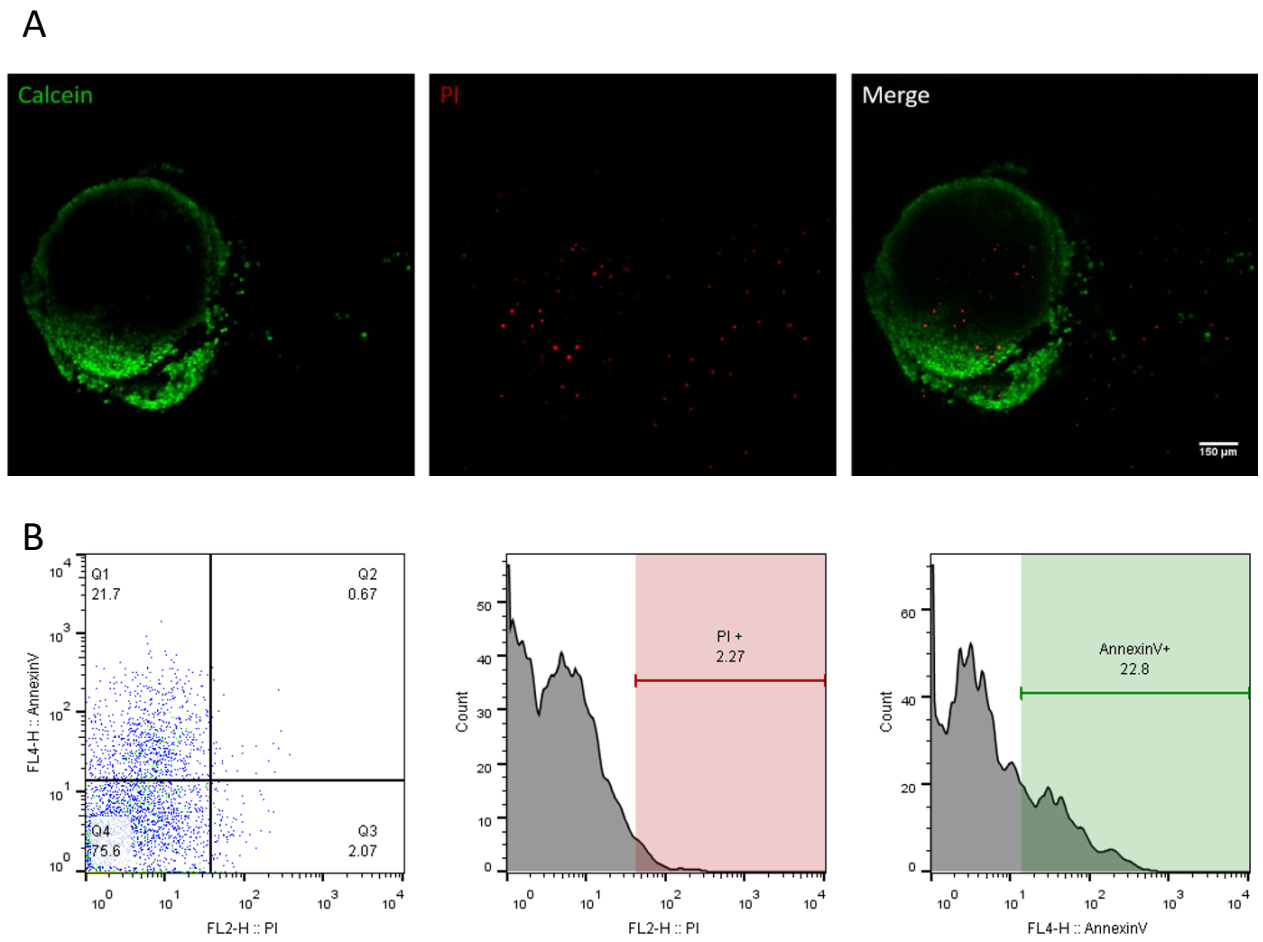

Figure III.9. Apoptosis analysis of MDA-MB-231 spheroids. A) Live/dead staining with PI and Calcein AM dyes. B) FACS analysis of dissociated cells labelled with PI and Annexin V.

2. Bone cells

The characterization of bone cells, osteoblasts and osteoclasts, is essential for an understanding of bone pathophysiology, particularly in case of bone metastasis.

2.1. Human Osteoblast Cultures

Several methods have been described to isolate and culture osteoblasts [113]. Frequently, human osteoblasts are obtained from *in vitro* differentiation of bone marrow isolated cells.

MSCs are pluripotent cells that have the potential to differentiate into chondrogenic, adipogenic and osteoblastic lineage – whereby, the differentiation of MSCs *in vitro* is sensible and largely depends on the culture conditions. The osteogenic differentiation of MSCs *in vitro* has been reported to be induced by the presence of growth stimulating factors such as, dexamethasone, Vitamin D3, ascorbic acid and β-glycerophosphate [114].

Although, there are still a large variability of protocols in the literature concerning the exact combination of inducer factors to achieve a quick and effective osteoblastic phenotype of MSCs in culture. Therefore, 4 combinations of differentiation factors at different concentration were designed and tested (Table III.2), in order to obtain the most suitable osteogenic medium.

Table III.2. Chemical composition of osteogenic supplemented media combinations.

	DIFF #1	DIFF #2	DIFF #3	DIFF #4
1a,25-Dihydroxyvitamin D3	10^{-7} M	10^{-7} M	10^{-7} M	-
Dexamethasone	10^{-8} M	10^{-7} M	10^{-7} M	10^{-7} M
β-glycerol phosphate	-	-	$5x10^{-5}$ M	$5x10^{-5}$ M
2-phosph-L-Ascorbic Acid	-	-	10^{-2} M	10^{-2} M

Having the bone co-culture system in mind, every condition was performed either with supplemented osteoblastic medium (DMEM, 10% Gibco inactivated FBS) and osteoclastic medium (α-MEM, 10% Hyclone inactivated FBS).

2.1.1. Morphological analysis

The cellular morphology was monitored over the differentiation process at different time-points. At day 4 of induced differentiation (Figure III.10A), MSCs exhibit a homogeneous confluent distribution with a characteristic fibroblastic phenotype, although with no significant differences over the differentiation conditions.

At day 7 of differentiation (Figure III.10B), there are still no significant differences between the conditions, however cells appear to be organized through a defined direction within the well. This orientation is provided by the stereochemical orientation of negatively charged groups of type I collagen fibrils produced by immature pre-osteoblastic cells in the first steps of differentiation process – these fibrils are believed to act as mineralized crystal nucleation points later in the process [115].

Moreover, at day 14 of differentiation (Figure III.10C) there is a clear outstanding phenotype change, particularly on conditions #3 and #4 on both osteoblastic and osteoclastic media. It is possible to note the presence of several mineralization vesicles described in the literature as the mean through these cells release calcium phosphate deposits to the extracellular matrix to form new-born mineralized matrix [116].

These results, although preliminary, indicate an effective induction of osteodifferentiation particularly for both condition #3 and #4.

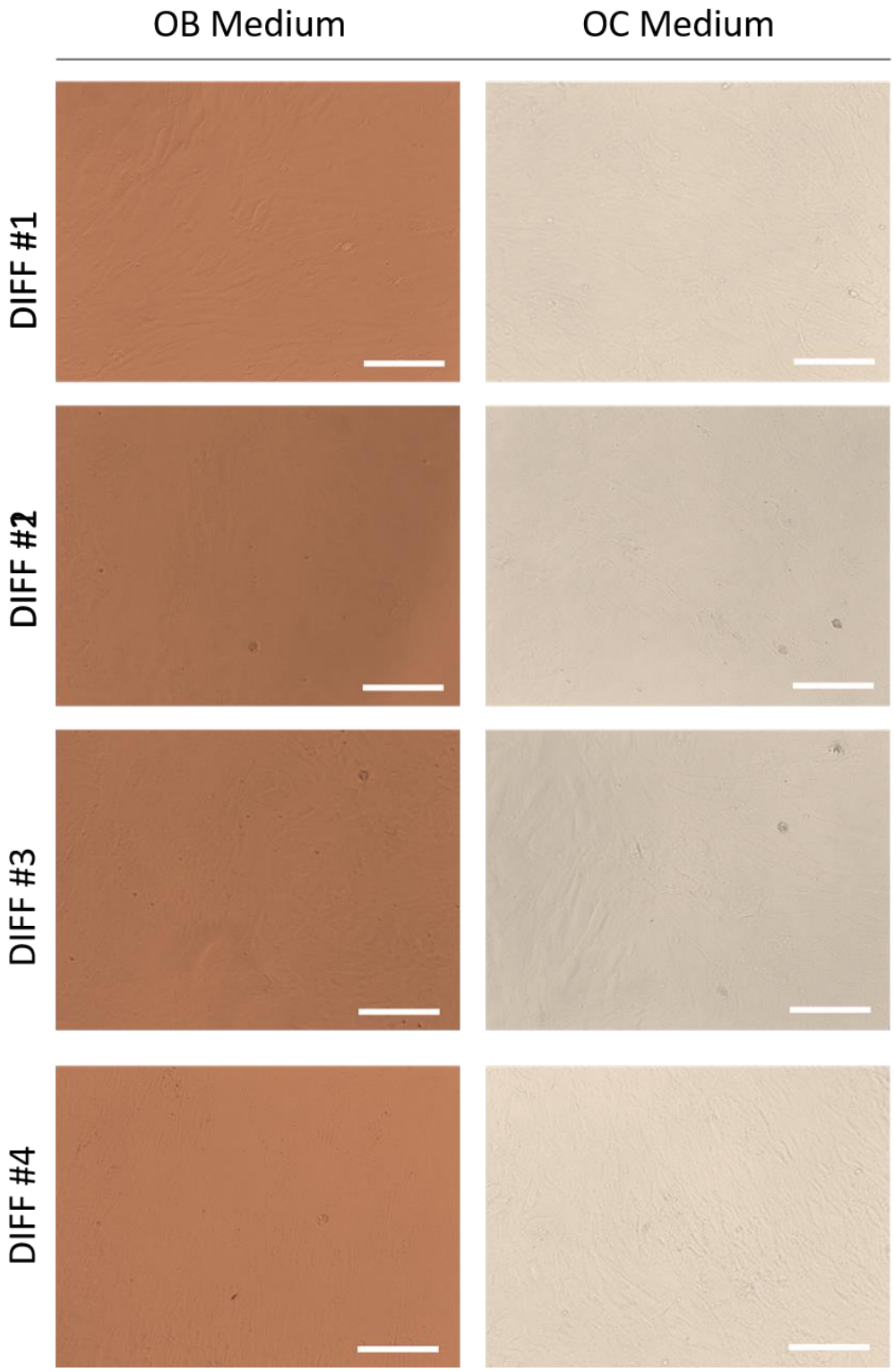

Figure III.10A. Morphological phenotype of MSC on induced differentiation for 4 days. Scale bar: 200µm

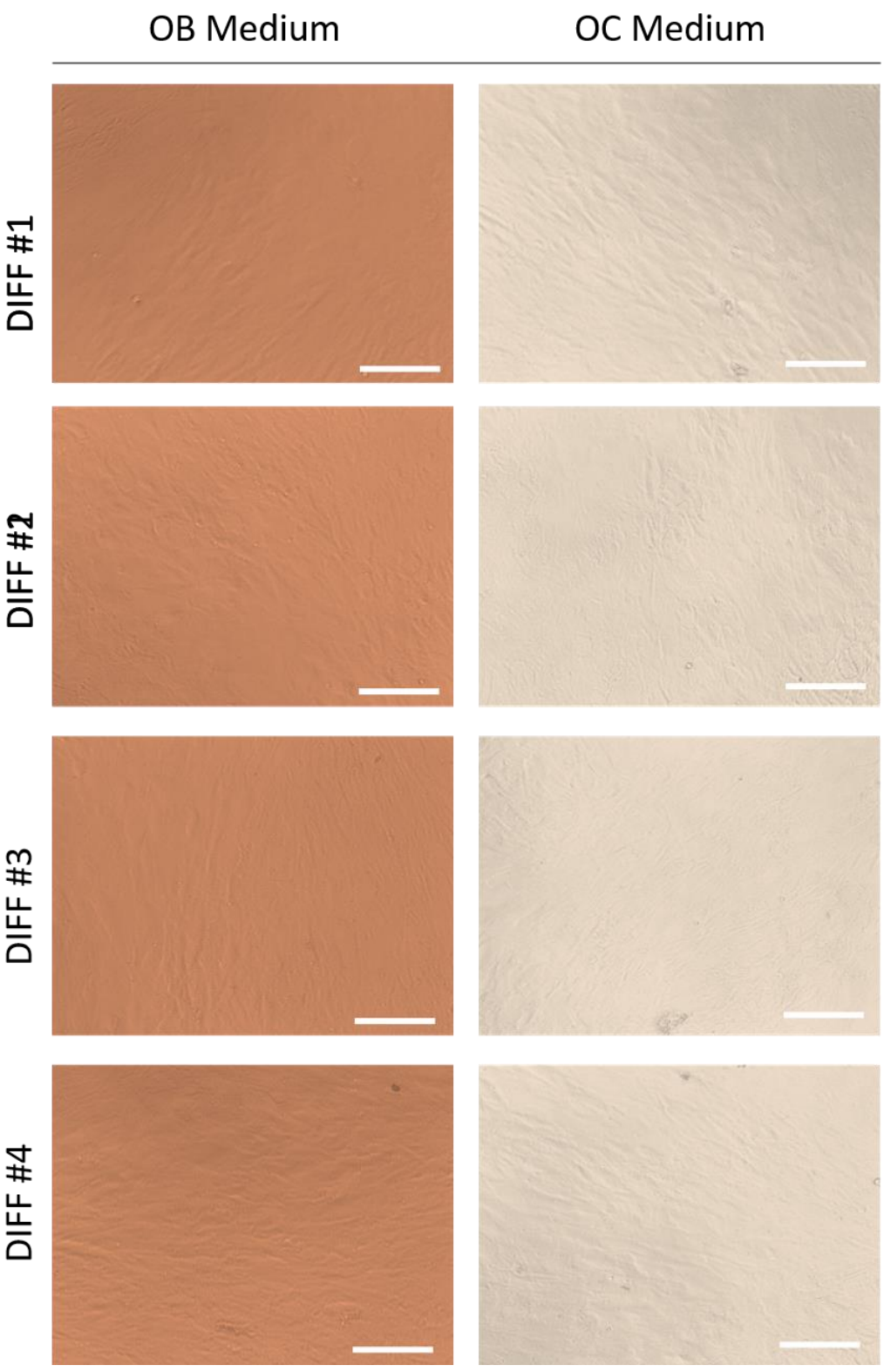

Figure III.10B. Morphological phenotype of MSC on induced differentiation for 7 days. Scale bar: 200µm

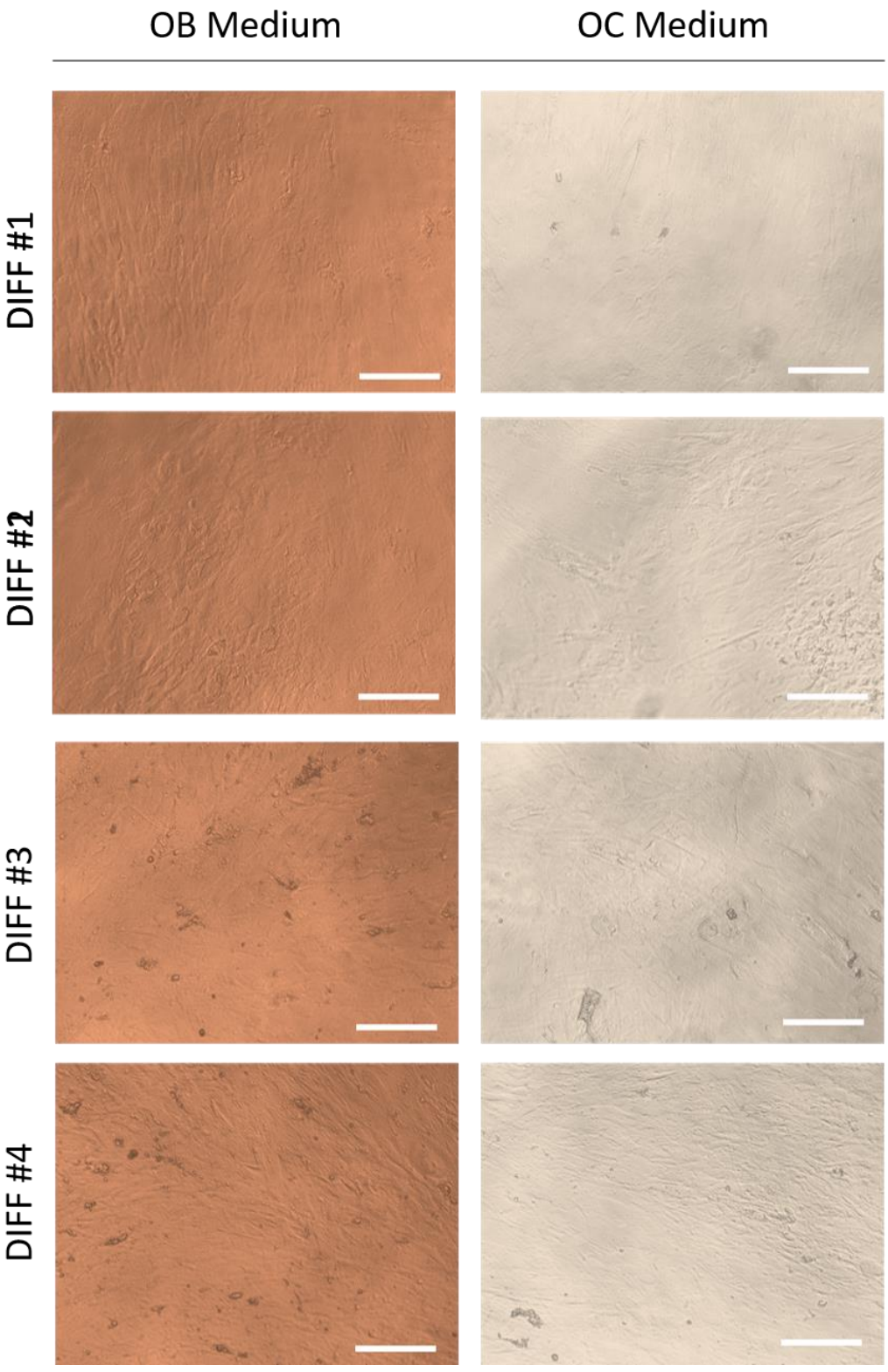

Figure III.10C. Morphological phenotype of MSC on induced differentiation for 14 days. Scale bar: 200µm

2.1.2. Cellular viability

Cell proliferation throughout osteoblast differentiation was indirectly inferred from the dsDNA content for each experimental condition (Figure III.11), while cell metabolic activity was evaluated by the ability of cells to reduce resazurin (Figure III.12).

For the osteogenic combinations #3 and #4 in osteoblastic medium, it is particularly denoted the three described stages of differentiation: proliferation, matrix production/maturation, and mineralization [117].

Initially, after 1 day of differentiation, it is noted an increased in DNA content on these two combinations when compared with the remaining samples. This preliminary result could be explained by the vigorous cell proliferation described for the first phase of osteoblastic differentiation.

For day 7 of differentiation, despite of the low values of DNA for all samples (likely due to a mistaken dilution step during the procedure) it is possible to conclude about the increased metabolic activity of conditions #3 and #4 which is presumably an indication of intense matrix metabolites production that characterize the second phase of osteoblastic differentiation.

After 14 days of differentiation, both DNA content and cell metabolic activity are significantly decreased for conditions #3 and #4 making evidence to the fact that these cells are already in the mineralization phase. In the meantime, at this point the combination #1 and #2 seems to be initiating their differentiation process.

The results for combinations tested in osteoclastic medium exhibit a generalized low quantity of DNA with exceeded high levels of metabolic activity along the experiment course. These arbitrary results could indicate that cells are stressed in these conditions, which do not allow them to fully differentiate into osteoblasts.

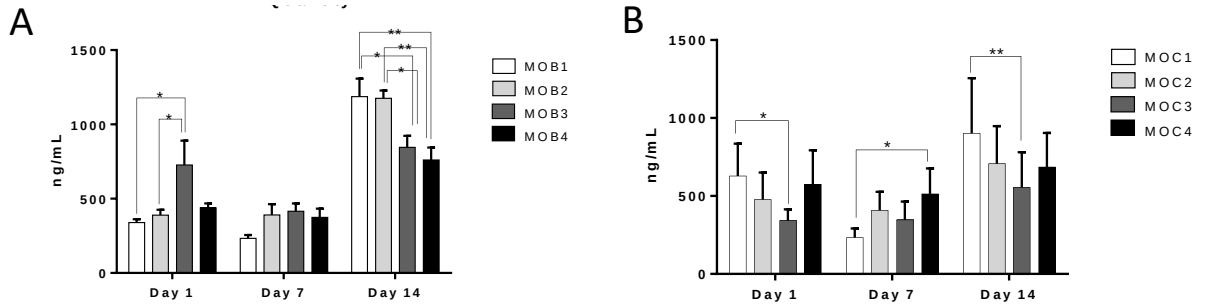

Figure III.11. dsDNA quantification by means of PicoGreen fluorescence emission. The results for osteogenic conditions tested in osteoblast medium (MOB) and osteoclastic medium (MOC) are represented in (A) and (B), respectively (n=6 replicas, * p<0.05, ** p<0.01, *** p<0.001, **** p<0.0001).

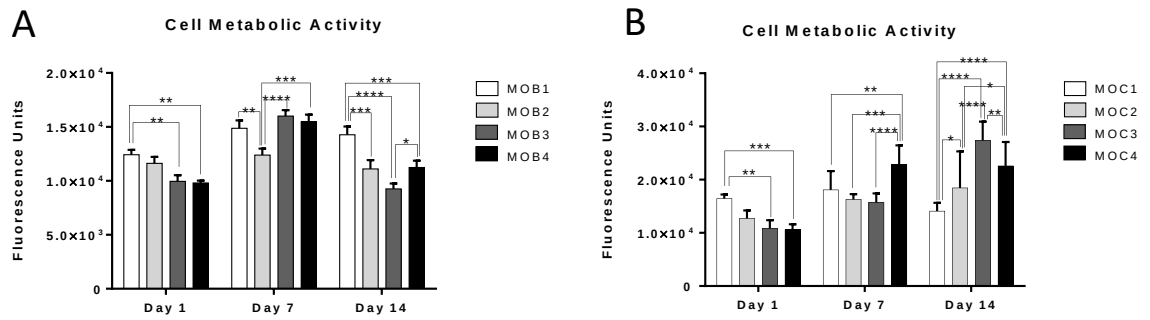

Figure III.12. Cell metabolic activity measured by fluorescence emission of resazurin reduction products. The results for osteogenic conditions tested in osteoblast medium (MOB) and osteoclastic medium (MOC) are represented in (A) and (B), respectively (n=6 replicas, * p<0.05, ** p<0.01, *** p<0.001, **** p<0.0001).

2.1.3. ALP activity and quantification

ALP quantification was performed in order to detect early mineralization stages. ALP is a membrane enzyme expressed in osteoblasts that is capable of generating phosphate by incorporation of hydroxylapatite, the inorganic component of bone, in first stages of bone mineralization.

ALP expression was assessed either through direct staining of the wells (Figure III.13A) and ALP activity quantification measured from sample lysates (Figure III.13B).

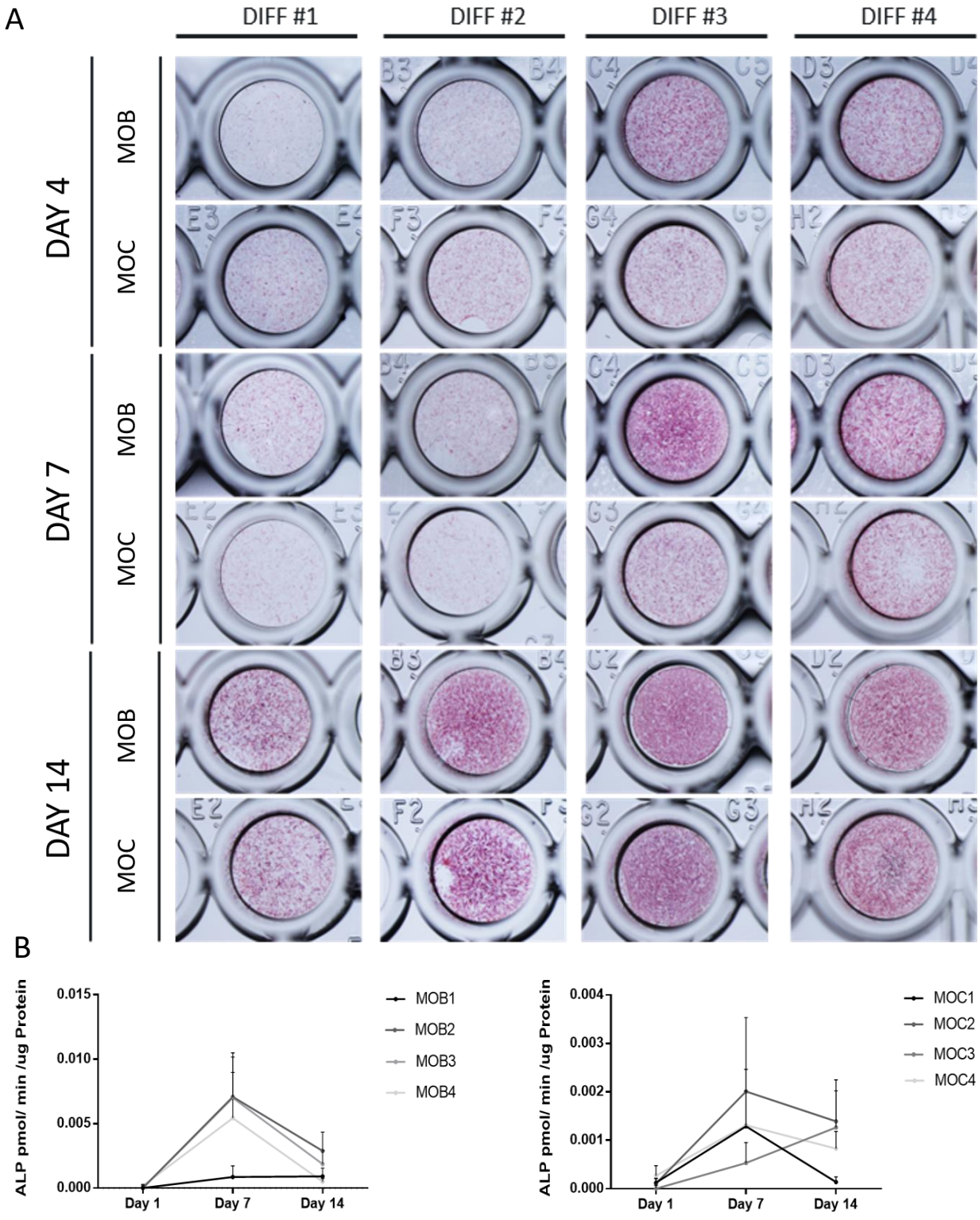

Figure III.13. ALP expression. A) ALP staining. B) ALP activity normalized to the total protein content.

At day 4 of differentiation it is already possible to observe a slight positive stain in both #3 and #4 conditions in osteoblastic medium that stand out from the remaining conditions. At day 7, the same pattern remains with an increased effect, where the #3 condition appears to be the osteogenic condition that most induce the early mineralization of MSCs. At day 14 of differentiation, there is already a generalized positive stain for all conditions. At this point, it is postulated that the early steps of mineralization have already started in every condition, which indicates a delayed induction of osteogenic differentiation for all conditions.

Accordingly, ALP quantification graphs validate previous results with a protuberant high activity of ALP at day 7 of differentiation for both #3 and #4 conditions in osteoblastic medium. At day 14 there is a generalized decrease of ALP activity indicating the advanced phase of differentiation process of these cells.

For conditions in osteoclastic medium, the ALP quantification is globally very low indicating the absence of ALP expression. The lack of essential amino acids and the different composition between serum of both media seems to affect negatively the differentiation process of MSCs, therefore for co-culture system the osteoclastic medium is not ideal.

2.1.4. Alizarin-red assay

Calcium deposition in osteoblastic new formed matrix was quantified by alizarin red staining, at day 14 of the differentiation (Figure III.14).

Similarly to the previous differentiation studies, the results show a positive staining for combination #3 and #4 in both osteoblastic and osteogenic medium. Although, for combination #3 in osteoblastic medium there is a clear strong positive staining that stands out from the remaining combinations. Alizarin quantification results, corroborate the previous conclusions with a significant increase for condition #3 in osteoblastic medium.

It was also performed a Von Kossa staining, although on day 14 of culture it was not obtained any positive result for matrix mineralization (data not shown). Von Kossa staining is expected to be a better suitable assay for long-term differentiation experiments.

Taken together these results, it was selected the #3 combination in osteoblastic medium to proceed with the co-culture system.

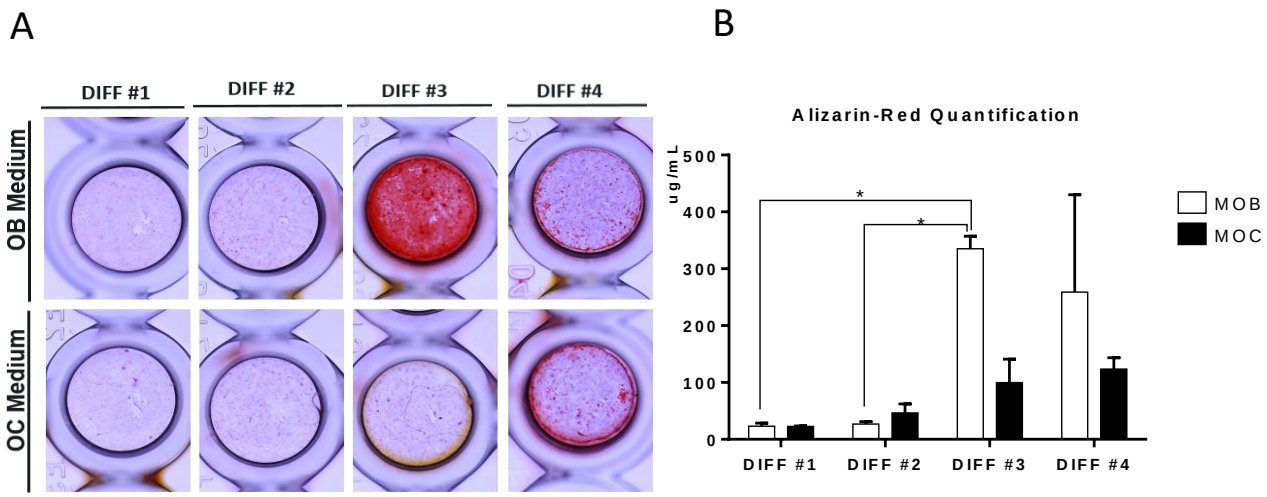

Figure III.14. Alizarin-red mineralization assay. A) Extracellular calcium deposits were visualised through Alizarin-red staining of each differentiation condition. B) Alizarin-red quantification (n=3 replicas, * p <0.05).

2.1.5. Gene expression

The gene markers expression analysis was performed in osteoblastic cultures supplemented with osteogenic combination #3 in DMEM medium during 14 days (Figure III.15A).

As osteoblasts proliferate and differentiate from MSCs they express/produce several proteins including growth factors, transcription factors and ECM proteins, each comprising a well characterized temporal pattern of expression.

In the early steps of differentiation, the expression of transcription factors such as Runx2 and Osx in osteochondroprogenitors is reported to initiate the osteo-lineage commitment. Further on, during the matrix production phase, it is reported the expression of genes associated with the formation of bone matrix such as type I collagen, which will be mineralized with apatite crystals upon activation of tissue-non-specific alkaline phosphatase (ALP). Ultimately, in the final stage of matrix maturation, genes associated with mineralization, such as osteocalcin (OCN) and bone sialoprotein (IBSP), are expressed at the highest levels [117].

As expected for day 14 of differentiation, the results show an outstanding high expression of type I collagen (Col1a), indicating the massive production of new ECM characteristic of differentiated osteoblasts. As verified by both ALP protein qualitative and quantitative experiments, the positive expression of ALP transcripts also corroborates the on-going first steps of ECM mineralization.

Osteocalcin (OCN), is a secreted tissue-specific protein, that act as a circulating hormone involved in the control of insulin secretion and sensitivity. The positive expression of OCN transcripts indicates an advanced maturation of osteoblasts in culture. Furthermore, OCN, as an endocrine factor, has an extremely significant role in the stimulation of metastatic breast cancer cells within the environment, contributing for the progressive aggressiveness of metastatic vicious cycle.

It is also reported that osteoblasts release VEGF in response to a number of stimuli and express receptors for VEGF in a differentiation dependent manner, modulated by the extracellular microenvironment [118]. Despite the low basal expression, the analysis of VEGF gene profile in microfluidic experiments will reflect the effect of cancer cells in osteoblasts.

Concerning the development of a full independent bone co-culture system, the expression of RANKL transcripts was evaluated over the course of differentiation process (Figure III.15B). RANKL has a pivotal role in bone remodelling and is the main inductor of osteoclastogenesis on mononuclear osteoclast progenitors [41]. The positive expression of RANKL on time of co-culture initiation (day 14 of MSCs differentiation) validates the experiment design and allows moving forward on the project development.

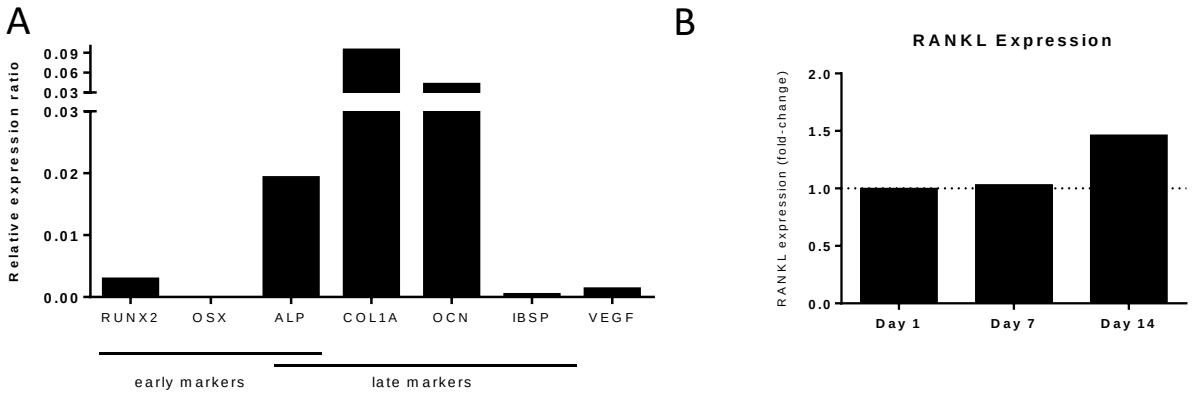

Figure III.15. Osteoblastic gene expression analysis. A) Osteoblastic gene markers analysis. The expression values of each gene were normalized with expression of B2M gene. B) RANKL chronological expression analysis. The expression values were normalized with by the basal expression of RANKL on day 1 of differentiation.

2.2. Human Osteoclast Cultures

2.2.1. Isolation and maturation procedure

Osteoclasts are large, multinucleated cells formed by the fusion of osteoclast precursors found in the monocyte fraction of blood.

To generate human osteoclasts, PBMCs were first isolated by density centrifugation from whole blood. In order to positively enrich the PBMC population with osteoclast precursors, the cell suspension was further purified by isolating CD14+ cells through magnetic sorting (Figure III.16).

CD14 is a cell surface receptor highly expressed in monocytes involved in innate immune system. CD14+ monocytes can differentiate into a multitude of different cells, including dendritic cells, tissue-macrophages and osteoclasts, through differentiation pathway encouraged by specific cytokines.

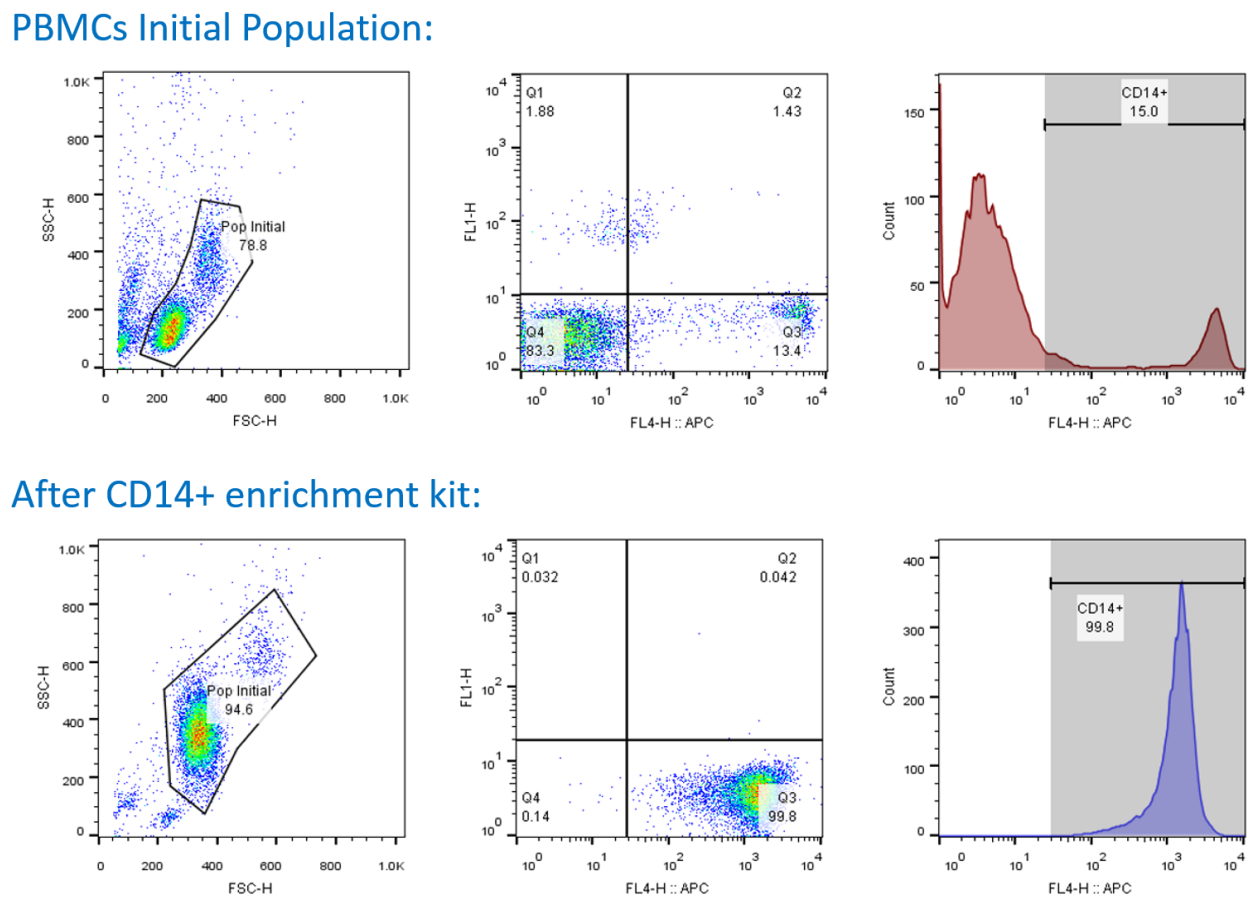

Figure III.16. FACS analysis of CD14+ cells content in initial PBMC population and after magnetic enrichment. Notably, the enrichment step allows a shift from 15% of total initial population to almost a 100% on final population of CD14+ cells (n=3). The antibody quality was validated through the analysis of APC isotype on both cell samples (data not shown).

The formation of resorbing osteoclasts is a complex multi-step process involving the commitment of cells from the monocyte lineage to differentiate into osteoclast precursors, the fusion of these cells to form mature multi-nuclear osteoclasts, and finally the activation of the osteoclasts to resorb bone. The cytokines M-CSF and RANKL are both essential and sufficient for survival, proliferation and differentiation of osteoclasts [113].

M-CSF induces the proliferation and survival of cells from monocyte/macrophage lineage; while, the interaction between RANK and RANKL, trigger the transduction pathway on M-CSF-induced cells that induces the fusion of mononuclear osteoclast progenitors [113].

The gradual evolution of CD14+ monocytes morphology along with the cytokine osteoclast-induction period is represented in Figure III.17.

Some punctual multinucleated cells of about 100-200 µm length are clearly observed on day 9 of differentiation, indicating the propensity for these cells to generate fully active osteoclast. At this time-point, osteoclasts culture is considered to be prepared for the functional resorption studies [119].

An exceeded cytokine osteoclast-induction period is not desirable because once an osteoclast initiates their functional activity, its lifespan is very limited and it will not survive to the passage for other substrates. Therefore, day 9 was selected as the end-point of osteoclast-induction cytokine stimulation for being considered the time-point with the ideal amount of pre-osteoclast cells with differentiation propensity.

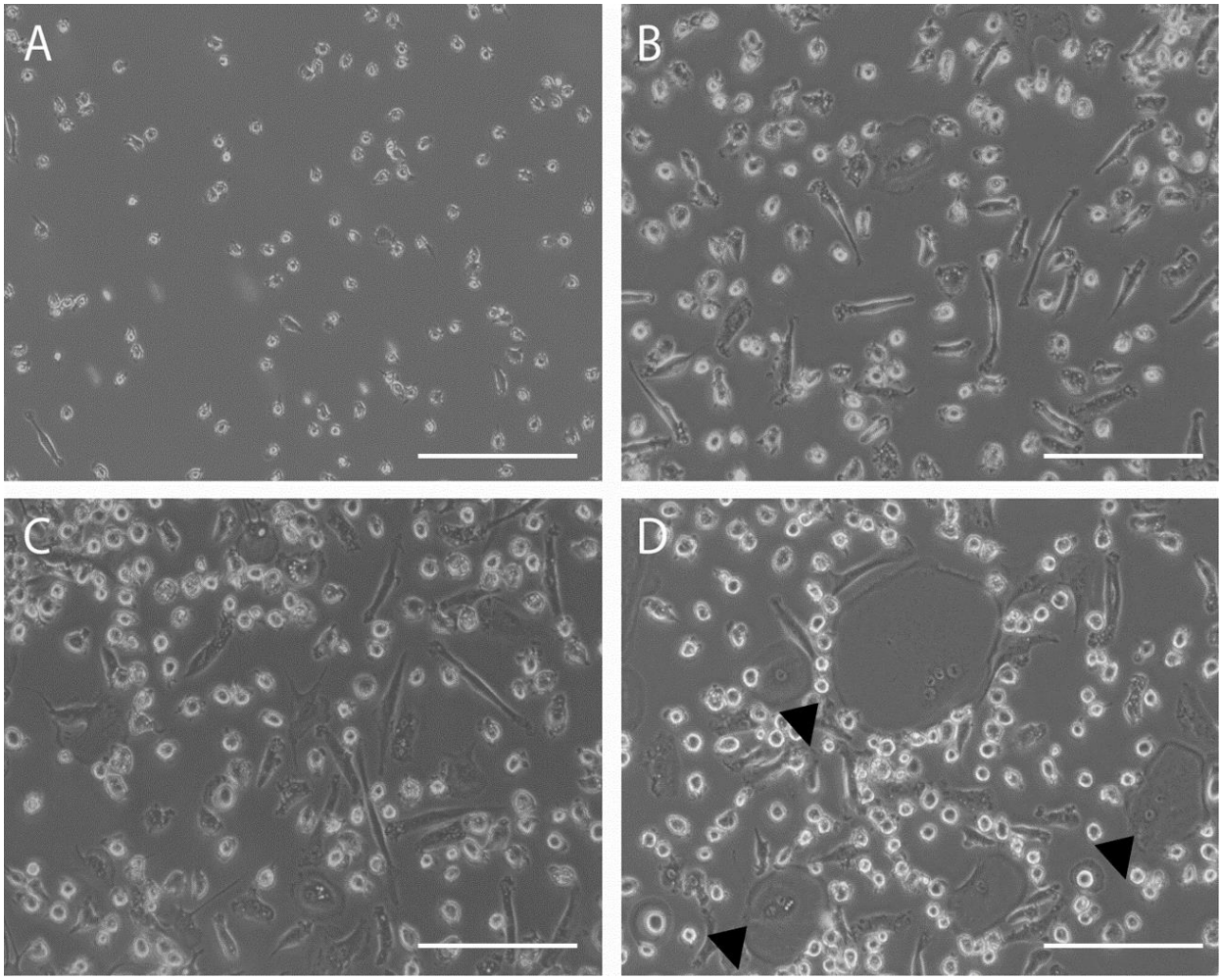

Figure III.17. Representative images of cellular morphology during osteoclastogenesis maturation period. A) Day 2: cells are small, spherical and mononuclear. There are a significant number of cells non-adhered to the surface yet. B) Day 5: it is possible to notice different cell populations appearing, although osteoclastic-like cells cannot be distinguished yet. C) Day 7: some cells begin to display an osteoclast-like appearance with larger cytoplasm, although any multinucleated cell was spotted. D) Day 9: it is clear the presence of punctual giant multinucleated cells with a characteristic osteoclast-like phenotype (marked with black arrows). Scale bar: 200 µm.

2.2.2. Functional experiments

2.2.2.1. TRAP staining

The evaluation of differentiation of monocytes to mature osteoclasts was firstly assessed through the analysis of the phagocytic cells-specific marker TRAP (Figure III.18) after 72h post-osteoclast maturation period.

In TCPS standard cultures, it is clear the presence of an osteoclast phenotype: giant multinucleated cells with purple TRAP-positive staining. Despite the verified phenotypic differentiation of monocytes to osteoclasts, the formation of sealing zones is typically not seen when these cells are cultured on unnatural surfaces like TCPS or glass [120].

Nonetheless, when cultured in a calcified subtract these cells present a completely different phenotype. It is possible to see the presence of the resorption pits (violet depressions marked with ‘’*’’ in Figure III.18). No multinucleated cells are noted, presumably because were already in the detachment phase after functional activity and were washed during the staining procedure.

These suggest that different substrates influence the morphology and potentially the function of osteoclasts. Thus, a matrix that mimics the natural surroundings of cells should lead to a better comparison between *in vitro* experiments and the *in vivo* scenario.

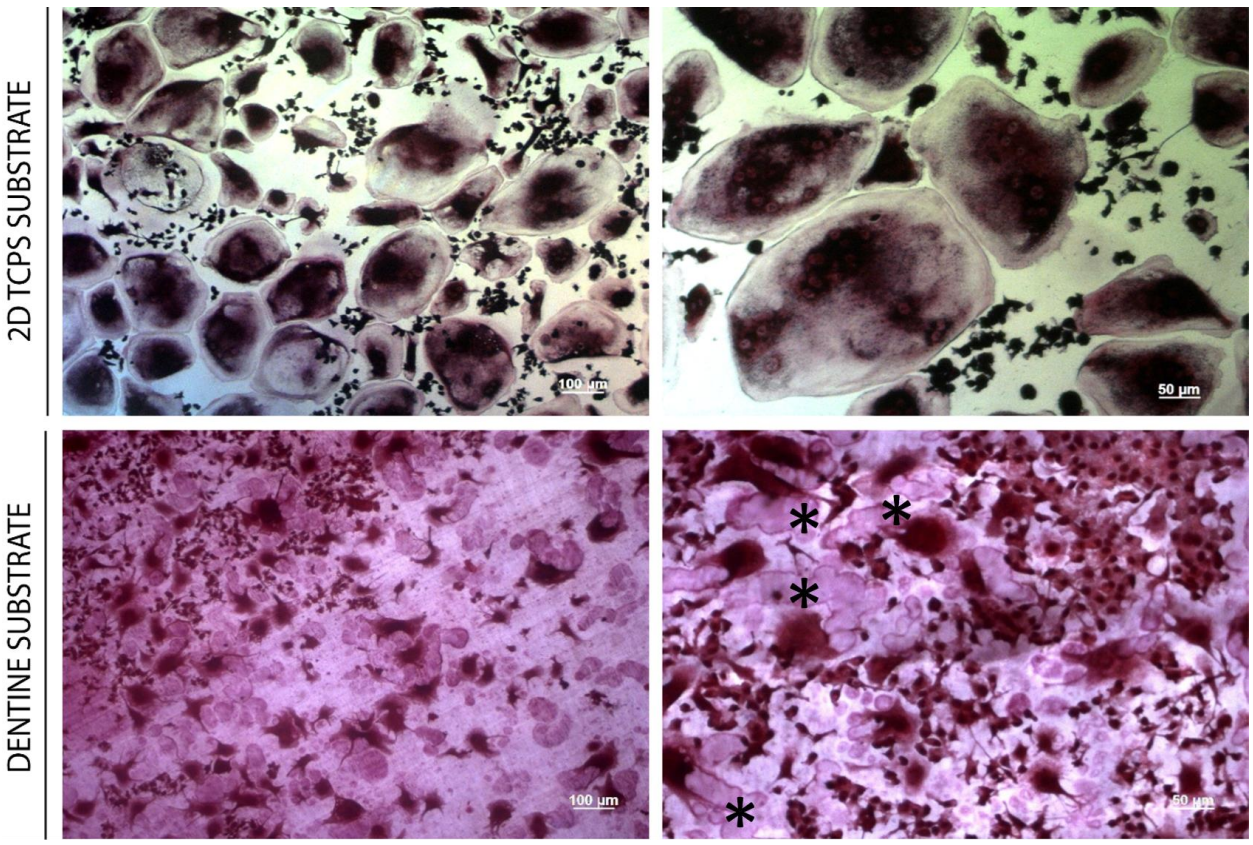

Figure III.18. TRAP staining of osteoclasts seeded in 2D standard TCPS surfaces and on top of calcified dentine substrates. Resorption pits are marked with ’’ * ‘’ symbol.

2.2.2.2. SEM analysis

The bone matrix represents the natural environment of osteoclasts, consisting of inorganic hydroxyapatite and to a minor part of organic components, such as collagen type I and bone specific proteins [117]. Whence, the culture of osteoclasts on top of dentine calcified discs allow to obtain a key defining system to evaluate the resorption activity of these cells.

Dentine is a hard calcareous bone-like structure, composed of calcium hydroxyapatite with small amounts of calcium carbonate, calcium fluoride and magnesium phosphate, which are usually used as bone resorption substrates [121]. The chemical composition of dentine discs was verified through the energy dispersive X-ray analysis of backscattered electrons on these structures (Figure III.19).

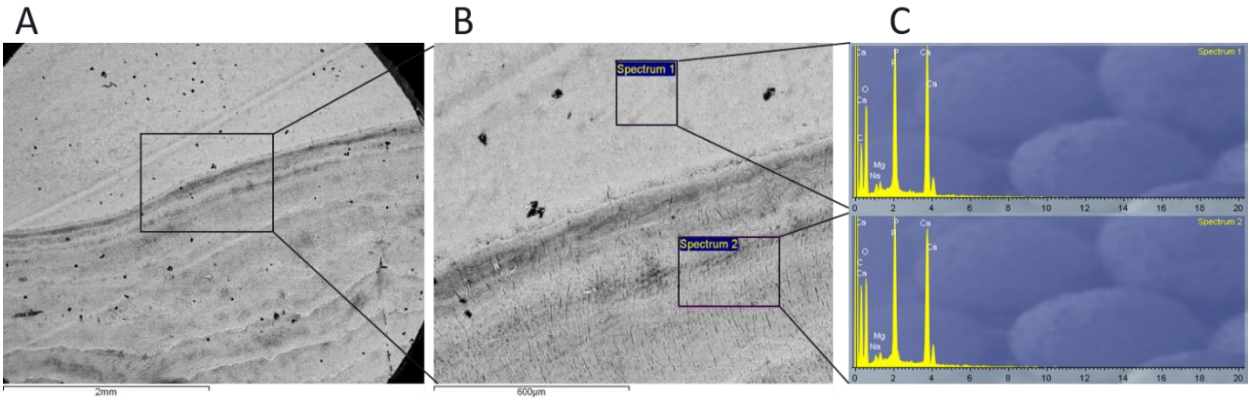

Figure III.19. SEM/EDS analysis of dentine discs. A) Wide backscattered electron (BSE) image of a representative dentine disc. It is commonly distinguished a denoted difference of different portions of disc. B) Zoom-in BSE image of chemical frontier of dentine. C) Energy Dispersive X-ray Spectroscopy (EDS) graphs of elemental composition on both portions. The only noteworthy change is the lower presence of carbon in spectrum 1 when compared with Spectrum 2. The occurrence of carbon in the structure do not affect the bone-like chemical structure of dentine disc, therefore, it could be stated that this variance is not significant to the overall role of these substrates.

When qualitatively compared the structure of an intact disc with the discs that were in culture with osteoclasts (Figure III.20), it is strikingly verified the presence of several resorption lacunae. In fact, it is very clear the polarization of these cells on top of these lacunae described in literature [55] - the osteoclast cells exhibit a visibly ruffled border in the basal membrane which is in contact with the bone surface from where they secrete protons and the enzymes responsible for the degradation of bone. It is also possible to note the cytoplasmatic extensions that they form in order to physically isolate these cavities from the rest of the surface.

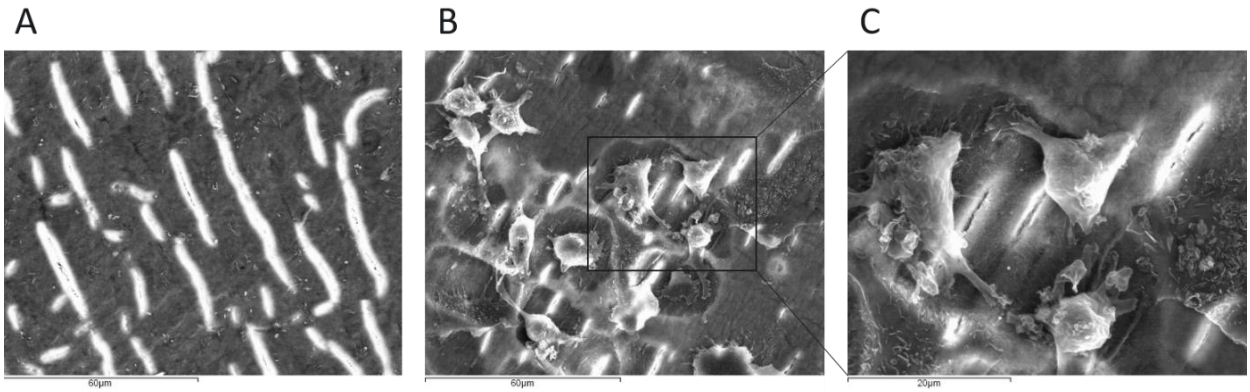

Figure III.20. SEM - SE images. A) Secondary electron (SE) close-up image of an intact dentine disc (without cells). It is possible to observe some characteristic bright scratches in the structure, presumably due to the existence of some protuberances in the structure. B) SE image of osteoclast cells cultured in dentine discs for 72h. C) Detail of osteoclasts spread around a lacuna roof.

2.2.2.3. F-actin staining

Within the differentiation process, osteoclasts modulate their F-actin cytoskeleton forming characteristic actin rings that isolates the acidified resorptive microenvironment from the general extracellular space [122].

The modulation of cytoskeleton was examined by an actin staining with fluorescent labelled phalloidin of osteoclasts in culture for 72h either in TCPS (Figure III.21) and in dentine substrates (Figure III.22).

In TCPS culture, it is clear the establishment of a nearly pure population of giant multinucleated cells. It is notable that cells with more than 10 nuclei exhibit a significant larger cytoplasmatic area which mates the progressive maturation of osteoclasts by fusion of progenitors cells.

It is generally observed that their cytoskeleton is tightly organized in podosomes mostly arranged as a band in the periphery of the cells. These dot-like structures are actin-rich adhesive structures that are postulated to be a result of a failed resorption [120] – in the absence of a calcified matrix, osteoclasts are not capable to form a sealing zone and then start their secretory resorption activity.

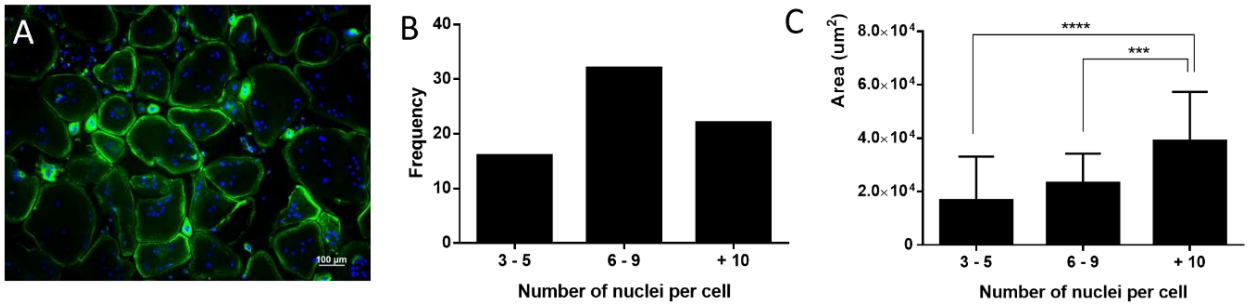

Figure III.21. Morphological analysis of osteoclasts cultured in TCPS surfaces. A) Representative image of 488-phalloidin staining. Nuclei are stained with Hoechst. B) Nuclei per cell frequency analysis. C) Cell area measurements distributed by number of nuclei per cell quartiles (n=70 cells, *** p<0.001, **** p<0.0001).

In comparison, cells differentiated on dentine substrates generate multi-nucleated cells capable of modulating their F-actin in actin rings which build up sealing zones between the cells and the bone-like matrix (Figure III.22). It is reported an overlap correlation between the actin rings diameter and the resorption pits length [120] of primary human osteoclasts on top of 2D bone matrix substrates, implying the formation of functional active osteoclasts.

These sealing zones were observed only on dentine substrates and not on TCPS. The morphological differences of primary human osteoclasts in actin modulation and sealing zone formation detected, confirm the importance of the environment that is used as culture substrate for the *in vitro* generation of active osteoclasts.

The cell size and frequency of multinucleated cells analysis reflect the major presence of cells with less than 5 nuclei to the detriment of larger multinucleated cells. Although, in these substrates it is not possible to fully individualize cell borders along the z-axis due to their semi-dimensionality, which interfere with phenotypic analysis.

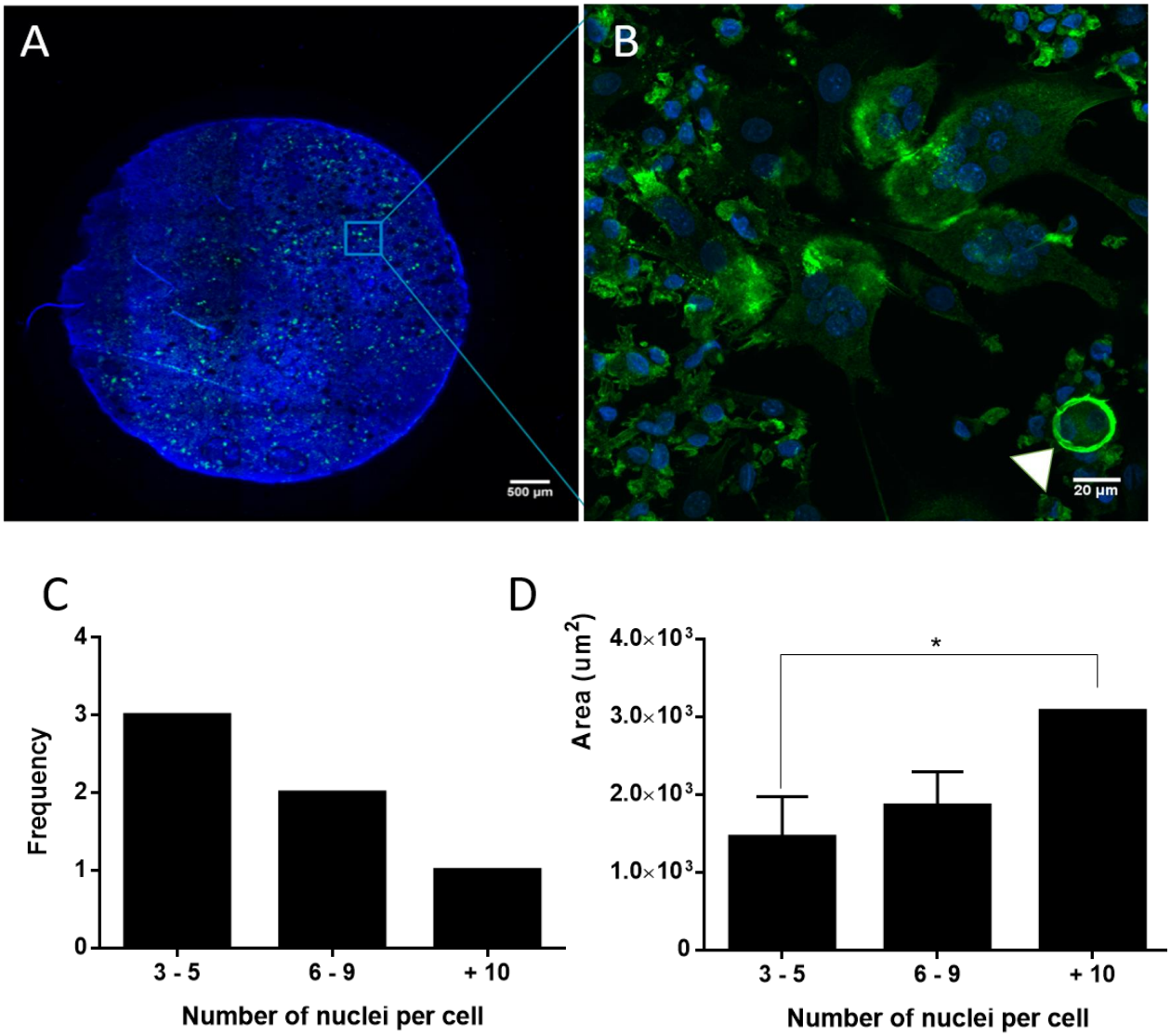

Figure III.22. Morphological analysis of osteoclasts cultured in dentine surfaces. A) Cell distribution on dentine disc. Osteoclasts spread themselves in dentine substrate in a homogeneous way which indicates the full acceptance of cells to the substrate. It is also possible to note the strong auto-fluorescence of dentine disc in blue channel. B) Representative image of 488-phalloidin staining. Nuclei are stained with Hoechst. A representative actin ring is marked with a white arrowhead. C) Nuclei per cell frequency analysis. D) Cell area measurements distributed by number of nuclei per cell quartiles (n=6 cells, * $p<0.05$).

2.2.2.4. 3D reconstruction of resorption pits

Osteoclasts and other phagocytic cells can all ingest and degrade very small particles of bone either *in vitro* or *in vivo.* However, only osteoclasts can create resorption pits on bone [113]. The analysis of resorption pits is, therefore, the key defining attribute and best quantifiable assay for evaluating the bone resorptive activity of fully developed osteoclasts.

After maturation period, osteoclasts were detached from the dentine discs and these were fluorescently labelled with calcein-AM. Osteoclast-generated resorption pits were reconstructed from calcein stained stacked images (Figure III.23A) using an original Matlab program (Figure III.23B) [103].

The program returns the 3D reconstructed images of resorption pits as well as the quantified measurements of a series of shape descriptors. Particularly, the volume and the top section area are vital statistics useful to compare the osteoclast activity in bone metastasis niche experiments.

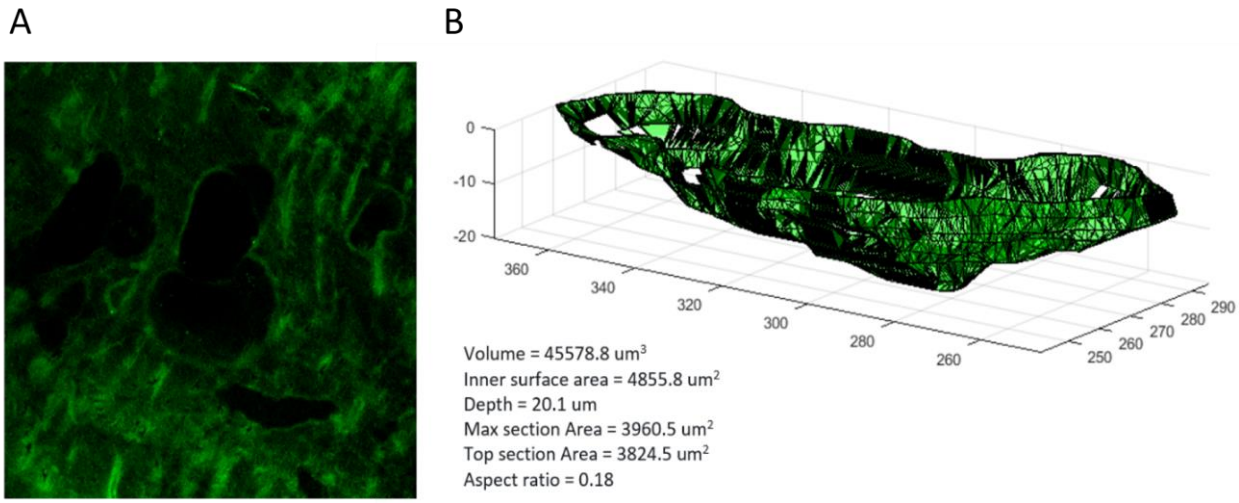

Figure III.23. 3D reconstruction of osteoclast-generated resorption pits. A) Confocal image of a representative resorption pit stained with calcein-AM dye. Calcein binds to calcium deposits and fluoresces, allowing to have a complete labelled topography of dentine structure. B) Corresponding 3D reconstruction of selected representative resorption pit. The outcome shape measurements are presented in bottom.

2.2.2.5. MMPs activity analysis

The matrix metalloproteinases comprise a family of zinc-dependent endopeptidases that have the capacity to cleave extracellular matrix. Recently, MMPs have been described to be involved in tumour-promoting activities, such as activation of latent growth factors. Indeed, MMP activity has been shown to be required for establishment and growth of metastatic cancer in bone. *Lee et al* demonstrated that the inhibition of MMP-2 and MMP-9 undermines the capability of bone degradation by tumour metastasis [123].

MMP-9 is produced principally by osteoclasts and cells of the immune system, and is known to be required for osteoclast migration and therefore their functional activity [124].

MMP-2 is secreted predominantly by fibroblasts and osteoblasts, and is involved in the activation of MMP-13 and degradation of the basement membrane. Enhanced expression of active MMP-2 has been correlated with breast cancer grade and disease progression [125].

The production of MMP-2 and MMP-9 was detected and quantified by zymography analysis (Figure III.24).

There is an ectopic expression of MMP-9 in control samples with only medium which refers to the protein present in the serum from bovine origin. The band is evident in all samples, and should not be considered in the analysis.

As expectable, there is a strong expression of MMP-9, although no significant differences are visible between osteoclasts cultured in TCPS or in dentine discs. The MMP-2 activity, although less expressive, seems to exhibit an enhanced expression in osteoclasts cultured in dentine discs, mainly the active form.

However, there are a large variability associated with results obtained from two experiments; and it is still not possible to distinguished between the pro and the active form of MMP-9. In order to achieve a better and efficient quantification of both MMPs and their respective pro and active forms, it is suggested to execute individual zymograms in which it would be loaded a smaller amount of sample in MMP-9 analysis and the gel run adapted to each experiment.

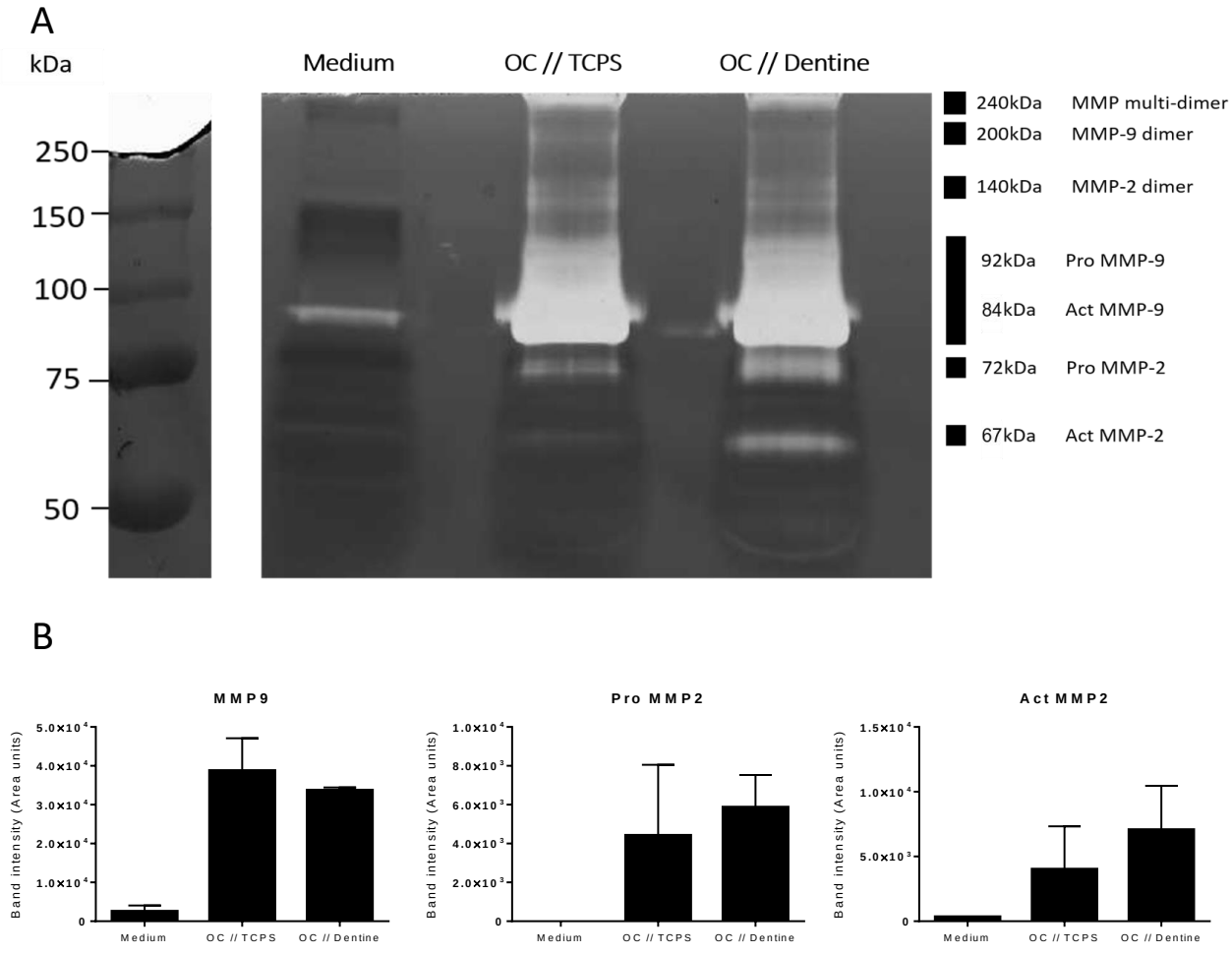

Figure III.24. Zymography analysis of MMP-2 and MMP-9 activity. A) Zymogram gelatine gel. Bands identification was recognised by their size with comparison with reported bibliographic [126] values. B) Quantification of MMP-2 and -9 activity. Quantification was performed by means of integrative intensity of the gelatinase bands using Fiji software (n=2).

2.2.2.6. Gene expression

Osteoclast differentiation mediated by M-CSF and RANKL can be distinguished in three lineage stages: the pro-osteoclast (spindle-shaped macrophage cells), the pre-osteoclast (small round mononucleated TRAP-positive cells), and the mature osteoclast (multinucleated TRAP-positive cells) stage. Each stage exhibit a characteristic gene pattern for specific osteoclastogenic markers [127].

M-CSF induces expression of RANK on these cells, priming them for further differentiation in response to RANKL. In response to RANKL, expression of a number of transcription factors that regulate further differentiation of RANK-expressing cells is increased. These include c-Fos, and NFATc1. They induce expression of several gene-encoding proteins involved in osteoclast activation, including TRAP, Ctsk, and CTR, and mediate production of H+ and Cl-, which form HCl under the ruffled borders of osteoclasts.

A screening of osteoclastogenic genes was performed in order to assess the stage of differentiation of osteoclasts cultured for 9 days in dentine discs (Figure III.25).

The low expression of NFATc1 and c-Fos in conjugation with the high expression of TRAP and Ctsk point to an advanced stage of differentiation of these cells.

Despite the mature characteristics, these cells exhibit an unexpected shallow expression of RANK. This surprising result is supposedly attributed to the low PCR efficiency of the primer designed. Nevertheless, it is the analysis of gene pattern profile in microfluidic experiments that will ultimately allow concluding about the over-activation of osteoclasts within the metastatic niche.

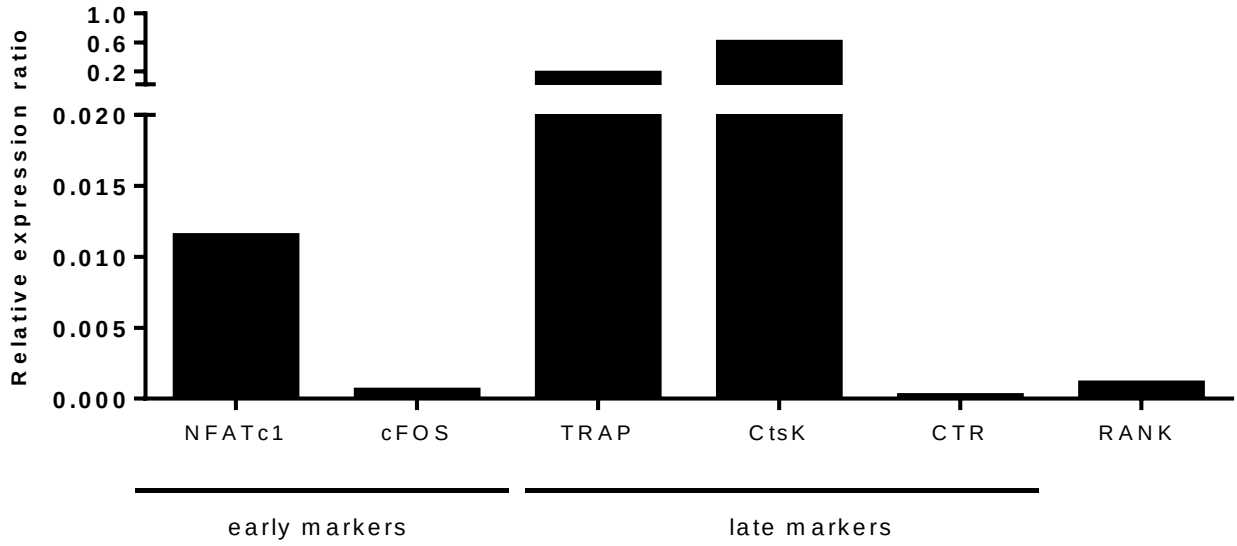

Figure III.25. Osteoclastic gene expression analysis. The expression values of each gene were normalized with expression of B2M gene.

2.3. Osteoblast/Osteoclast co-cultures

As a concept proof of bone co-culture system, MSCs were seeded on top of dentine discs with osteoblast differentiation medium and pre-osteoclasts were seeded on top of differentiated MSCs. The optimized conditions were further investigated.

2.3.1. TRAP staining

Pre-osteoclasts with 7 days of differentiation were seeded on top of MSCs at different stages of differentiation (1, 7 or 14 days).

The maturation period of osteoclasts was reduced from 9 days to 7 days, because it was estimated to be the period where there are more osteoclast precursors in culture – since that the multinucleated cells observed in culture flask are lost during the passage.

After 4 days of co-culture, a TRAP staining was performed (Figure III.26).

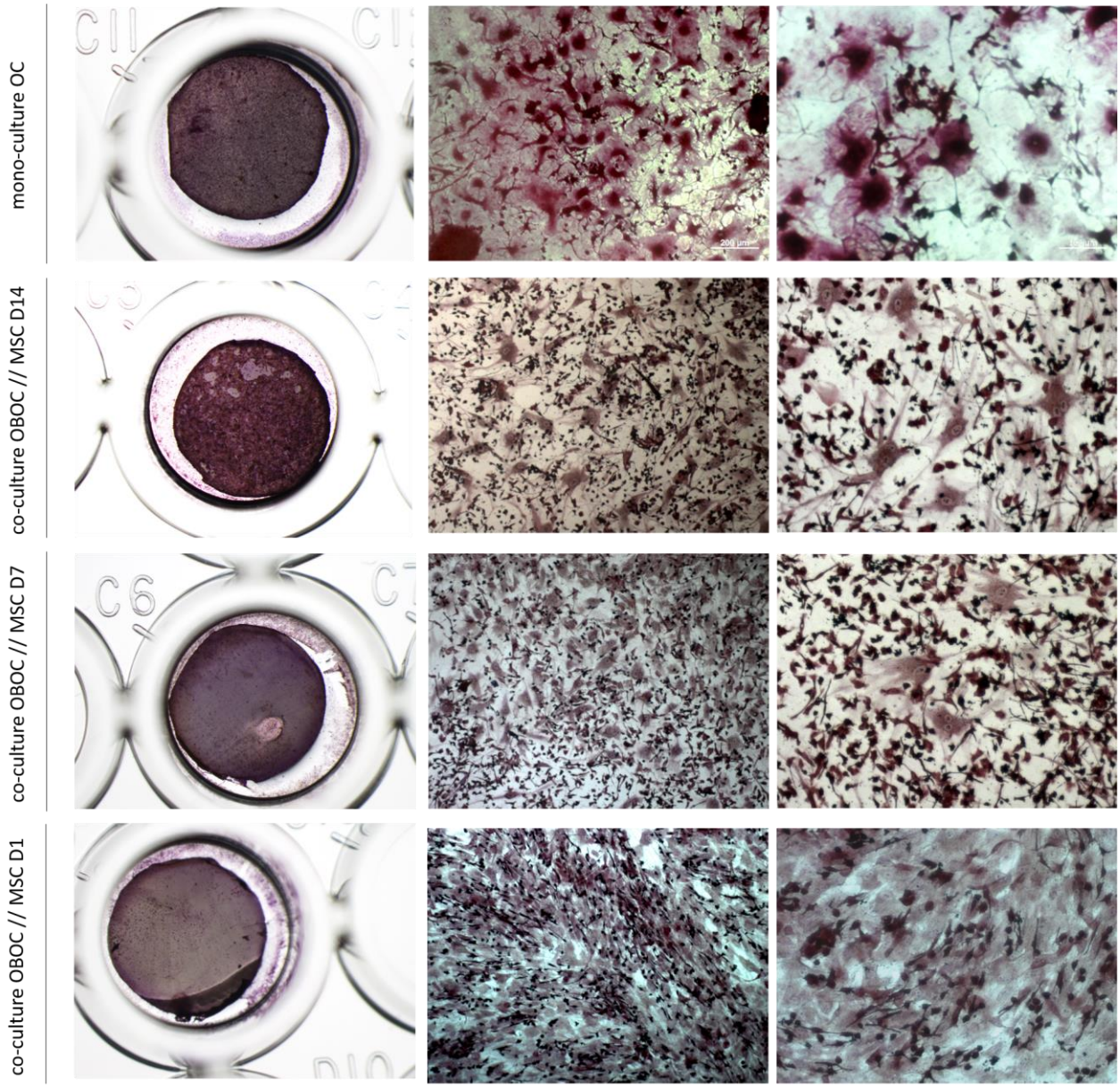

Figure III.26. TRAP staining of osteoclast/osteoblast co-culture on top of dentine discs. Monoculture of osteoclasts supplemented with external M-CSF and RANKL was used as a control. MSCs with different periods of differentiation (Day 1, 7 and 14) were tested.

In osteoclast monoculture, as previously reported, it is possible to observe multi-nucleated TRAP-positive cells.

For co-culture systems, as expected, it is observed the presence of big spreaded cells with mesenchymal phenotype blended with small TRAP-positive cells. Concerning the presence of osteoclast cells, it is very tricky to distinguish them in co-culture systems, mostly in co-culture of MSCs cells with 1 day of differentiation. For co-cultures with 7 and 14 days of osteogenic differentiation is already possible to observe some TRAP-positive cells similar to the osteoclast monoculture, although not clearly.

TRAP staining is, therefore, not ideal to conclude about the presence of multinucleated mature-osteoclasts in co-culture systems. Further phenotypic studies are desirable.

2.3.2. F-actin staining

The morphology phenotype and the cell distribution over the dentine discs was evaluated by F-actin staining for both monoculture and co-culture system between osteoblasts and osteoclasts cells (Figure III.27).

Similarly to what was observed before, in osteoclast monoculture it is possible to detect the presence of multinucleated cells with characteristic actin rings.

Both in MSCs monoculture and OB/OC co-culture is evident the oriented and spread distribution of MSCs indicating a good adaptation of these cells to the substrate. In co-culture system it is possible to observe a complete covering of dentine surface with MSCs. Nevertheless, it is not possible to detect multinucleated cell with osteoclast morphology. The superior cell density of MSCs difficult the visualization and individualization of osteoclast cells.

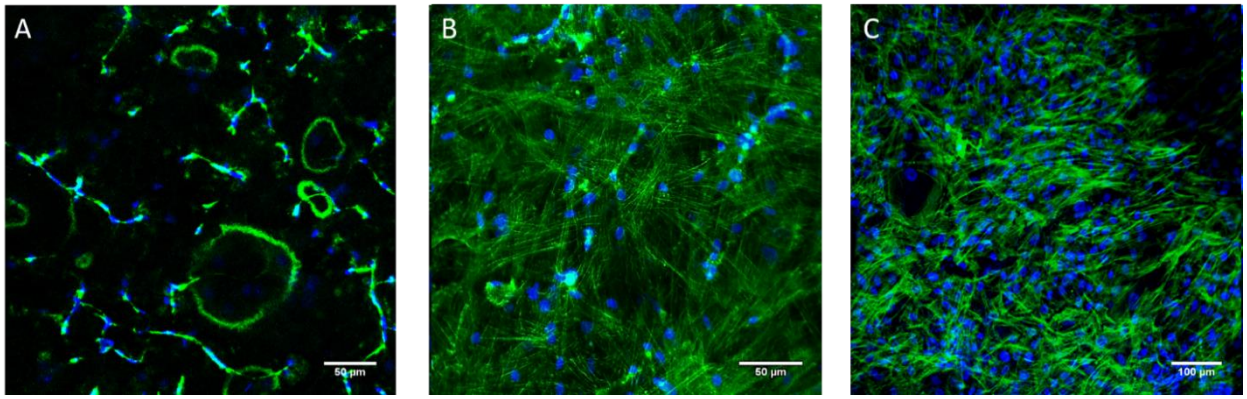

Figure III.27. Bone co-culture morphology on dentine discs: Phalloidin 488 and Hoechst 33342 staining. A) Osteoclast monoculture. B) MSCs monoculture. C) OB/OC co-culture. MSCs in passage 9 were differentiated for 14 days.

To overcome the handicap to visually individualize osteoblasts and osteoclasts in co-culture system it is suggested a co-localization of each cell type using specific cell markers with different fluorophores – e.g. it could be used a commercially available MSCs cell line transfected with GFP, while the detection of osteoclasts multinucleated cells could be assessed through Ctsk immunostaining using a secondary antibody coupled to a red fluorophore.

3. Microfluidic cultures

Cells exist *in vivo* in carefully maintained microenvironments within three-dimensional communities. Particularly metastatic niche comprises a great number of crosstalk relationships that positively affect both home-bone cells and metastatic cancer cells. However, *in vitro* cellular microenvironments are typically characterized by long distances between cells, large fluid stress and cell volume/medium ratio less than one. Microfluidic technology can facilitate the study of cell behaviour *in vitro* with more reproductive models that, when properly designed, can reassemble the intrinsic characteristics of *in vivo* niche.

Although, the design of a microscale cell culture device presents a number of unique challenges, many of which have been already discussed [128].

3.1. Preparation of microfluidic devices

Due to size restrictions, the commercially available microfluidic chambers (Figure III.28A) are not suitable for the system intended – first, the large spheroid size does not allow a workable manipulation through the main channel of microfluidic; and additionally, the bi-compartmentalization of each side of the chamber would not allow a fluidic equilibrium if the dentine disc was placed on one of the wells.

Henceforward, two different chambers were created using a master mold of a silicon and circular compartments were posteriorly shaped (Figure III.28B and C). Although, the produced chambers exhibited a slight difference on PDMS integrity levels that restrains the correct assembly on PDL pre-coated glass slides. The increased softness was presumably attributed to the solidification process, although every optimization attempts were failed.

Ultimately, to overcome either the size restrictions of commercial chamber and the PDMS integrity of the newly fabricated chambers, commercial chambers were shaped outwardly with two new compartments (Figure III.28D). A compartment of 3 mm length was cut on left side of each chamber designed to hold the spheroid structure; A compartment of 8 mm length was symmetrically cut on middle zone of the right side where the dentine disc it will be placed.

This last strategy successfully allowed either the correct assembly of the entire platform, and the workable compartmentalization adapted to cellular systems involved in the model.

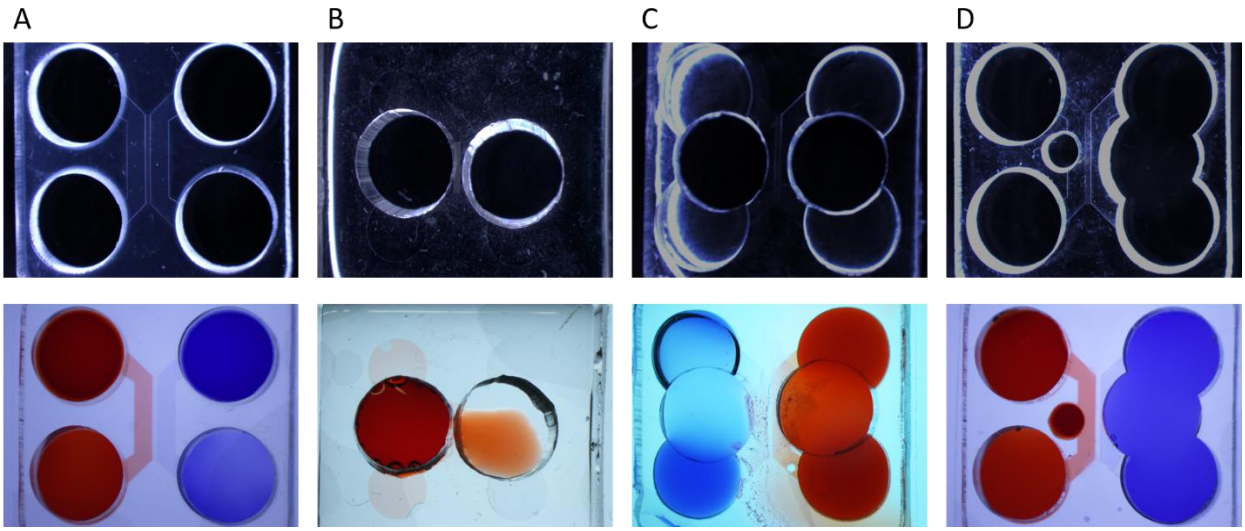

Figure III.28. Microfluidic chamber design strategies. The magnified images of each design approach are represented in the first row. The chambers were assembled in PDL pre-coated glass slides and their quality was evaluated through dyes distribution over the compartments – images represented in the second row. For B and C approaches dye solutions overpassed the confined compartments within minutes.

3.2. Cell behaviour in microfluidic system

3.2.1. MCF-7 Spheroids

In order to evaluate the effects of bone cells on breast cancer cells behaviour, MCF-7 spheroids were cultured in microfluidic culture with OB/OC co-culture system.

In order to reduce the variables of the system, the final platform was achieved by the progressive culture of both osteoclasts and osteoblasts independent monocultures with MCF-7 spheroids.

To rule out the potential effects induced by the media of bone cells in MCF-7 activity, microfluidic control experiments were also performed in the presence of either osteoclast and osteoblast medium.

3.2.1.1. Structural dispersion

MCF-7 spheroids' structural changes were determined through the analysis of the differential between total spread area and the original confined spheroid middle-section area (Figure III.29).

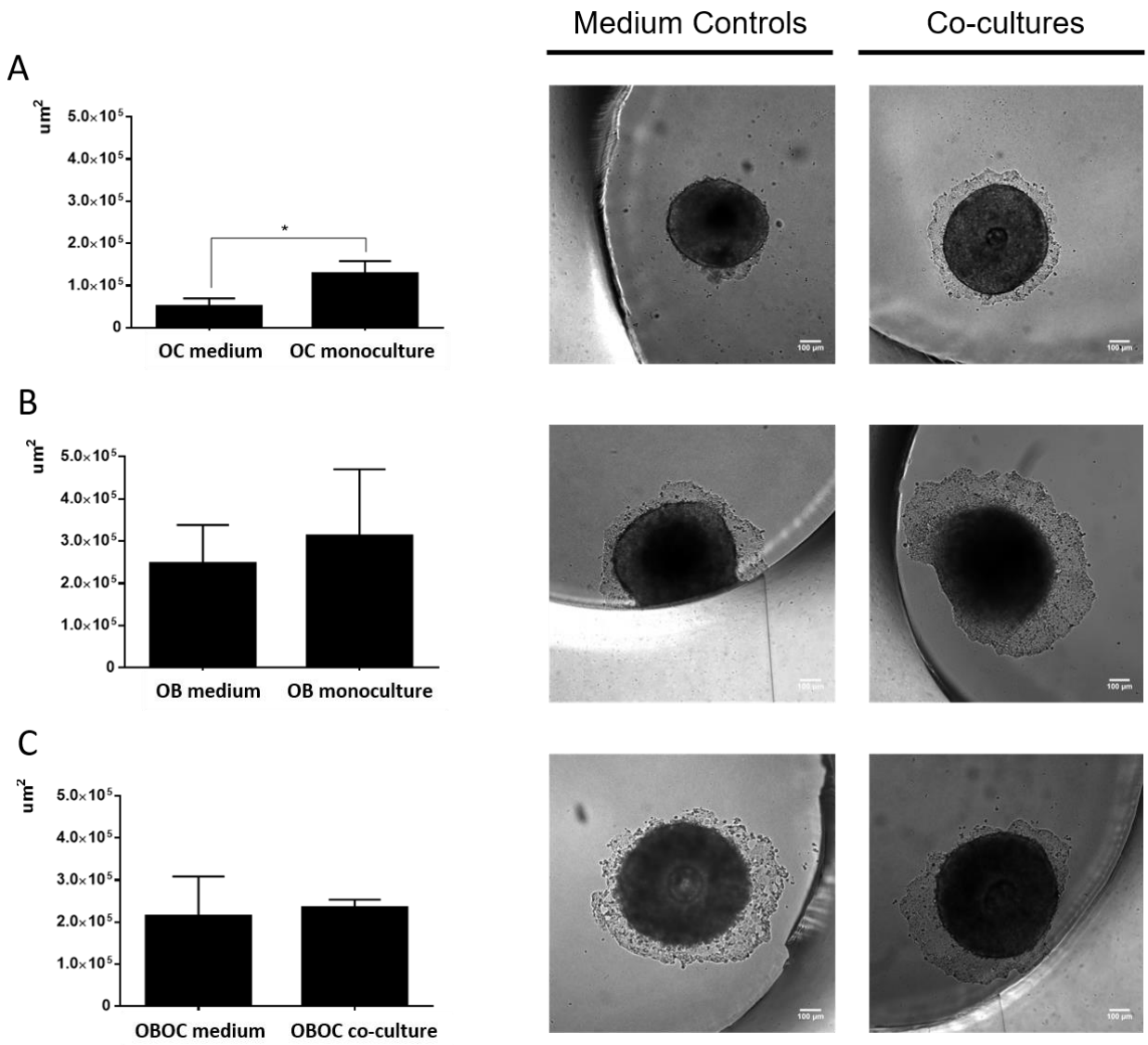

Figure III.29. Spread area of MCF-7 spheroids in microfluidic culture with bone cells. A) MCF7–Osteoclast monoculture experiment. B) MCF7–Osteoblast monoculture experiment. C) MCF7–OB/OC co-culture experiment (n=5, * p<0.05).

MCF-7 spheroids in microfluidic culture with osteoclasts (Figure III.29A) exhibit a significant loss of original structure when compared with the control condition. Cells appear to be influenced by factors secreted from the bone compartment.

In the meantime, for osteoblastic (Figure III.29B) and OB/OC co-cultures (Figure III.29C) the overall spreading of MCF-7 cells are 2-fold increased. However, this increase appears to be induced by bone cells co-culture in microfluidic culture as well as by osteoblastic medium itself.

It is hypothesized that the extraordinary dispersion of MCF-7 spheroids in this conditions is presumably a result of the activation of MCF-7 cells by the phenol red present in the osteoblastic medium. Phenol red is reported to possess estrogenic properties, stimulating MCF-7 cell proliferation in a dose-dependent manner [129]. Whereas osteoclastic medium does not present phenol red concentrations in their constitution to affect MCF-7 cells.

Therefore, it is preliminary concluded that the microfluidic culture with bone cells indeed affect the MCF-7 spheroid structure in a significant way, although the comparison with media controls is a requirement.

3.2.1.2. Gene expression

The gene expression of metastatic markers was comparatively analysed for each condition of microfluidic system (Figure III.30).

The expression of VEGF remains lower than the basal conditions for all conditions except for the OB/OC co-culture system. The overexpression of VEGF confirms the enhanced effect of bone cells in cancer aggressiveness, reported in the literature [9]. Interestingly, this overexpression is not manifested in microfluidic culture in respect to bone monocultures, which implies the mandatory interplay of both cell types in tri-culture system.

The same pattern is shown for RANK expression, although the RANKL does not seem to be affected in MCF-7 cells in culture with bone cells.

These results are consistent with the literature [130] – several studies have analysed the RANK, RANKL expression of breast cancer cell lines (HCC70, MCF-7, MDA-MB-231, MDA-MB-435, MDA-MB-453, T47D and ZR 75-1) using RT-PCR analyses. MCF-7, MDA-MB-231, and T47D expressed RANK, whereas RANKL expression was determined only in HCC70.

Taken these results together suggests that the efficacy on breast cancer cells of the metastatic vicious cycle reconstruction *in vitro* by this platform. Although, it is mandatory to increase the number of experiments to infer about their statistically relevance.

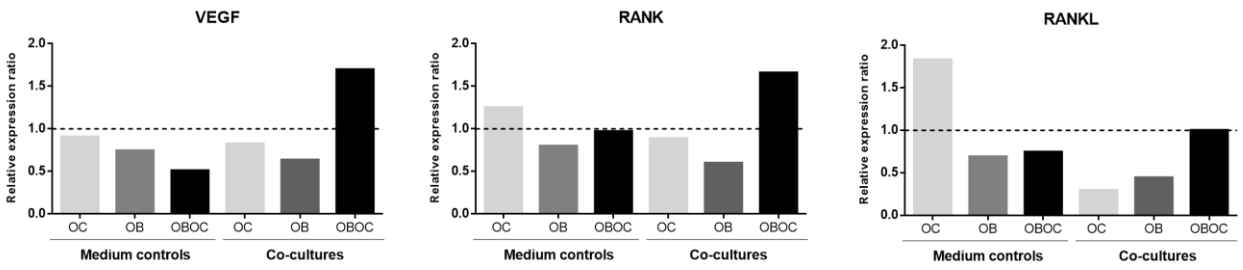

Figure III.30. MCF-7 gene expression analysis in microfluidic experiments. The expression values of each gene were normalized with expression of B2M reference gene and posteriorly standardised by the basal conditions, i.e. spheroid culture for 4 days in 96-well plate pre-coated with agarose (mark at y=1).

3.2.2. Bone system

In order to evaluate the opposite effect of breast cancer cells in bone system homeostasis, osteoclast and osteoblast monocultures as well as OBOC co-cultures were individually evaluated when in microfluidic culture with MCF-7 spheroids. Microfluidic cultures with only MCF-7 medium were used as control.

3.2.2.1. F-actin staining

Cell morphology was analysed by F-actin staining for both monoculture and co-culture systems between OB/OC in microfluidic culture with MCF-7 spheroids (Figure III.31).

For osteoclast monocultures, while is not observed multinucleated cells in microfluidic culture with MCF-7 medium, for the microfluidic culture with MCF-7 spheroids are visualized some large multinucleated cells and several actin-ring structures. These preliminary results indicate an increased activation of osteoclasts, which is expectable by the literature reports [58].

In osteoblasts monocultures, no significant alterations on cell morphology are detected between microfluidic cultures with medium and MCF-7 cells. MSCs exhibit a spread and fibrillary aspect, typical of fully differentiated osteoblasts, for both conditions.

Regarding OB/OC co-cultures, cells appear to be in a stressed state and already started to detach from the surface. This results indicate the need for a further optimization of microfluidic co-cultures; either the time-point of the experiment and the working volume for each compartment could induce a sheer stress that affect negatively cell behaviour either in a mechanical and/or in a bio-chemical way, that have to be explored. And again, a differential fluorescent co-localization of both cell types would be desirable in order to achieve a better visualization and identification of cells within the co-culture system.

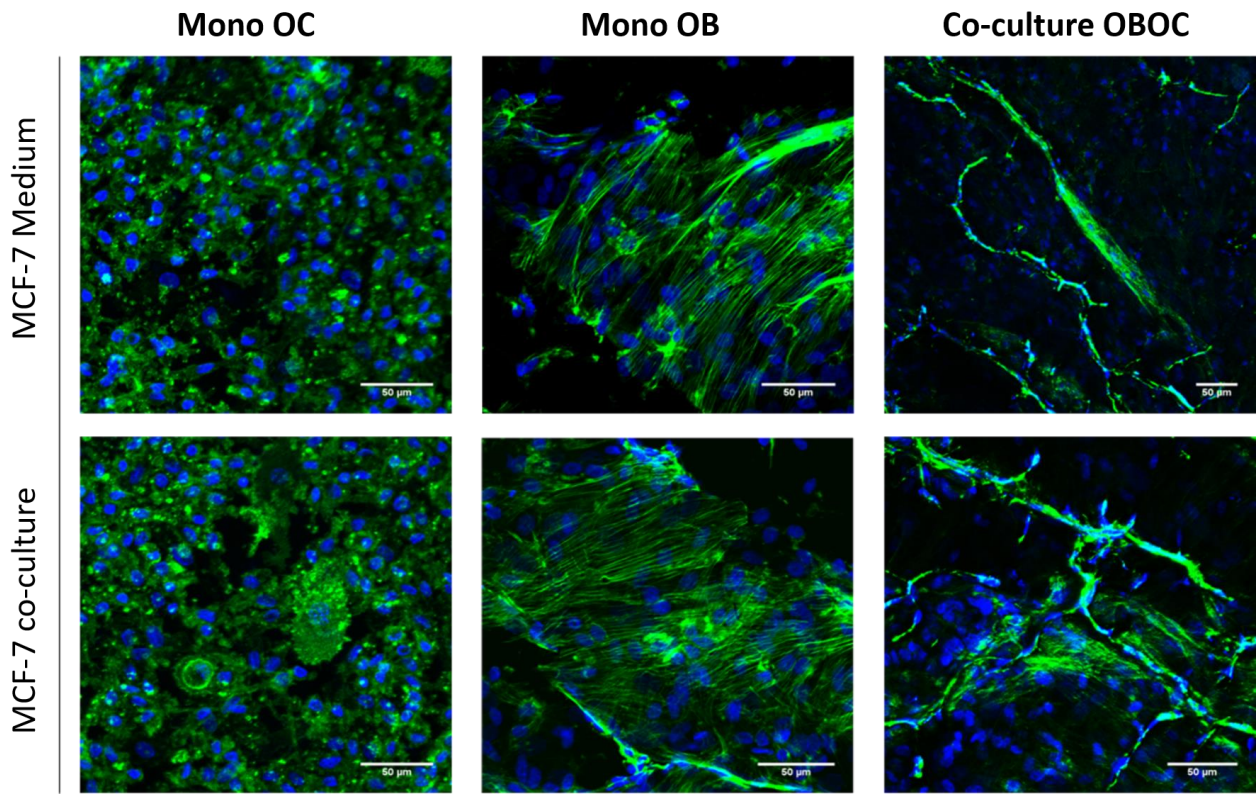

Figure III.31. Bone cells morphology in microfluidic cultures: Phalloidin 488 and Hoechst 33342 staining. It was analysed the influence of MCF-7 spheroids either for each monoculture system and for the final co-culture system. Microfluidic cultures with only MCF-7 medium were used as controls.

3.2.2.2. 3D reconstruction of resorption pits

In order to obtain quantifiable results of osteoclast activity, osteoclast-generated resorption pits were reconstructed from Confocal Microscopic images. The represented images and the quantification graphs are demonstrated and analysed in Figure III.33.

The measurements of resorption pits revealed a marked difference between microfluidic cultures controls with MCF-7 medium and microfluidic cultures with MCF-7 cells, with a remarkable increase in either Volume, Top Section Area and Depth. Although, no significant differences are shown between osteoclast monoculture and OB/OC co-culture.

Microfluidic culture with MCF-7 exhibits resorption pits that are deeper and wider than control cultures, and therefore a greater volume. Albeit, from the 3D reconstruction images it is possible to observe that pits from microfluidic cultures with MCF-7 are the result of the combined action of several sealing zones.

These results indicate a superior osteoclast activity in microfluidic cultures with MCF-7 hypothesising to be an effect of secretory factors produced by breast cancer cells in the scope of metastatic environment [58], although further experimental reproductions are essential.

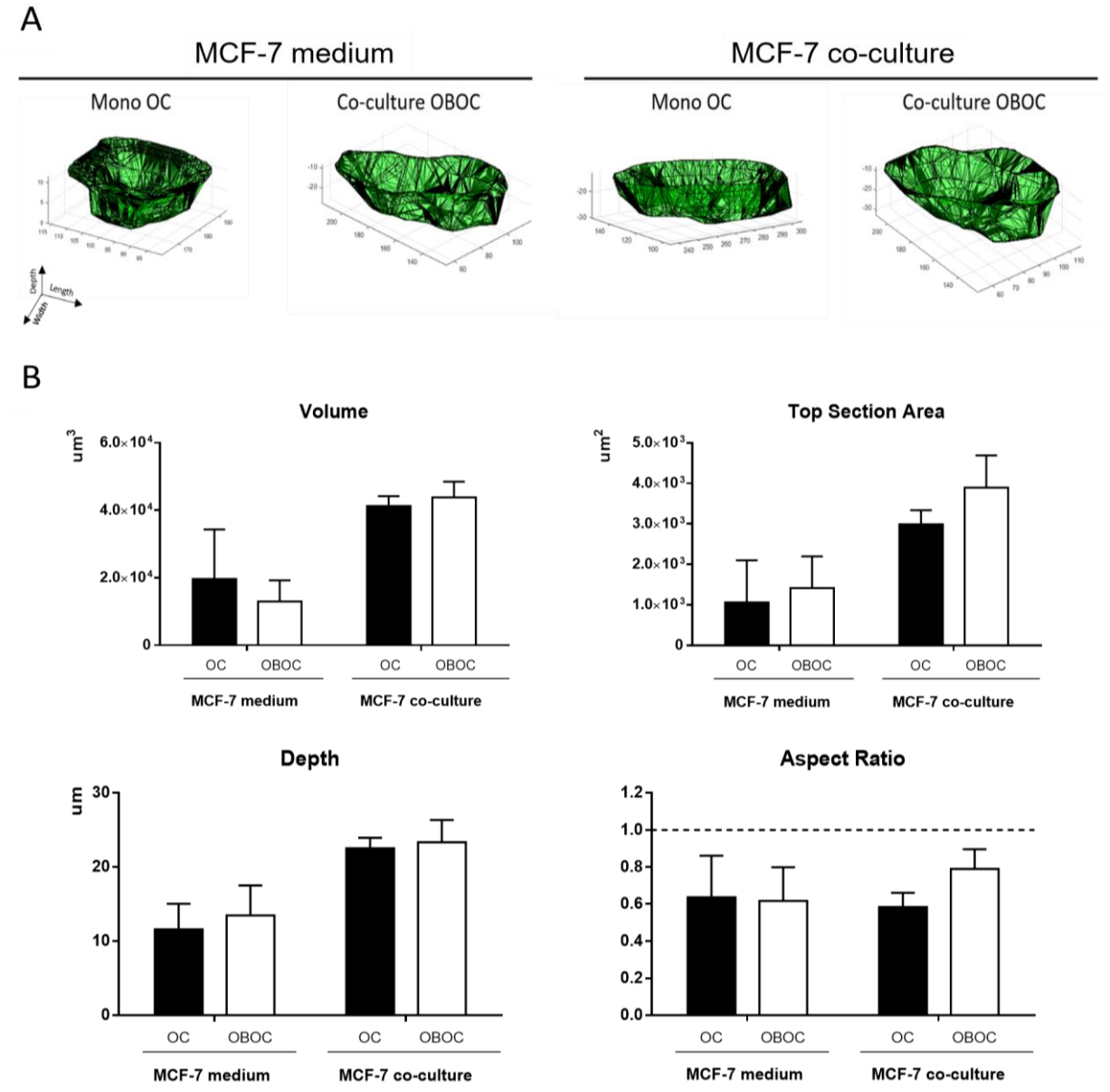

Figure III.32. 3D reconstruction of resorption pits in microfluidic cultures experiments. A) Representative images of 3D reconstruction for each condition. B) Quantification analysis of Volume, Top Section Area, Depth and Aspect Ratio (n=2).

3.2.2.3. MMPs activity analysis

MMPs present in media were analysed either in osteoclast monoculture microfluidic experiments (Figure III.33A) and in OB/OC co-culture microfluidic experiments (Figure III.33B).

The osteoclast monoculture results exhibit an increase of MMPs production in presence of MCF-7 spheroids when compared with the medium controls. The increase activity of MMP-9 reflects an over-activation of osteoclastic activity corroborating the previous results of osteoclast-generated resorption pits analysis. In the other hand, the increase presence of MMP-2 could presumably have origin of breast cancer cells.

In order to fully understand and theorize about MMPs production, further studies should be performed and complemented with advanced proteomic and genomic analysis for cell type.

Regarding to the OB/OC co-culture microfluidic experiments no remarkable differences are observed between MCF-7 culture and the medium controls for both MMPs analysed.

It is hypothesized, together with the previous results, that microfluidic culture time is not enough to observe sensible differences of MMPs secretions to the media. The number of independent experiments should be increased to assess the existence of a significant trend as well as further complementary studies are required to fully validate this results.

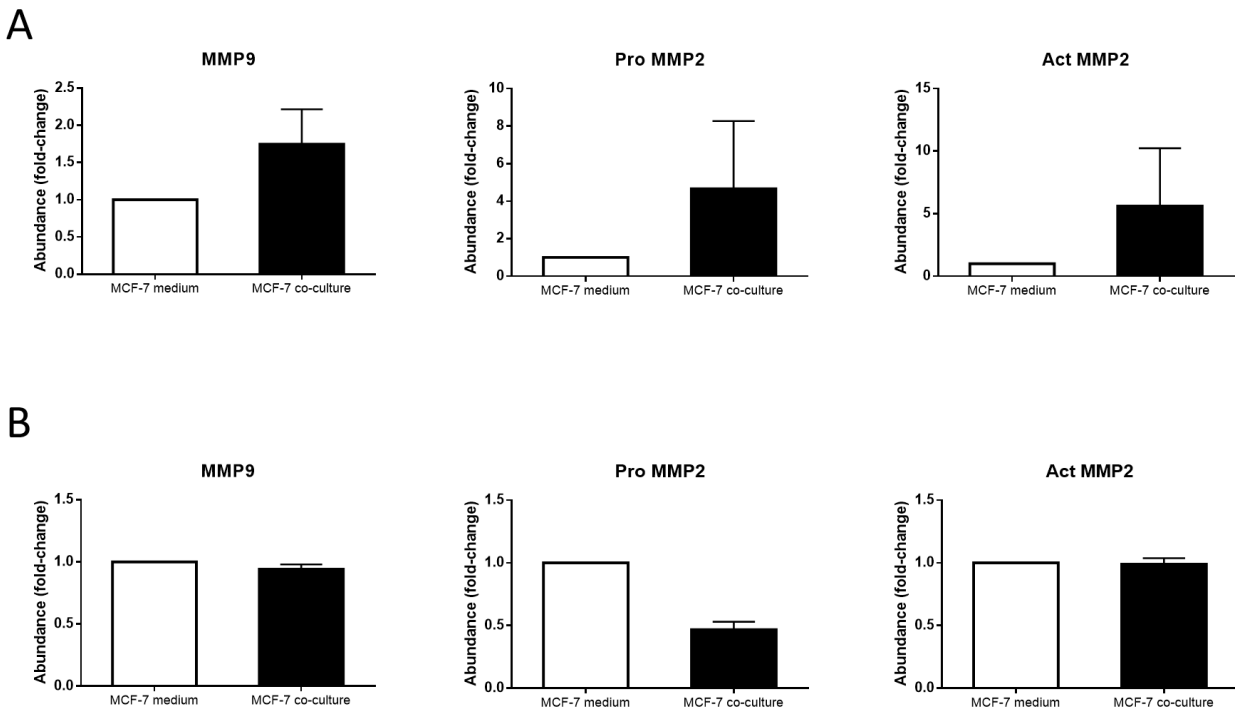

Figure III.33. Quantification of MMP-2 and MMP-9 activity. A) Osteoclast monoculture microfluidic experiments. B) OB/OC co-culture microfluidic experiments. Abundance of MMPs activity was normalized with the respective medium control for each sample (n=2).

3.2.2.4. Gene expression

Osteoblastic (Figure III.34A) and osteoclastic (Figure III.34B) gene markers were profiled for microfluidic experiments in order to assess early transcription changes, which will ultimately reflect cell behaviour. The results of co-culture system were compared either with osteoblast monoculture microfluidic experiments or osteoclast monoculture microfluidic experiments.

For osteoblastic analysis it is observed an extraordinary increase of differentiation markers in microfluidic cultures with osteoblast monocultures. Despite the positive expression of these markers in co-culture systems, the increased pattern is not verified. This result illustrates the variability intrinsic to the system that evidences the need for the statistical reproductions.

The osteoclastic analysis exhibits a generalized decrease of mature osteoclast markers. Although there is a substantial increase in expression of either c-Fos and CTR, particularly on microfluidic cultures with MCF-7 cells.

As osteoclast early marker, c-Fos subexpression indicates the presence of a major population composed by still not matured osteoclasts, which suggests that an extended co-culture period would be beneficial. On other hand, the superior expression of CTR signposts the presence of some fully active mature osteoclasts, which explain the osteoclast-generated resorption pits results.

Lastly, it is notable the prominent overexpression of both RANK/RANKL bone remodelling markers, particularly in microfluidic cultures with tri-culture system. This increased expression is the final statement that confirms the positive cross-effect of both cancer cells and bone cells within the metastatic niche. RANKL/RANK bind activate a cascade transduction pathway that culminates in the activation of osteoclast activity. The increased expression of these markers corroborates the previous osteoclast functional results and preliminary validates the over-activation of osteoclasts reported in breast cancer bone metastasis.

Taken together, it is possible to conclude about the pilot success of the microfluidic system assemble. However, further robust studies will be needed to clarify the outcomes obtained in this preliminary study.

A

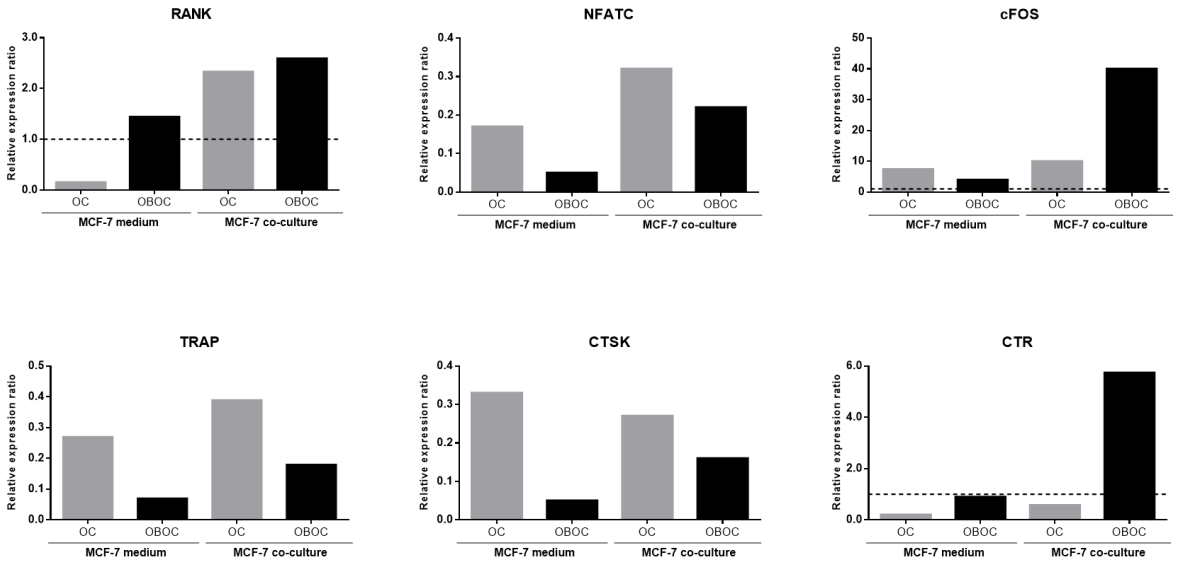

B

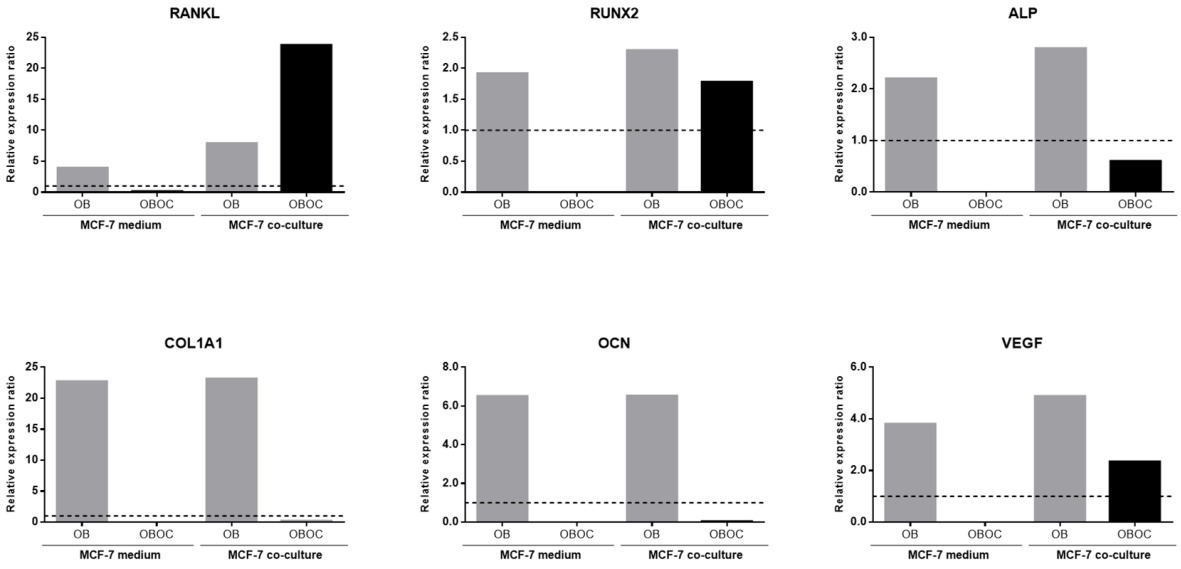

Figure III.34. Gene expression analysis in microfluidic experiments. A) Osteoblastic markers. B) Osteoclastic markers. The expression values of each gene were normalized with expression of B2M reference gene and posteriorly standardised by the basal conditions, i.e. either osteoblast or osteoclast monocultures on top of dentine discs in 96-well plate (mark at y=1).

Concluding remarks and perspectives

The development of breast cancer-induced bone lesions is predominantly based on a cooperative interaction between breast cancer cells and bone cells (osteoclasts and osteoblasts). The lack of ability to replicate the complex environment of human metastasis *in vitro* remains a critical barrier to understand the intricate vicious interplay and therefore explore more efficiently potential therapeutic targets.

In order to address this shortcoming, it was progressively optimized a novel tool based on microfluidic technology to tailor the human *in vivo* metastatic bone niche.

1. Both MCF-7 and MDA-MB-231 human breast cancer cell lines were efficiently assembled in spheroidal 3D structures in a highly feasible and regular liquid-overlay culture. Both the morphology and the apoptosis analysis of spheroids indicate the reassembling of a necrotic core within the inner portion reported *in vivo*.

As future perspectives in the scope of this project outline, it is proposed the system optimization of breast cancer cell lines with different immunogenic profiles. It was recently found a unique and dynamic interconversion of HER2 gene expression in circulating tumour cells found in breast cancer patients bloodstream: ER+/HER2- cells can spontaneously become ER+/HER2+ and convert back to ER+/HER2- [131]. The alternating expression of HER2 is dependent of different molecular signalling pathways and therefore their susceptibility to different anti-cancer drugs. Henceforward, a parallelization of microfluidic reactions would allow a high-throughput arrangement ideally suitable for screening potential therapeutic drugs in the pre-clinical phase.

2. hMSCs osteo-differentiation culture was optimized using osteoblastic medium supplemented with several combinations of inducing factors (dexamethasone, Vitamin D3, ascorbic acid and β-glycerophosphate). Osteoblast mineralization competence was positively accessed after 14 days of differentiation for combination #3, either through functional studies or osteogenic gene expression. Primary human blood-derived cells with osteoclastic potential were expanded in presence of M-CSF and RANKL and their osteoclastic activity were validated in calcified substrates by resorption functional assays and gene expression analysis. To establish bone co-culture system, 7 days-mature osteoclasts were seeded on top of 14 days-differentiated MSCs in dentine discs, reassembling either the chemical composition and structure of bone ECM.
The co-culture was maintained for 4 days. Either TRAP staining and F-actin of co-cultures were performed, although the individualization of both cell types were not clear in any of these studies, which preclude the validation of the system arrangement.

Therefore, it is mandatory a further optimization and validation of the bone co-culture system. To overcome the handicap to visually individualize osteoblasts and osteoclasts it is suggested a co-localization of each cell type using specific cell markers with different fluorophores – e.g. it could be used a commercially available MSCs cell line transfected with GFP, while the detection of osteoclasts multinucleated cells could be assessed through CtsK immunostaining using a secondary antibody coupled to a red fluorophore. Also the culture period of the experiment should be assessed.

3. The final tri-culture system was achieved through transfering both cancer and bone co-culture systems to the respective compartment of an optimized microfluidic chamber. The cross-effect between cells were assessed either by morphological studies, resorption functional assays or gene expression.

The morphometric analysis conducted in a high-throughput scan revealed that MCF-7 spheroids exhibit a tendency to lose their original 3D structure when compared with the control condition, probably influenced by the secretion of factors from bone compartment. These results are corroborated with the increased expression of VEGF and RANKL in presence of bone cells, which preliminarily indicate the recapitulation of the metastatic vicious cycle reported in the literature. Nevertheless, more complementary experiments are required in order to achieve statistically significant results.

On the other compartment, the bone co-culture analysis in microfluidic culture with MCF-7 cells suggest an over-activation of osteoclast activity, i.e. 3D morphological analysis of osteoclast-generated resorption pits, using an in-house developed quantitative computational tool (BonePit algorithm, MATLAB), showed a remarkable increase in resorption pit volume, area and depth when MCF-7 spheroids were present in cancer compartment. The increased expression of both RANK and RANKL in OB/OC co-culture experiments preliminary signposts a successful recapitulation of metastasis vicious cycle reported in the literature. However, these results lack in statistically relevance and further genomic and therefore proteomic studies should be performed in order to validate these assumptions.

Additionally, it should be designed and fabricated a fully original microfluidic chamber model with appropriated compartmentalization and structural integrity. Partnerships with specialized microfabrication research groups may be desirable.

Furthermore, as a prospective work it is also idealized the addition of a microfluidic compartment designed for the culture of nerve cells from peripheral nervous system. This will untimely recapitulate the metastatic bone niche main interactions *in vivo* and therefore, allow the study of pain mechanistic pathways reported in bone metastatic disease patients.

References

1. WHO, *World cancer report 2014 - International Agency for Research on Cancer*. 2014: Geneva: WHO.
2. Tavassoli, F.A., et al., *Pathology and Genetics of Tumours of the Breast and Female Genital Organs*. 2003.
3. Coleman, R.E., *Metastatic bone disease: clinical features, pathophysiology and treatment strategies.* Cancer treatment reviews, 2001. **3**(27): p. 165-176.
4. Kozlow, W. and T.A. Guise, *Breast cancer metastasis to bone: mechanisms of osteolysis and implications for therapy.* Journal of mammary gland biology and neoplasia, 2005. **10**(2): p. 169-180.
5. Dexter, R.M., A.H. Wyllie, and M.C. Raff, *The Role of Apoptosis in Development, Tissue Homeostasis and Malignancy: Death from inside out.* Springer Science & Business Media, 2012: p. 101-101.
6. Hanahan, D. and R. A. Weinberg, *Hallmarks of Cancer: The Next Generation.* Cell, 2011. **144**(5): p. 646-674.
7. Marusyk, A. and K. Polyak, *Tumor heterogeneity: causes and consequences.* Biochimica et biophysica acta, 2010. **1805**(1): p. 105-17.
8. Chiang, A.C. and J. Massagué, *Molecular basis of metastasis.* The New England journal of medicine, 2008. **359**(26): p. 2814-23.
9. Martin, T.A., et al., *Cancer Invasion and Metastasis: Molecular and Cellular Perspective*. 2000, Landes Bioscience.
10. Poste, G. and I.J. Fidler, *The pathogenesis of cancer metastasis.* Nature, 1980. **5743**(283): p. 139-146.
11. Chambers, A.F., A.C. Groom, and I.C. MacDonald, *Dissemination and Growth of Cancer Cells in Metastatic Sites.* Nature Reviews Cancer, 2002. **2**: p. 563-563.
12. Paget, S., *The distribution of secondary growths in cancer of the breast.* The Lancet, 1889. **133**(3421): p. 571-573.
13. Vanharanta, S. and J. Massagué, *Origins of metastatic traits.* Cancer cell, 2013. **24**(4): p. 410-421.
14. Joyce, J.A. and J.W. Pollard, *Microenvironmental regulation of metastasis.* Nature reviews. Cancer, 2009. **9**(4): p. 239-52.
15. Wan, L., K. Pantel, and Y. Kang, *Tumor metastasis: moving new biological insights into the clinic.* Nature Medicine, 2013. **19**(11): p. 1450-1464.
16. Weigelt, B., J.L. Peterse, and L.J. van't Veer, *Breast cancer metastasis: markers and models.* Nature Reviews Cancer, 2005. **5**(8): p. 591-602.
17. Zaha, D.C., *Significance of immunohistochemistry in breast cancer.* World journal of clinical oncology, 2014. **5**(3): p. 382.
18. Quail, D.F. and J.A. Joyce, *Microenvironmental regulation of tumor progression and metastasis.* Nature medicine, 2013. **19**(11): p. 1423-1437.
19. Perou, C., *S04 Molecular classification of breast cancer and its emerging clinical relevance.* The Breast, 2011. **20**: p. S2-S3.
20. Holliday, D.L. and V. Speirs, *Choosing the right cell line for breast cancer research.* Breast Cancer Research, 2011. **13**(4): p. 1.
21. Soule, H., et al., *A human cell line from a pleural effusion derived from a breast carcinoma.* Journal of the National Cancer Institute, 1973. **51**(5): p. 1409-1416.
22. Cailleau, R., M. Olivé, and Q.V. Cruciger, *Long-term human breast carcinoma cell lines of metastatic origin: preliminary characterization.* In vitro, 1978. **14**(11): p. 911-915.
23. Lacroix, M. and G. Leclercq, *Relevance of breast cancer cell lines as models for breast tumours: an update.* Breast cancer research and treatment, 2004. **83**(3): p. 249-289.
24. Levenson, A.S. and V.C. Jordan, *MCF-7: the first hormone-responsive breast cancer cell line.* Cancer research, 1997. **57**(15): p. 3071-3078.

25. Kang, Y., et al., *A multigenic program mediating breast cancer metastasis to bone.* Cancer cell, 2003. **3**(6): p. 537-549.
26. Bilezikian, J.P., L.G. Raisz, and T.J. Martin, *Principles of Bone Biology: Two-Volume Set*. 2008: Academic Press.
27. Nather, A., *Bone grafts and bone substitutes: basic science and clinical applications*. 2005: World Scientific.
28. Mundy, G.R., *Bone remodelling and its disorders*. 1999: CRC Press.
29. Morrison, S.J. and D.T. Scadden, *The bone marrow niche for haematopoietic stem cells.* Nature, 2014. **505**(7483): p. 327-334.
30. Seeman, E. and P.D. Delmas, *Bone quality—the material and structural basis of bone strength and fragility.* New England Journal of Medicine, 2006. **354**(21): p. 2250-2261.
31. Matsuo, K. and N. Irie, *Osteoclast–osteoblast communication.* Archives of biochemistry and biophysics, 2008. **473**(2): p. 201-209.
32. Hauschka, P.V., et al., *Growth factors in bone matrix. Isolation of multiple types by affinity chromatography on heparin-Sepharose.* Journal of Biological Chemistry, 1986. **27**(261): p. 12665-12674.
33. Henriksen, K., et al., *Local communication on and within bone controls bone remodeling.* Bone, 2009. **44**(6): p. 1026-1033.
34. Bruder, S.P., D.J. Fink, and A.I. Caplan, *Mesenchymal stem cells in bone development, bone repair, and skeletal regenaration therapy.* Journal of cellular biochemistry, 1994. **56**(3): p. 283-294.
35. Li, X.J. and W.S. Jee, *Integrated bone tissue anatomy and physiology.* Current Topics in Bone Biology, 2005: p. 11-56.
36. Barnes, G.L., et al., *Growth factor regulation of fracture repair.* Journal of Bone and Mineral Research, 1999. **14**(11): p. 1805-1815.
37. Whyte, M.P., *Hypophosphatasia and the Role of Alkaline Phosphatase in Skeletal Mineralization*.* Endocrine Reviews, 1994. **15**(4): p. 439-461.
38. Parfitt, A., *Osteonal and hemi-osteonal remodeling: the spatial and temporal framework for signal traffic in adult human bone.* Journal of cellular biochemistry, 1994. **55**(3): p. 273-286.
39. Lian, J., *Bone formation: osteoblast lineage cells, growth factors, matrix proteins and the mineralization process.* Primer on the metabolic bone diseases and disorders of mineral metabolism, 1999.
40. Aubin, J.E., *Bone formation: maturation and functional activities of osteoblast lineage cells.* Primer on the metabolic bone diseases and disorders of mineral metabolism, 2006.
41. Khosla, S., *Minireview: The opg/rankl/rank system.* Endocrinology, 2001. **142**(12): p. 5050-5055.
42. Harada, S.-i. and G.A. Rodan, *Control of osteoblast function and regulation of bone mass.* Nature, 2003. **423**(6937): p. 349-355.
43. Nakashima, K., et al., *The novel zinc finger-containing transcription factor osterix is required for osteoblast differentiation and bone formation.* Cell, 2002. **108**(1): p. 17-29.
44. Clarke, B., *Normal bone anatomy and physiology.* Clinical journal of the American Society of Nephrology, 2008. **3**(Supplement 3): p. S131-S139.
45. Marie, P.J., *Targeting integrins to promote bone formation and repair.* Nature Reviews Endocrinology, 2013. **9**(5): p. 288-295.
46. Roodman, G.D., *Cell biology of the osteoclast.* Experimental hematology, 1999. **27**(8): p. 1229-1241.
47. Nicholson, G.C., et al., *Induction of osteoclasts from CD14-positive human peripheral blood mononuclear cells by receptor activator of nuclear factor κB ligand (RANKL).* Clinical Science, 2000. **99**(2): p. 133-140.
48. Teitelbaum, S.L., *Bone resorption by osteoclasts.* Science, 2000. **289**(5484): p. 1504-1508.
49. Vaananen, H., et al., *The cell biology of osteoclast function.* Journal of cell science, 2000. **113**(3): p. 377-381.
50. Hayman, A.R. and T.M. Cox, *Tartrate-Resistant Acid Phosphatase Knockout Mice.* Journal of Bone and Mineral Research, 2003. **18**(10): p. 1905-1907.
51. Manolagas, S.C., *Birth and death of bone cells: basic regulatory mechanisms and implications for the pathogenesis and treatment of osteoporosis 1.* Endocrine reviews, 2000. **21**(2): p. 115-137.

52. Takahashi, N., et al., *Osteoclast-Like Cell Formation and its Regulation by Osteotropic Hormones in Mouse Bone Marrow Cultures*.* Endocrinology, 1988. **122**(4): p. 1373-1382.
53. Hsu, H., et al., *Tumor necrosis factor receptor family member RANK mediates osteoclast differentiation and activation induced by osteoprotegerin ligand.* Proceedings of the National Academy of Sciences, 1999. **96**(7): p. 3540-3545.
54. Yasuda, H., et al., *Osteoclast differentiation factor is a ligand for osteoprotegerin/osteoclastogenesis-inhibitory factor and is identical to TRANCE/RANKL.* Proceedings of the National Academy of Sciences, 1998. **95**(7): p. 3597-3602.
55. Boyle, W.J., W.S. Simonet, and D.L. Lacey, *Osteoclast differentiation and activation.* Nature, 2003. **423**(6937): p. 337-342.
56. Tsuda, E., et al., *Isolation of a novel cytokine from human fibroblasts that specifically inhibits osteoclastogenesis.* Biochemical and biophysical research communications, 1997. **234**(1): p. 137-142.
57. Adamopoulos, I.E. and E.D. Mellins, *Alternative pathways of osteoclastogenesis in inflammatory arthritis.* Nature Reviews Rheumatology, 2015. **11**(3): p. 189-194.
58. Mundy, G.R., *Metastasis to bone: causes, consequences and therapeutic opportunities.* Nature reviews. Cancer, 2002. **2**(8): p. 584-93.
59. Liotta, L.A. and E.C. Kohn, *The microenvironment of the tumour-host interface.* Nature, 2001. **411**(6835): p. 375-379.
60. Käkönen, S.M. and G.R. Mundy, *Mechanisms of osteolytic bone metastases in breast carcinoma.* Cancer, 2003. **97**(S3): p. 834-839.
61. Chirgwin, J.M. and T.A. Guise, *Molecular Mechanisms of Tumor-Bone Interactions in Osteolytic Metastases.* Critical Reviews™ in Eukaryotic Gene Expression, 2000. **10**(2): p. 20-20.
62. Chen, Y.C., D.M. Sosnoski, and A.M. Mastro, *Breast cancer metastasis to the bone: mechanisms of bone loss.* Breast Cancer Res, 2010. **6**(12): p. 215-215.
63. Pouliot, N., H.B. Pearson, and A. Burrows, *Investigating metastasis using in vitro platforms.* 2000.
64. Hutchinson, L. and R. Kirk, *High drug attrition rates - where are we going wrong?* Nature reviews. Clinical oncology, 2011. **8**(4): p. 189-90.
65. Eccles, S.A., et al., *Critical research gaps and translational priorities for the successful prevention and treatment of breast cancer.* Breast Cancer Research, 2013. **15**(5): p. R92.
66. Egeblad, M., M.G. Rasch, and V.M. Weaver, *Dynamic interplay between the collagen scaffold and tumor evolution.* Current opinion in cell biology, 2010. **22**(5): p. 697-706.
67. Lieschke, G.J. and P.D. Currie, *Animal models of human disease: zebrafish swim into view.* Nature Reviews Genetics, 2007. **8**(5): p. 353-367.
68. Frese, K.K. and D.A. Tuveson, *Maximizing mouse cancer models.* Nature Reviews Cancer, 2007. **7**(9): p. 654-658.
69. Baharvand, H., et al., *Differentiation of human embryonic stem cells into hepatocytes in 2D and 3D culture systems in vitro.* International Journal of Developmental Biology, 2006. **50**(7): p. 645.
70. Li, Y.-H. and C. Zhu, *A modified Boyden chamber assay for tumor cell transendothelial migration in vitro.* Clinical & experimental metastasis, 1999. **17**(5): p. 423-429.
71. Kim, J.B., R. Stein, and M.J. O'Hare, *Three-dimensional in vitro tissue culture models of breast cancer—a review.* Breast cancer research and treatment, 2004. **85**(3): p. 281-291.
72. Antoni, D., et al., *Three-dimensional cell culture: a breakthrough in vivo.* International journal of molecular sciences, 2015. **16**(3): p. 5517-5527.
73. Bersini, S., et al., *A microfluidic 3D in vitro model for specificity of breast cancer metastasis to bone.* Biomaterials, 2014. **35**(8): p. 2454-2461.
74. Aggarwal, B.B., et al., *Models for prevention and treatment of cancer: problems vs promises.* Biochemical pharmacology, 2009. **78**(9): p. 1083-94.
75. Knight, A., *Systematic reviews of animal experiments demonstrate poor human clinical and toxicological utility.* ATLA-Alternatives to Laboratory Animals, 2007. **35**(6): p. 641.
76. Polson, A.G. and R.N. Fuji, *The successes and limitations of preclinical studies in predicting the pharmacodynamics and safety of cell-surface-targeted biological agents in patients.* British journal of pharmacology, 2012. **166**(5): p. 1600-1602.

77. Russell, W.M.S., R.L. Burch, and C.W. Hume, *The principles of humane experimental technique.* 1959.
78. Breslin, S. and L. O'Driscoll, *Three-dimensional cell culture: the missing link in drug discovery.* Drug discovery today, 2013. **18**(5): p. 240-249.
79. Mehta, G., et al., *Opportunities and challenges for use of tumor spheroids as models to test drug delivery and efficacy.* Journal of Controlled Release, 2012. **164**(2): p. 192-204.
80. Lin, R.Z. and H.Y. Chang, *Recent advances in three-dimensional multicellular spheroid culture for biomedical research.* Biotechnology journal, 2008. **3**(9-10): p. 1172-1184.
81. Garg, T., et al., *Scaffold: a novel carrier for cell and drug delivery.* Critical Reviews™ in Therapeutic Drug Carrier Systems, 2012. **29**(1).
82. Whitesides, G.M., *The origins and the future of microfluidics.* Nature, 2006. **442**(7101): p. 368-373.
83. Manz, A., N. Graber, and H.á. Widmer, *Miniaturized total chemical analysis systems: a novel concept for chemical sensing.* Sensors and actuators B: Chemical, 1990. **1**(1): p. 244-248.
84. Pihl, J., M. Karlsson, and D.T. Chiu, *Microfluidic technologies in drug discovery.* Drug Discovery Today, 2005. **10**(20): p. 1377-1383.
85. Dittrich, P.S. and A. Manz, *Lab-on-a-chip: microfluidics in drug discovery.* Nature Reviews Drug Discovery, 2006. **5**(3): p. 210-218.
86. Ziolkowska, K., et al., *PDMS/glass microfluidic cell culture system for cytotoxicity tests and cells passage.* Sensors and Actuators B: Chemical, 2010. **145**(1): p. 533-542.
87. Thompson, D.M., et al., *Dynamic gene expression profiling using a microfabricated living cell array.* Analytical chemistry, 2004. **76**(14): p. 4098-4103.
88. Walker, G.M., et al., *Effects of flow and diffusion on chemotaxis studies in a microfabricated gradient generator.* Lab on a Chip, 2005. **5**(6): p. 611-618.
89. Esch, E.W., A. Bahinski, and D. Huh, *Organs-on-chips at the frontiers of drug discovery.* Nature Reviews Drug Discovery, 2015. **14**(4): p. 248-260.
90. Di Carlo, D., *Inertial microfluidics.* Lab on a Chip, 2009. **9**(21): p. 3038-3046.
91. Beebe, D.J., G.A. Mensing, and G.M. Walker, *Physics and applications of microfluidics in biology.* Annual review of biomedical engineering, 2002. **4**(1): p. 261-286.
92. Stone, H.A., A.D. Stroock, and A. Ajdari, *Engineering flows in small devices: microfluidics toward a lab-on-a-chip.* Annu. Rev. Fluid Mech., 2004. **36**: p. 381-411.
93. Squires, T.M. and S.R. Quake, *Microfluidics: Fluid physics at the nanoliter scale.* Reviews of modern physics, 2005. **77**(3): p. 977.
94. Neuži, P., et al., *Revisiting lab-on-a-chip technology for drug discovery.* Nature reviews Drug discovery, 2012. **11**(8): p. 620-632.
95. Wlodkowic, D. and J.M. Cooper, *Tumors on chips: oncology meets microfluidics.* Current Opinion in Chemical Biology, 2010. **14**(5): p. 556-567.
96. Huh, D., et al., *From Three-Dimensional Cell Culture to Organs-on-Chips.* HHS Public Access, 2015. **21**(12): p. 745-754.
97. Sung, K.E. and D.J. Beebe, *Microfluidic 3D models of cancer.* Advanced drug delivery reviews, 2014. **79**: p. 68-78.
98. Ziółkowska, K., R. Kwapiszewski, and Z. Brzózka, *Microfluidic devices as tools for mimicking the in vivo environment.* New Journal of Chemistry, 2011. **35**(5): p. 979-990.
99. Wu, L.Y., D. Di Carlo, and L.P. Lee, *Microfluidic self-assembly of tumor spheroids for anticancer drug discovery.* Biomedical microdevices, 2008. **10**(2): p. 197-202.
100. Huang, C.P., et al., *Engineering microscale cellular niches for three-dimensional multicellular co-cultures.* Lab on a Chip, 2009. **9**(12): p. 1740-1748.
101. Gao, Y., et al., *A versatile valve-enabled microfluidic cell co-culture platform and demonstration of its applications to neurobiology and cancer biology.* Biomedical microdevices, 2011. **13**(3): p. 539-548.
102. Sung, K.E., et al., *Transition to invasion in breast cancer: a microfluidic in vitro model enables examination of spatial and temporal effects.* Integrative Biology, 2011. **3**(4): p. 439-450.
103. Sousa, D., et al., *Ablation of Y1 receptor impairs osteoclast bone-resorbing activity.* Sci. Rep. , 2016. **33470**(6).

104. Park, J.W., et al., *Microfluidic culture platform for neuroscience research.* Nature protocols, 2006. **1**(4): p. 2128-2136.
105. Corning, *Corning Matrigel® Matrix*, C.I.L. Sciences, Editor. 2012.
106. Oridate, N., R. Lotan, and D. Lotan, *Reconstituted basement membrane (matrigel®): A useful semisolid medium for growth of tumor cell colonies.* In Vitro Cellular & Developmental Biology-Animal, 1996. **32**(4): p. 192-193.
107. Mueller-Klieser, W., *Tumor biology and experimental therapeutics.* Critical reviews in oncology/hematology, 2000. **36**(2): p. 123-139.
108. Diaspro, A., F. Federici, and M. Robello, *Influence of refractive-index mismatch in high-resolution three-dimensional confocal microscopy.* Applied optics, 2002. **41**(4): p. 685-690.
109. Liu, L.-L., et al., *Identification of valid reference genes for the normalization of RT-qPCR expression studies in human breast cancer cell lines treated with and without transient transfection.* PloS one, 2015. **10**(1): p. e0117058.
110. Ferreira, E. and M.J. Cronjé, *Selection of suitable reference genes for quantitative real-time PCR in apoptosis-induced MCF-7 breast cancer cells.* Molecular biotechnology, 2012. **50**(2): p. 121-128.
111. Graff, J.R., et al., *E-cadherin expression is silenced by DNA hypermethylation in human breast and prostate carcinomas.* Cancer research, 1995. **55**(22): p. 5195-5199.
112. Ivascu, A., *High-throughput tumor spheroid generation and cacterization of spheroid adhesions and tight junctions*. 2007.
113. Helfrich, M.H., *Bone research protocols*. Vol. 80. 2003: Springer Science & Business Media.
114. Fakhry, M., et al., *Molecular mechanisms of mesenchymal stem cell differentiation towards osteoblasts.* World J Stem Cells, 2013. **5**(4): p. 136-148.
115. Addadi, L. and S. Weiner, *Interactions between acidic proteins and crystals: stereochemical requirements in biomineralization.* Proceedings of the National Academy of Sciences, 1985. **82**(12): p. 4110-4114.
116. Anderson, H.C., *Vesicles associated with calcification in the matrix of epiphyseal cartilage.* The Journal of cell biology, 1969. **41**(1): p. 59-72.
117. Safadi, F.F., et al., *Bone structure, development and bone biology*, in *Bone pathology*. 2009, Springer. p. 1-50.
118. Spector, J.A., et al., *Osteoblast expression of vascular endothelial growth factor is modulated by the extracellular microenvironment.* American Journal of Physiology-Cell Physiology, 2001. **280**(1): p. C72-C80.
119. Søe, K. and J.M. Delaissé, *Glucocorticoids maintain human osteoclasts in the active mode of their resorption cycle.* Journal of bone and mineral research, 2010. **25**(10): p. 2184-2192.
120. Kleinhans, C., et al., *Comparison of osteoclastogenesis and resorption activity of human osteoclasts on tissue culture polystyrene and on natural extracellular bone matrix in 2D and 3D.* Journal of biotechnology, 2015. **205**: p. 101-110.
121. Boyde, A., N. Ali, and S. Jones, *Resorption of dentine by isolated osteoclasts in vitro.* British dental journal, 1984. **156**(6): p. 216-220.
122. Faccio, R., et al., *Dynamic changes in the osteoclast cytoskeleton in response to growth factors and cell attachment are controlled by β3 integrin.* The Journal of cell biology, 2003. **162**(3): p. 499-509.
123. Lee, J., et al., *A matrix metalloproteinase inhibitor, batimastat, retards the development of osteolytic bone metastases by MDA-MB-231 human breast cancer cells in Balb C nu/nu mice.* European journal of cancer, 2001. **37**(1): p. 106-113.
124. Sundaram, K., et al., *RANK ligand signaling modulates the matrix metalloproteinase-9 gene expression during osteoclast differentiation.* Experimental cell research, 2007. **313**(1): p. 168-178.
125. Nakopoulou, L., et al., *MMP-2 protein in invasive breast cancer and the impact of MMP-2/TIMP-2 phenotype on overall survival.* Breast cancer research and treatment, 2003. **77**(2): p. 145-155.
126. Shimokawa, K.-i., et al., *Matrix metalloproteinase (MMP)-2 and MMP-9 activities in human seminal plasma.* Molecular human reproduction, 2002. **8**(1): p. 32-36.

127. Takeshita, S., K. Kaji, and A. Kudo, *Identification and characterization of the new osteoclast progenitor with macrophage phenotypes being able to differentiate into mature osteoclasts.* Journal of Bone and Mineral Research, 2000. **15**(8): p. 1477-1488.
128. Walker, G.M., H.C. Zeringue, and D.J. Beebe, *Microenvironment design considerations for cellular scale studies.* Lab on a Chip, 2004. **4**(2): p. 91-97.
129. Berthois, Y., J.A. Katzenellenbogen, and B.S. Katzenellenbogen, *Phenol red in tissue culture media is a weak estrogen: implications concerning the study of estrogen-responsive cells in culture.* Proceedings of the National Academy of Sciences, 1986. **83**(8): p. 2496-2500.
130. Ney, J., et al., *RANK, RANKL and OPG expression in breast cancer–influence on osseous metastasis.* Geburtshilfe und Frauenheilkunde, 2012. **72**(05): p. 385-391.
131. Jordan, N.V., et al., *HER2 expression identifies dynamic functional states within circulating breast cancer cells.* Nature, 2016.

Annexes

Table A.I. Primers used in quantative RT-PCR analysis.

Name	Genbank accession no.	Primer Sequence	Product Length	~Tm
Beta-2-microglobulin (B2M)	NM_004048.2	Fw 5'- GATGAGTATGCCTGCCGTGT -3′ Rv 5'- TGCGGCATCTTCAAACCTCC -3′	105	60.18 60.96
Histone H2A (HIST)	NM_003509.2	Fw 5'- AAGTCACCATCGCACAGGG -3′ Rv 5'- AATCCAGGCTTCTACTTGCCC -3′	106	60.00 60.06
Tyrosine 3-monooxygenase/tryptophan 5-monooxygenase activation protein zeta (YWHAZ)	NM_003406.3	Fw 5'- ACGTCCCTCAAACCTTGCTT -3′ Rv 5'- GGCCTTCTGAACCAGCTCAT -3′	76	59.82 60.03
Vascular endothelial growth factor Iso-165 (VEGF)	NM_001033756.2	Fw 5'- CTTGCCTTGCTGCTCTACCT -3' Rv 5'- GCAGTAGCTGCGCTGATAGA -3'	123	60.04 59.97
Receptor activator of nuclear factor kappa B (RANK)	AF018253.1	Fw 5'- CGTTGCAGCTCAACAAGGAC -3' Rv 5'- TCCGTGGAGGAAAAGGCATC -3'	76	60.04 60.04
Receptor activator of nuclear factor kappa B ligand (RANKL)	AF019047.1	Fw 5'- CCCAACGGTACACGACTCA -3' Rv 5'- CATCTCCCACTGGCAGGTAAATA -3'	76	59.34 59.86
Collagen type 1-alpha (COL1A1)	AF017178.2	Fw 5'- CGCAGTGGCCTCCTAATTTC -3' Rv 5'- GAATGGAAGGCAAGCCCATC -3'	89	58.98 59.25
Osterix (OSX)	NM_152860.1	Fw 5'- GCTCCTTGGGACCCGTTC -3′ Rv 5'- AGCCATAGTGAACTTCCTCCTCA -3′	70	60.05 60.82
Bone sialoprotein (IBSP)	J05213.1	Fw 5'- CAGAAGGCACCACAGAGACC -3' Rv 5'- CCAAAAGGTGGGGAAGTGGT -3'	124	60.32 60.11
Runt related transcription factor 2 (RUNX2)	NM_001024630.3	Fw 5'- GAGTGGACGAGGCAAGAGTT -3' Rv 5'- CTGTCTGTGCCTTCTGGGTT -3'	127	59.68 59.69
Osteocalcin (OCN)	NM_199173.5	Fw 5'- CTCACACTCCTCGCCCTATTG -3' Rv 5'- GCTTGGACACAAAGGCTGCAC -3'	109	60.20 62.87
Alkaline phosphatase (ALP)	BC021289.2	Fw 5'- AGAACCCCAAAGGCTTCTTC -3′ Rv 5'- CTTGGCTTTTCCTTCATGGT -3′	74	57.71 56.20
Tartrate-resistant acid phosphatase 5b (TRACP 5b)	DL489316.1	Fw 5'- CTACCCACTGCCTGGTCAAG -3′ Rv 5'- TCCATGAAATTCCCAGCCCC -3′	148	60.04 60.03
Cathepsin K (CtsK)	NM_000396.3	Fw 5'- TTCCCGCAGTAATGACACCC -3′ Rv 5'- GGAACCACACTGACCCTGAT -3′	118	60.04 59.31
Calcitonin receptor (CTR)	BC075028.2	Fw 5'- CAACATTGTCCGGGTGCTTG -3′ Rv 5'- GGATCATGGTGGCCTTCACA -3′	92	60.04 60.03
Nuclear factor of activated T-cells 1 (NFATc1)	NM_172390.2	Fw 5'- TGTGCAAGCCGAATTCTCTG -3′ Rv 5'- GAAAGATGGCGTTACCGTTGG -3′	159	58.84 59.87
FBJ murine osteosarcoma viral oncogene homolog (c-FOS)	NM_005252.3	Fw 5'- GGGGCAAGGTGGAACAGTTA -3′ Rv 5'- GTCTGTCTCCGCTTGGAGTG -3′	134	59.89 60.39

Table A.2. Primer efficiency analysis of genes tested

B2M

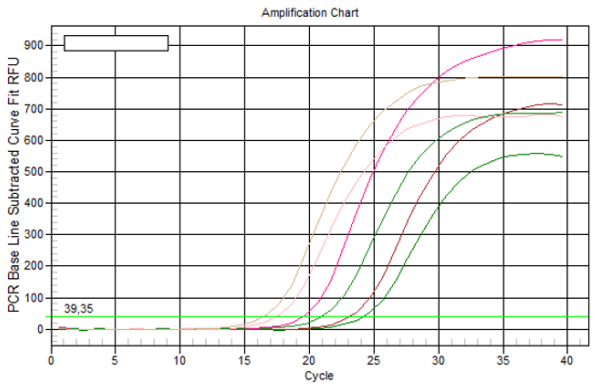

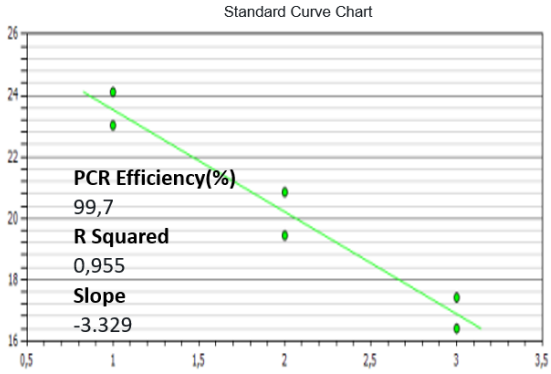

YWHAZ

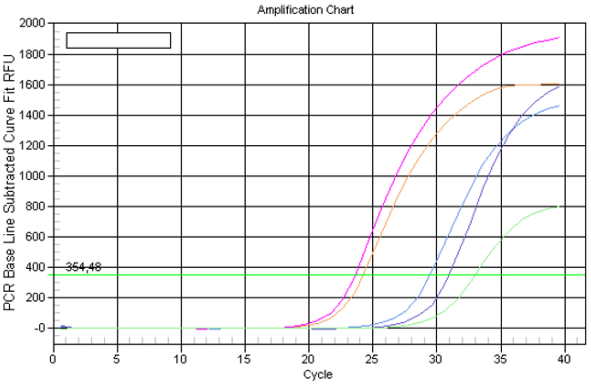

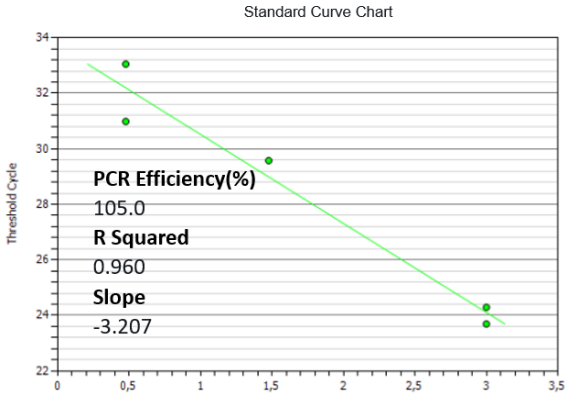

RANK

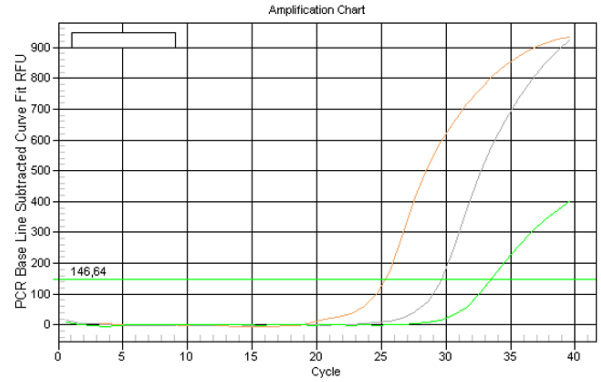

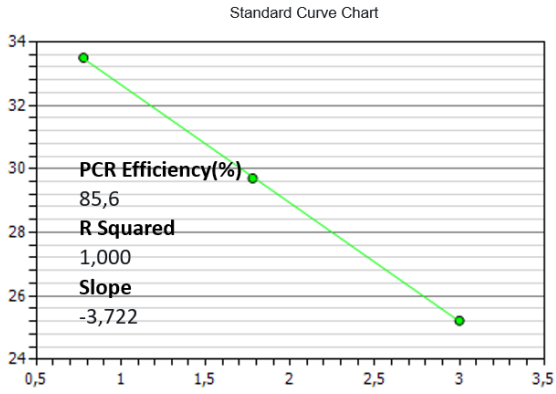

COL1A1

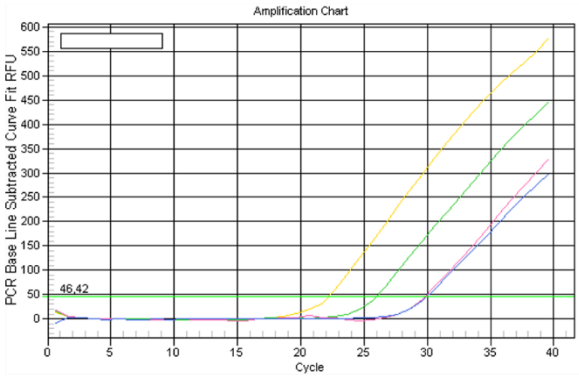

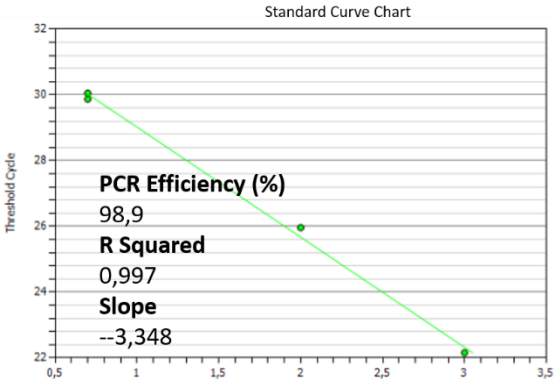

IBSP

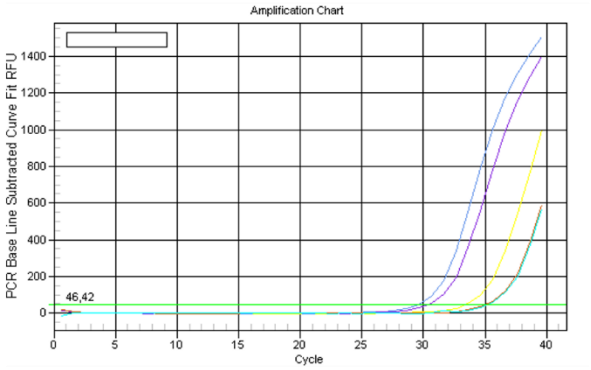

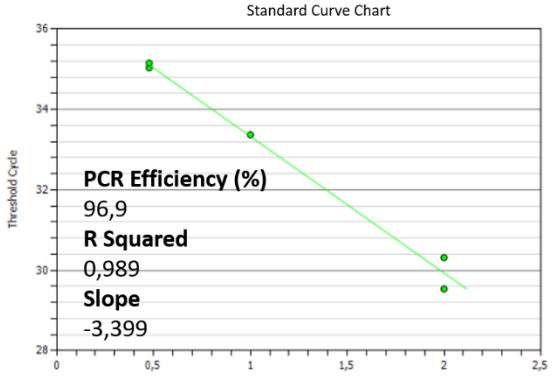

PUNX2

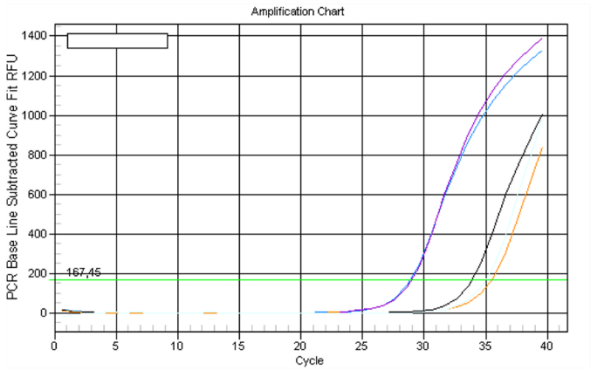

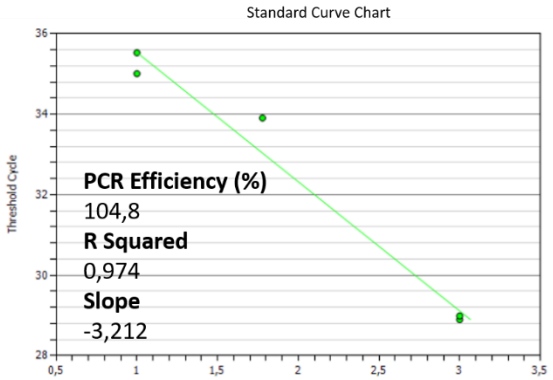

VEGF

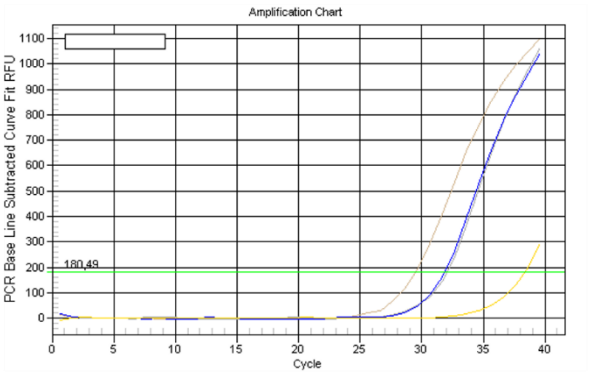

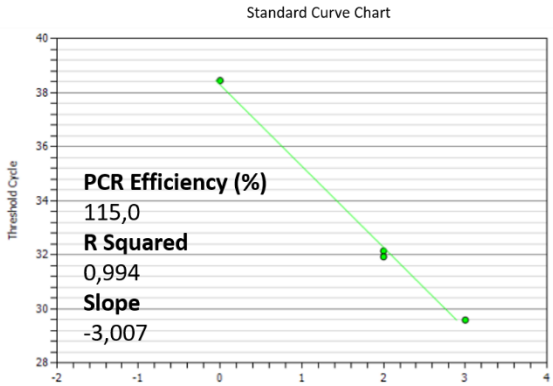

OCN

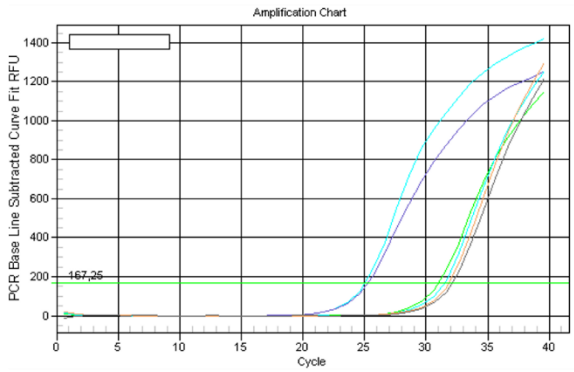

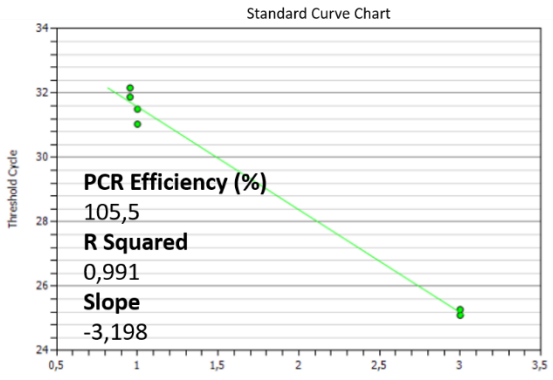

ALP

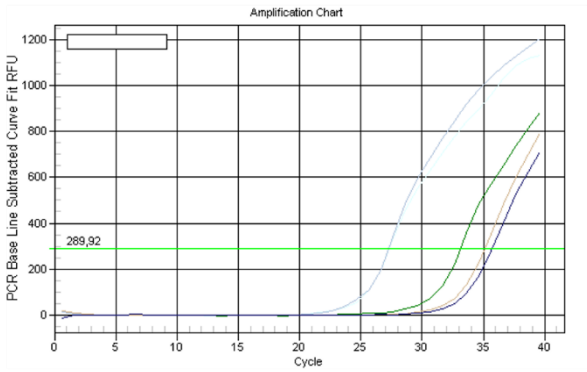

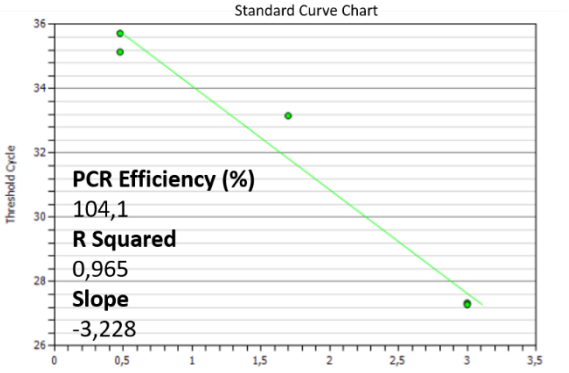

TRAP

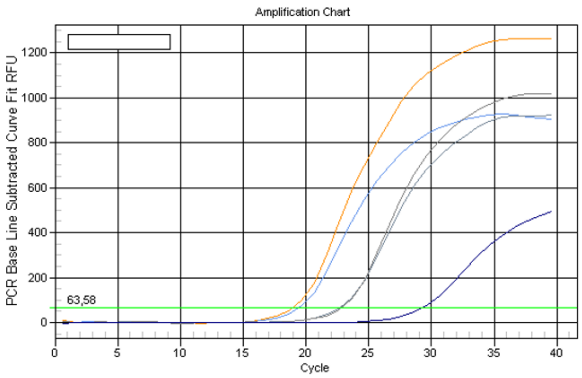

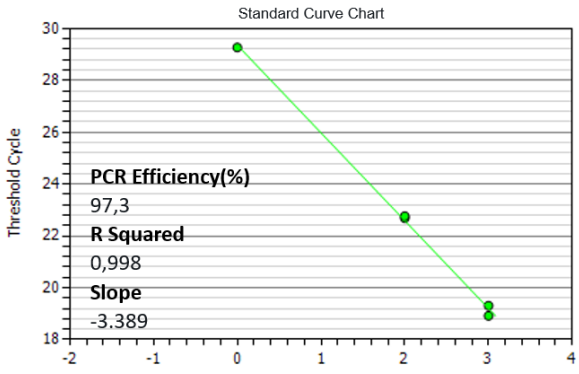

CtsK

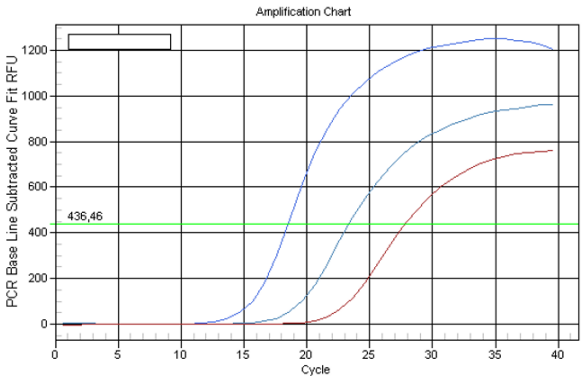

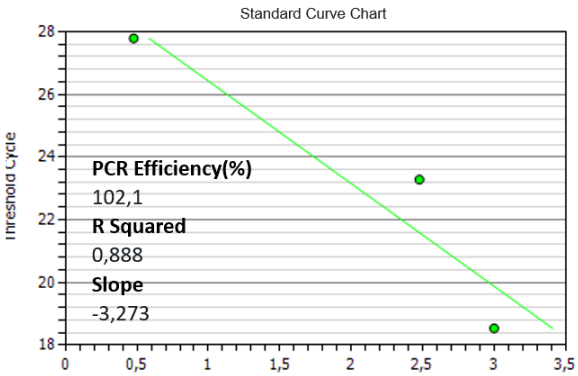

NFATC1

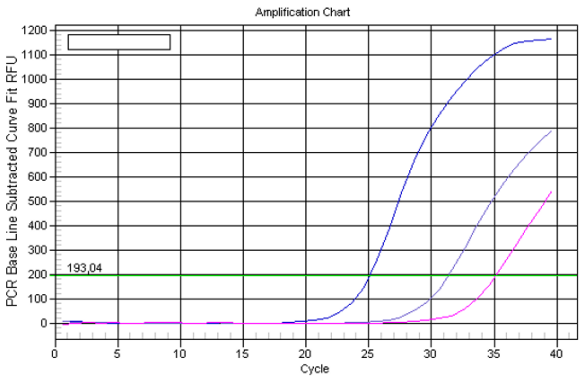

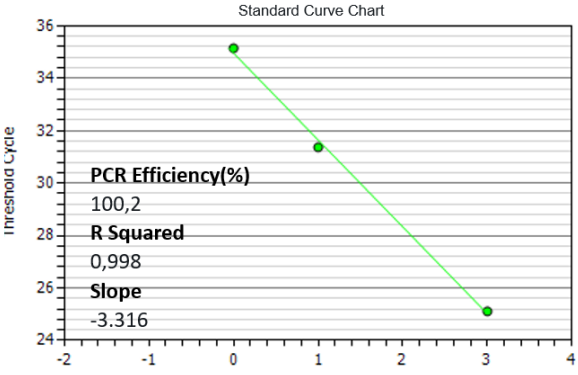

c-FOS

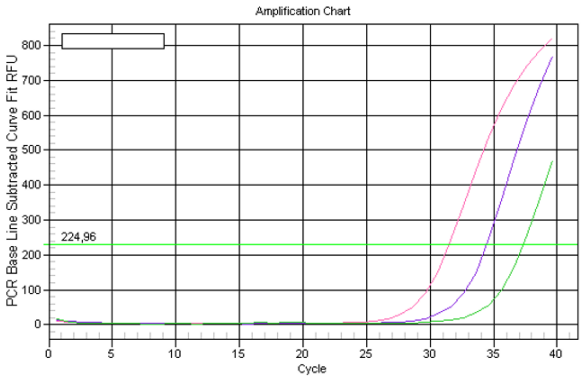
Amplification Chart
PCR Base Line Subtracted Curve Fit RFU
224,96
Cycle

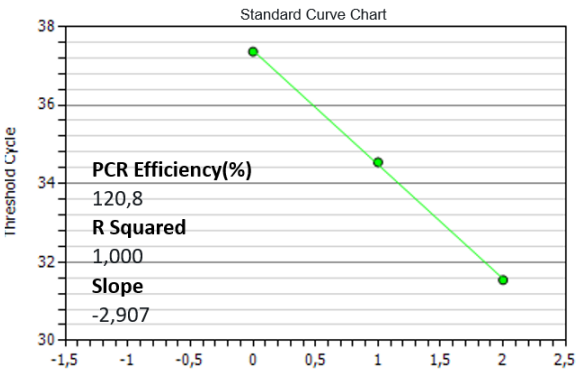
Standard Curve Chart
Threshold Cycle
PCR Efficiency(%)
120,8
R Squared
1,000
Slope
-2,907